Universität Rostock



Traditio et Innovatio

Mixtures of Methane and Hydrogen under Planetary Conditions

Kumulative Dissertation
zur Erlangung des akademischen Grades
doctor rerum naturalium (Dr. rer. nat.)
der Mathematisch-Naturwissenschaftlichen Fakultät
der Universität Rostock

vorgelegt von
Argha Jyoti Roy,
geboren am 31. Dezember 1997 in Siliguri, West Bengal, Indien

Rostock, October 15, 2025

https://doi.org/10.18453/rosdok_id00005794



Dieses Werk ist lizenziert unter einer
Creative Commons Namensnennung 4.0 International Lizenz.

1. Gutachter: Prof. Dr. Ronald Redmer, Institut für Physik, Universität Rostock
2. Gutachter: Prof. Dr. Andreas Hermann, Institute for Condensed Matter and Complex Systems (ICMCS), University of Edinburgh

Jahr der Einreichung: 2025
Jahr der Verteidigung: 2026
Tel: +49 (0) 381 498-6917
Internet: https://www.statistische.physik.uni-rostock.de
E-Mail: argha.roy@uni-rostock.de

Abstract

The present cumulative thesis describes the thermodynamic and electronic properties of mixtures of methane (CH_4) and hydrogen (H_2) at high pressures and temperatures. Hydrogen, Methane and Water are the most abundant molecules in our Universe and yet attributes of their mixtures lack substantial data and understanding. We focus on characterizing and calculating equation of state and structural changes of CH_4–H_2 mixtures using *ab initio* method density functional theory molecular dynamics (DFT–MD).
To complement the existing sparse dataset on the mixture of methane and hydrogen, we first investigate thermodynamic properties of the fluid mixture. We then compare the resulting equation of state and structural changes to those of pure methane and hydrogen to understand the mixture as a whole. Expanding on this, we explain the changes in thermodynamic and electronic properties due to varying concentrations of hydrogen molecules in the mixture. Additionally, we discuss models that incorporate nonideal effects as a function of concentration for the thermal equation of state and electronic properties. We also validate the linear mixing approximation for the binary mixture of methane and hydrogen. Finally, we outline the basics and computational efficacy of a new technique, stochastic finite–temperature density functional theory combined with Langevin dynamics (sDFT–MD), to overcome the computational challenges of traditional DFT−MD under warm dense matter conditions.

Zusammenfassung

Die vorliegende kumulative Dissertation beschreibt die thermodynamischen und elektronischen Eigenschaften von Mischungen aus Methan (CH_4) und Wasserstoff (H_2) bei hohen Drücken und Temperaturen. Wasserstoff, Methan und Wasser gehören zu den häufigsten Molekülen im Universum, und dennoch mangelt es bislang an ausreichenden Daten und Verständnis über die Eigenschaften ihrer Mischungen. Im Fokus dieser Arbeit steht die Charakterisierung und Berechnung der Zustandsgleichung sowie der strukturellen Veränderungen von CH_4–H_2 Mischungen mithilfe der ab initio−Methode der Molekulardynamik auf Grundlage der Dichtefunktionaltheorie (DFT–MD).
Um die bislang spärliche Datengrundlage zu Mischungen aus Methan und Wasserstoff zu erweitern, untersuchen wir zunächst die thermodynamischen Eigenschaften der Fluidmischung. Anschließend vergleichen wir die daraus resultierende Zustandsgleichung und die strukturellen Veränderungen mit denen von reinem Methan und reinem Wasserstoff, um ein umfassenderes Verständnis der Mischung zu erlangen. Darauf aufbauend erläutern wir die Änderungen der thermodynamischen und elektronischen Eigenschaften in Abhängigkeit von unterschiedlichen Wasserstoffkonzentrationen in der Mischung. Zusätzlich werden Modelle vorgestellt, die nichtideale Effekte als Funktion der Konzentration für die thermische Zustandsgleichung und die elektronischen Eigenschaften berücksichtigen. Weiterhin überprüfen wir die Gültigkeit der linearen Mischungsnäherung für das binäre System aus Methan und Wasserstoff. Abschließend stellen wir die Grundlagen und die rechnerische Effizienz einer neuen Methode vor–der stochastischen Dichtefunktionaltheorie bei endlicher Temperatur kombiniert mit Langevin-Dynamik (sDFT–MD) um die rechnerischen Herausforderungen der herkömmlichen DFT–MD unter Bedingungen dichter, warmer Materie zu überwinden.

Contents

1. Introduction **1**

1.1. Warm Dense Matter (WDM) . . . 2
1.2. From Hydrogen to Methane . . . 3
1.3. Current understanding of methane–hydrogen mixtures . . . 5
1.4. Linear mixing approximation (LMA) . . . 6
1.5. Aim and Outline of this thesis . . . 7

2. Methodology **8**

2.1. Many−body problem . . . 8
2.2. Born-Oppenheimer Approximation . . . 9
2.3. Density Functional Theory . . . 10
2.3.1. Kohn-Sham formalism at finite temperatures . . . 12
2.3.2. Plane waves and pseudopotentials . . . 13
2.3.3. Approximation of the exchange-correlation functional . . . 15
2.4. Molecular Dynamics Simulation . . . 16
2.5. DFT−MD simulations with VASP . . . 17

3. Additional theoretical means **19**

3.1. Equation of state (EOS) . . . 19
3.2. Structural properties of fluids . . . 19
3.2.1. Pair distribution function (PDF) . . . 20
3.2.2. Diffusion coefficient . . . 20
3.3. Electronic properties . . . 20
3.3.1. Band gap calculation . . . 21
3.3.2. Electrical and thermal conductivity . . . 22

4. Stochastic density functional theory **24**

4.1. Bottelneck of traditional KS-DFT . . . 24
4.2. The Essence of Stochastic DFT (sDFT) . . . 24
4.2.1. Random Variables . . . 25
4.2.2. Stochastic vectors . . . 25
4.2.3. sDFT . . . 26
4.2.4. Chebyshev methods . . . 27
4.3. Langevin dynamics . . . 29

5. Results **30**
5.1. $CH_4 + H_2$ . . . 30
5.1.1. Evaluation of the Linear Mixing Approximation (LMA) . . . 30
5.1.2. Structural Changes . . . 31
5.2. Modeling the EOS and electronic properties . . . 32
5.2.1. Thermal EOS . . . 33
5.2.2. Transport Properties . . . 34
5.3. sDFT-MD: Hydrogen as a test case . . . 37
5.4. Summary and Outlook . . . 39

6. Publications **41**
6.1. Mixture of hydrogen and methane under planetary interior conditions . . . 41
6.2. Understanding the transport properties of methane–hydrogen mixtures under the interior conditions of ice giants . . . 54
6.3. Stochastic density functional theory combined with Langevin dynamics for warm dense matter . . . 68

A. Appendix **84**
A.1. EOS: Mixtures . . . 84
A.2. Convergence of DFT-MD and electronic properties simulations . . . 84

Bibliography **87**

B. Curriculum vitae **98**

C. Acknowledgement **100**

D. Danksagung **101**

E. Declaration **102**

1. Introduction

Ordinary matter exhibits various states such as Gases, Solids, Liquids and Plasma, when subjected to different thermodynamic conditions. At the junction of condensed matter and plasmas, we encounter an exotic state of matter termed as warm dense matter (WDM) signified by the appearance of quantum degeneracy, Coulomb correlations, and thermal effects. Although this state of matter is not part of our everyday lives, we are constantly influenced by it: For example, the Earth's geodynamo arises from molten iron and nickel at immense pressures that maintain them in a fluid state [1–4]. Similarly, geodynamic activity of other planets such as Mercury [5], Mars [6], Jupiter [7], and Saturn [8] are governed by materials exhibiting behavior that can only occur under WDM conditions. In the gas giants in our solar system (Jupiter and Saturn), brown dwarfs, the crusts of white dwarfs, and most stars primarily consist of hydrogen and helium. Under certain high-pressure and high-temperature conditions, this mixture undergoes phase transitions, miscibility changes, and electronic transitions. One particularly important process is the demixing of hydrogen and helium [9–11] in the interior of gas giants, which triggers helium rain [12, 13], the formation and decent of helium droplets that release gravitational energy. Similarly, the phase separation between carbon and hydrogen can lead to the gravitational settling of diamond [14–17], a mechanism proposed to explain the contrasting luminosities of Uranus and Neptune [18, 19]. Knowledge of materials properties under WDM conditions is therefore essential not only for explaining the structure and evolution of solar system but also for interpreting the nature of extrasolar planets (exoplanets). A prominent example is 51 Pegasi b [20], which was the first discovered exoplanet orbiting a Sun-like G-type star [21], with an orbital period of less than five days, despite having almost half the mass of Jupiter [22], defying the previous models of planetary formation and evolution. This discovery led scientists to classify such planets as *hot Jupiters*. Since then, other classes of exoplanets have emerged such as *mini−Neptunes*, *hot−Neptunes* such as GJ 436b [23], the super–Neptune HAT-P-11b [24], etc. In order to understand and expand the evolution of planets, planetary models are utilized [25, 26], which rely critically on the equation of state (EOS) (thermal and caloric) of the non–ideal mixture of elements, as well as on transport properties like electrical and thermal conductivities, viscosity, and diffusivities under WDM conditions.

Beyond planetary science, WDM also plays a pivotal role in inertial fusion experiments as the pressure−temperature path in inertial fusion experiments in facilities like the National Ignition Facility (NIF) [27, 28], the Laser Megajoule (LMJ), and/or the OMEGA

laser [29] traverses the WDM regime. Other advancements in techniques to reach high pressures and conduct probes, such as X-ray free−electron lasers, are currently in demand in facilities like the EuXFEL [30], LCLS [31, 32], and SACLA [33]. Scientists utilize techniques developed from WDM experiments to synthesize materials such as nanodiamonds from hydrocarbons or Fe-C superionic alloys [34, 35] to name a few. In particular, researchers use materials with high activation thresholds, along with rescaled setups in the semiconductor industry.

Theoretically, the description of WDM is challenging, as the quantum degeneracy and Coulomb correlations cannot be treated as a perturbation in this regime. Consequently, advanced many-body methods have been developed to describe such systems with growing success. Some of these techniques include the Green's function method [36], the Bethe-Salpeter equation [37], and density functional theory (DFT), with the latter being the most frequent choice of methods. In this work, we employ DFT coupled with molecular dynamics to solve the many−body problem under WDM conditions.

1.1 Warm Dense Matter (WDM)

In the high-density, low-temperature limit, the system behaves as a degenerate Fermi gas, where quantum mechanical degeneracy arises from the antisymmetric nature of fermionic wave functions. At a slightly lower density range, the electron gas prefers to localize to minimize the Columbic repulsion, while maintaining long-range order (Wigner crystal). Conversely at the low−density, high−temperature limit, thermal effects, i.e., the kinetic energy, dominates, and approximations such as the Jellium model are used to describe the macroscopic effects. Further increase in temperature causes the charged particles to exhibit relativistic effects. In the intermediate region lies the WDM regime, where particles are partially ionized atoms and/or partially dissociated molecules. For the free electron gas it is characterized by temperatures between 0.1−100 eV and densities below solid density. The quantum mechanical degeneracy and Coulomb correlations between the particles play an equally significant role and neither the perturbative plasma models and/or standard condensed matter theory is applicable.

To qualitatively assess the importance of the aforementioned effects, a few simple parameters have been introduced: the coupling parameter Γ and the degeneracy parameter Θ. The coupling parameter is defined by the ratio of the Coulomb potential E_C, and the thermal energy E_{Th}.

$$\Gamma = \frac{E_{\mathrm{C}}}{E_{\mathrm{Th}}} = \frac{e^2}{4\pi\epsilon_0 k_b T}\left(\frac{4\pi n_e}{3}\right)^{1/3}. \tag{1.1}$$

It gauges the correlation effects among the particles. Here, e is the electronic charge, ϵ_0 is the vacuum permittivity, k_b is the Boltzmann constant, $\hbar$ is the reduced Planck's constant, n_e is the electron density, and T is the temperature.

The degeneracy parameter, defined by the ratio of the thermal to the Fermi energy E_F,

$$\Theta = \frac{E_{\mathrm{Th}}}{E_F} = \frac{2m_e k_b T}{\hbar^2}\left(\frac{1}{3\pi^2 n_e}\right)^{2/3}. \tag{1.2}$$

assesses the effect of quantum degeneracy, where m_e is the mass of the electron. These two parameters can be used to classify plasmas,

$$\Gamma \gtrless 1 \begin{cases} \text{strongly coupled plasmas (nonideal)} \\ \text{weakly coupled plasmas (ideal)} \end{cases} \tag{1.3}$$

$$\Theta \gtrless 1 \begin{cases} \text{classical plasmas} \\ \text{degenerate plasmas} \end{cases} \tag{1.4}$$

Typically, WDM conditions are achieved when both parameters are close to unity, rendering perturbation expansion techniques ineffective and necessitating many-body approaches to account for quantum effects. One of the most used choices for the simulation of WDM is finite−temperature DFT−MD using the Kohn-Sham formalism, as discussed in Sec. 2.1. Other popular choices include orbital−free DFT−MD [38, 39], spectral quadrature DFT−MD [40], time−dependent DFT (TDDFT) [41], and stochastic DFT (sDFT); see Sec. 4.1. Other methods, such as Coupled Cluster theory [42] and path integral Monte Carlo [43–45] offer higher accuracy by circumventing approximations inherent to DFT–MD formalism; however, their application remains limited to low-Z systems due to computational cost. For a more thorough and detailed comprehension of WDM, see Refs. [46–48].

1.2 From Hydrogen to Methane

Three minutes after the Big Bang, hot dense protons and neutrons combined to produce atomic nuclei in a process called Big Bang nucleosynthesis [49–51]. Around 380,000 years later, the electrons localized as the early universe cooled down sufficiently to form hydrogen atoms, allowing photons to decouple and the cosmic microwave background (CMB) to emerge [52–54]. Over 100 to 200 million years, the early universe saw the formation of the first generation of stars, known as Population III stars, due to the gravitational collapse of hydrogen clouds [55–57], starting the process of stellar evolution and heavier element formation.

Hydrogen plays a fundamental role in shaping the structure and evolution of astrophysical objects. It exists under all conceivable physical conditions, from the coldest corners of interstellar gas pockets to ultra dense interiors of neutron stars, where temperatures and pressures reach up to billions of Kelvin and trillions of atmospheres. Hydrogen makes up about 92% of the Sun's mass, where it converts to Helium due to nuclear fusion at 15 mil-

lion Kelvin. In Sun−like stars, proton−proton chain nuclear fusion is found to be more efficient [58–60] than the Carbon−Nitrogen−Oxygen (CNO) cycle [61], with the latter being hypothesized to be dominating for stars with having 1.3 times the solar mass [58]. The excess fusion energy is then released as photons, powering life on Earth. Here, hydrogen is an essential component of our everyday life as one of the key components of DNA, water, and in industrial applications. Of the solar planets, the gas giants hold the highest concentration of H, as gravity data of the Juno and Cassini space probes suggests [62, 63]. Both Jupiter and Saturn possess dipolar intrinsic magnetic fields, driven by conductive hydrogen. Studies suggest hydrogen to undergo a first−order liquid−liquid non−metal−to−metal phase transition below 2000 K and at a pressure of around few Mbar [9, 64]. This metallization of H is predicted to initiate the demixing of H and He in sufficiently cold gas giants, such as Jupiter and Saturn [65–68]. A similar effect may exist in H_2O-H_2 mixtures [69, 70]. Recently, hydrogen has caught interest in the field of inertial confinement fusion (ICF) and alongisde the mixture of deuterium and tritium [71–73]. Despite the nature of pure hydrogen being interesting in itself and warranting more theoretical and experimental investigation, the propensity of hydrogen to combine with other elements makes it even more interesting, especially at high pressures and temperatures [74–77]. However, for planetary science, three major molecules containing hydrogen are Water (H_2O), Ammonia (NH_3) and Methane (CH_4).

Methane was first found in natural gases by Alessandro Volta. His investigation of marsh gas in the Lake Maggiore led to the identification and isolation of methane, constituting a 94% of natural gas. Being the simplest of saturated hydrocarbon alkane, having a molar mass of 16.043 g/mol, four equivalent single-bonded hydrogen, creating a highly symmetric tetrahedron structure (T_d), and a standardized bonding angle of 109.47° with melting and boiling points at 90.69 K and 111.66 K [78], respectively, at normal temperature and pressure (NTP). The symmetry plays an important role, as the equivalency of the bonds between C and H is not due to the hybridization, but is a consequence of the molecular point group symmetry [79]. On our planet, methane is a gaseous fluid, found in various parts of the geosphere, including the subsurface rocky crust, the atmosphere, and the complex fluid dynamics of the hydrosphere and lithosphere. Alongside CO_2, this hydrocarbon is a pivotal contributor to the greenhouse effect, due to its capacity to trap heat and influence climate variations [80–82]. The pathways for methane production are diverse; it is released through submarine volcanic activity [83] and is also believed to be generated as a byproduct of the serpentinization process [84, 85]. However, the detailed mechanisms of the formation of methane is still a subject of active debate.

In our Solar System, methane is the third–most abundant species after hydrogen and helium in the upper atmospheres of Jupiter and Saturn, with approximately 0.2% molecular abundance [86]. Different studies suggest a CH_4/H_2 ratio of $(1.9-2.3)\times 10^{-3}$ in Jupiter [87–89]. Observations from the Cassini mission suggest a mole fraction of 4.7×10^{-3} [88–91] in Saturn. The gas giants' temperatures are not enough to condense methane

and make it chemically stable, except for in the upper atmosphere of Jupiter, where solar UV radiation dissociates methane molecules, forming long–chained hydrocarbons. In Neptune and Uranus, methane is contained in vast amounts, together with water and ammonia. In the atmosphere of the ice giants, where it is a photochemically active volatile molecule, the measured carbon concentration is about 2-6% [92]. In the strato− and thermospheres of these ice giants, the primary photolysis of CH_4 [93, 94] occurs mainly due to the incoming solar flux, especially from the Lyman-α (121.6 nm).

- $CH_4 + h\nu \longrightarrow CH_3 + H.$

The radicals formed in this dominant reaction drive the formation of complex hydrocarbons in secondary reactions to form acetylene, ethane, and heavier hydrocarbons, giving the planets a bluish or greenish appearance [95]. Even on the largest moon of Saturn, Titan, liquid filled basins were discovered by Cassini in the polar regions, composed of methane mixed with ethane and other organic compounds. The occurrence of methane is not only restricted to celestial planets. Flyby missions and ground based IR observation discovered methane as a primary volatile in up to eleven comets, with abundances ranging from 0.4% to 2% with respect to water [96–101].
Methane is the most abundant organic molecule in our universe and has therefore been proposed as exoplanets bio-signature. It has a short photochemical lifetime in the atmosphere of terrestrial planets, thus implying replenishment from biotic processes, especially for planets with an Earth-like biosphere. The James Webb Space Telescope (JWST) discovered K2-18b, is a methane and carbon dioxide rich exoplanet orbiting in the habitable zone of dwarf star K2-18, merely 120 light-years from Earth. With the observed shortage of ammonia, the existence of a water ocean underneath the hydrogen atmosphere becomes very promising. From the preliminary data, dimethyl sulfide (DMS) is suspected to be present, which is produced by life on Earth [102]. However, the statistical significance of the DMS fingerprint in K2-18b's atmosphere has been heavily challenged in recent studies [103–105].

1.3 Current understanding of methane–hydrogen mixtures

The electronic structure of hydrogen makes it an active agent in chemical reactions under NTP. It also has a propensity to form stable high pressure compounds up to 100 GPa. The first high−pressure compounds of methane and hydrogen were reported about 26 years ago where a variety of crystal compositions $(CH_4)_2H_2$, CH_4H_2, $CH_4(H_2)_4$ were predicted in the pressure range of 5−7 GPa [106]. Theoretical explorations yield a variety of hydrogen rich structures including triclinic $(CH_4)_2H_3$ and trigonal $(CH_4)_2(H_2)_7$, along with several structures stable up to 200 GPa [107]. Doping carbonaceous sulfur hydride systems with methane is thought to have room temperature superconductivity under high pressure, however, experimental confirmations are still missing. Recent work of Ranieri

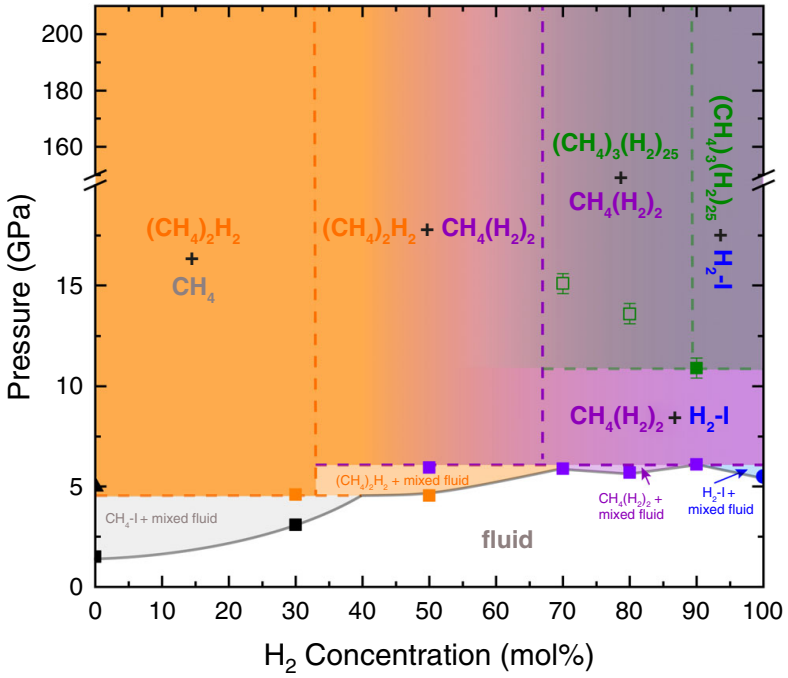


Figure 1.1.: Phase diagram of methane–hydrogen mixture as a function of H_2 concentration, courtesy of Ranieri et al. [108].

et al. [108] evaluated the stability of methane−hydrogen structures up to 200 GPa using X-ray diffraction (XRD) and diamond anvil cell (DAC) techniques combined with DFT calculations. They found an abundance of compounds with different hydrogen concentrations. Highly H_2 enriched mixtures led to the formation of hexagonal $CH_4(H_2)_2$ above 5 GPa. In CH_4−rich mixture, tetragonal $(CH_4)_2H_2$ formed, which undergoes hardening of the H_2 intramolecular vibrational mode with pressure. All the compounds are stable up to 160 GPa. For a better understanding, Fig. 1.1 presents the formation of all reported compounds formed as a function of H_2 concentration.

1.4 Linear mixing approximation (LMA)

The standard procedure to study planetary properties is to solve the structure equations [25, 26, 109]. Standard three−layer models are used as long as accurate gravity data from an orbiter mission are unavailable. However, one of the basic input is the equation of state of the relevant materials. Although our understanding of pure species shapes our perception of the planet to some extent, in reality, these planets consist of different materials in varying compositions. Therefore, the additive volume rule at constant pressure and temperature, i.e., the linear mixing approximation (LMA), is applied. The LMA allows the density ρ_{LM} and specific internal energy u_{LM} of the mixture to be extracted

from the following relations, based on the work of DeMarcus [110] and Peebles [111]:

$$\frac{1}{\rho_{\mathrm{LM}}(p,T)} = \sum_{i=1}^{N} \frac{\xi_i}{\rho_i(p,T)}, \tag{1.5}$$

$$u_{\mathrm{LM}}(p,T) = \sum_{i=1}^{N} \xi_i u_i(p,T) \tag{1.6}$$

ξ_i is the mass fraction, i.e., $\xi_i = \frac{m_i}{\sum^N m_i}$.
The deviation of the density and specific internal energy from the real mixture is obtained via:

$$\Delta\rho(p,T) = \frac{\rho_{\mathrm{LM}}(p,T)}{\rho_{\mathrm{Real}}(p,T)} - 1, \qquad \Delta u(p,T) = u_{\mathrm{Real}}(p,T) - u_{\mathrm{LM}}(p,T) \tag{1.7}$$

There are several mixing rules exists, however, the LMA performs the best as indicated by work on H-He mixtures [112] and its dilution with high Z elements such as C, N, O, Si, and Fe [113]. It also performs extremely well for C_2H_3 as a mixture of carbon and hydrogen [114]. In that light, we find this approach well suited for our study, and we discuss the deviations and the corresponding underlying reasons in Sec. 5.1.

1.5 Aim and Outline of this thesis

Despite the CH_4-H_2 compound signatures being detected as a by−product in many studies of hydrocarbons under planetary conditions, there were very few theoretical or experimental investigations. Hence, this work is concerned with mixtures of CH_4 and H_2 under WDM conditions typical for planets such as Uranus, Neptune, and Neptune-like exoplanets. The subsequent section 2.1 lays out the theoretical foundations of density functional theory molecular dynamics (DFT−MD), which is the method of choice in this thesis. We start by addressing the challenges in quantum many–body calculations, explaining means to solve it by decoupling ionic and electron dynamics and discuss foundational pillars of DFT. We then report a technical description of the plane−wave based code VASP. Subsequently, to analyze the data from VASP, additional computational theoretical models including essential technical details of data analysis are discussed in chapter 3. The chapter comprises the construction of EOS, including the pair distribution function and diffusion coefficients. Furthermore, section 3.3 outlines a method to calculate the electronic band gap and conductivities. The next section 4.1 discusses a novel technique, Stochastic density functional theory molecular dynamics (sDFT−MD) to decrease the computational complexity of traditional DFT using stochastic vectors and statistical sampling. In chapter 5, the main results of the work are outlined, which are contained in the publication in chapter 6. Finally, the thesis concludes with the complete set of EOS for the mixture with hydrogen molecular fraction, $\mathcal{X}_{H_2} = 0.116$, and the results of the convergence test for the simulation are given in Appendix A.

2. Methodology

One of the most challenging problems in physics is understanding the properties, structure, and dynamics of many-body systems. All the properties of a system are rooted in the interaction between the building blocks of our universe. Although specific examples of classical theory apply to quantum particles to some extent, the classical description falls short of completely describing reality.

2.1 Many−body problem

The *time−dependent* Schrödinger equation [115],

$$i\hbar\frac{\partial}{\partial t}\psi(\{\mathbf{r}_i,\mathbf{R}_J\};t)=\hat{H}\psi(\{\mathbf{r}_i,\mathbf{R}_J\};t), \tag{2.1}$$

describes the properties of every non-relativistic quantum mechanical particle. $\hat{H}$ is the Hamiltonian, $\hbar$ is the reduced Planck's constant, ψ is the wave function. The Schrödinger equation describes the evolution of the electronic coordinates $\mathbf{r}_i$ and ionic coordinates $\mathbf{R}_J$ at time t. Using the method of separation of variables [116], Eq. (2.1) can be split to obtain the *time−independent* Schrödinger equation,

$$\hat{H}\psi(\mathbf{r}_i,\mathbf{R}_J)=E\psi(\mathbf{r}_i,\mathbf{R}_J). \tag{2.2}$$

The Hamiltonian consists of kinetic and potential energy parts in the absence of external fields, i.e.,

$$\hat{H}=\hat{T}_e+\hat{T}_n+\hat{V}_{e-e}+\hat{V}_{e-n}+\hat{V}_{n-n}, \tag{2.3}$$

where $\hat{T}_n$, $\hat{T}_e$ are the kinetic energy operators of ions and electrons. The interactions between electrons is described by $\hat{V}_{e-e}$, electron-ion $\hat{V}_{e-n}$, and ion-ion $\hat{V}_{n-n}$.
The individual terms are given by:

$$\begin{aligned}
&\hat{T}_n=-\sum_{J}^{N_n}\frac{\hbar^2}{2M_J}\nabla_J^2;\quad \hat{T}_e=-\sum_{i}^{N_e}\frac{\hbar^2}{2m_e}\nabla_i^2;\quad \hat{V}_{e-e}=\frac{1}{4\pi\epsilon_0}\sum_{\substack{i,j\\ i\neq j}}^{N_e}\frac{e^2}{|\mathbf{r}_i-\mathbf{r}_j|};\\
&\hat{V}_{n-n}=\frac{1}{4\pi\epsilon_0}\sum_{\substack{I,J\\ I\neq J}}^{N_n}\frac{Z_IZ_Je^2}{|\mathbf{R}_I-\mathbf{R}_J|};\quad \hat{V}_{e-n}=-\frac{1}{4\pi\epsilon_0}\sum_{i}^{N_e}\sum_{I}^{N_n}\frac{Z_Ie^2}{|\mathbf{r}_i-\mathbf{R}_I|},
\end{aligned} \tag{2.4}$$

where M_I, m_e, ϵ_0, and Z_I denote the mass of ions and electrons, the vacuum permittivity, and charge of the nuclei, respectively.

However, solving the *time-independent* Schrödinger equation, Eq. (2.2), is not feasible for many−particle systems. A more detailed comprehension of Schrödinger's equation can be found in Refs. [117–119], and for a quick yet detailed read, see David Tong's lecture series [120].

2.2 Born-Oppenheimer Approximation

Eq. (2.1) can be analytically solved for a few cases, such as the ground state hydrogen atom and the harmonic oscillator, and can also describe quantum tunneling phenomena. However, technical problems arise as the number of particles increases. A simplification is required, and the first step is to make the Born-Oppenheimer approximation [121]. It assumes that electron movements are almost instantaneous compared to ionic movements. This is due to nuclei being at least 1800 times heavier than electrons, and thus, electrons respond faster than ions to external perturbations.
As a result, a complete basis set in Hilbert space [122] can be expressed in the form of Eq. (2.5), where the electronic eigenvector depends on the ionic positions $\mathbf{R}_J$ as parameters:

$$\psi(\mathbf{r}_i, \mathbf{R}_J, t) = \phi_k^e(\mathbf{r}_i; \mathbf{R}_J)\Theta_I(\mathbf{R}_J, t). \tag{2.5}$$

Therefore, the electronic Hamiltonian becomes:

$$\hat{H}_e\phi_k^e(\mathbf{r}_i; \mathbf{R}_j) = E_k\phi_k^e(\mathbf{r}_i; \mathbf{R}_j), \tag{2.6a}$$

$$[\hat{T}_e + \hat{V}_{e-e} + \hat{V}_{e-n}]\phi_e(\mathbf{r}_i; \mathbf{R}_J) = E_e(\mathbf{R}_J)\phi_e(\mathbf{r}_i, \mathbf{R}_J). \tag{2.6b}$$

Here, ϕ_k^e represents the orthonormal set of electronic eigenvectors. E_k denotes the corresponding energy eigenvalue of eigenstate k, which depends on the ionic coordinates $\mathbf{R}_J$. The dynamics of the nuclei can then be evaluated using the relation

$$i\hbar\frac{\partial}{\partial t}\Theta_I(\mathbf{R}_J; t) = [\hat{T}_n + \hat{V}_{n-n} + E_e(\mathbf{R}_j)]\Theta_I(\mathbf{R}_J; t). \tag{2.7}$$

Eqs. (2.6b) and (2.7) allow us to treat both subsystems separately while accounting for their interaction through the Born-Oppenheimer energy surface $E_e(\mathbf{R}_J)$. When combined with the approaches discussed in Sec. 2.1, this methodology provides a framework for calculating the properties of many-particle systems. Techniques such as the Hartree-Fock method serve as foundational methods for solving electronic structure problems. One of the most successful approaches is density functional theory, particularly when combined with molecular dynamics, as proposed by Car and Parrinello [123].

2.3 Density Functional Theory

The foundational framework proposed by Born and Oppenheimer [121] laid the groundwork for numerous approaches to solving complex many-body electronic structure problems, in which electrons are treated as moving within the static potential generated by the nuclei. Innovative methodologies emerged to tackle this intricate issue, notably through the expansion of Slater determinants [124], with the Hartree-Fock method [125] representing the most rudimentary approach. Sophisticated techniques such as Path Integral Monte Carlo (PIMC) [43–45] facilitate the extraction of eigenvalues for Eq. (2.2) in multi-body contexts. Nevertheless, deriving solutions through these methods can become complex and challenging, making it difficult to analyze larger system with higher degrees of freedom.

To overcome this issue, Thomas and Fermi (1927)[1] [126–128] proposed an approximation, employing the electronic density as variable for a homogeneous electron gas,

$$n(\mathbf{r}) = N_e \int d\mathbf{r}_1 .... \int d\mathbf{r}_{N_e-1} \left|\psi_e(\mathbf{r}_1 .....\mathbf{r}_{N_e-1})\right|^2 , \tag{2.8}$$

ensuring normalization to the total number of electrons within the system.

$$N_e = \int d\mathbf{r} n(\mathbf{r}). \tag{2.9}$$

However, this simplistic approximation struggles to accurately describe the bonding interactions between atoms that lead to molecule formation, and neglects the important exchange and correlation effects influencing electrons, as dictated by Pauli's exclusion principle.

Although the Thomas–Fermi approach provided an important starting point, Hohenberg and Kohn [129] substantially refined DFT, providing a robust theoretical foundation. They introduced two key theorems that form the backbone of the DFT framework and are given below,

Theorem 1: *The external potential is a unique functional of the electron density $n(\hat{r})$. Consequently, since $\hat{V}_{e-n}$ determines the electronic Hamiltonian, $\hat{H}_e = \hat{T}_e + \hat{V}_{e-n} + \hat{V}_{e-e}$, the many-particle ground state is a unique functional of $n(\boldsymbol{r})$.*

Theorem 2: *The Hohenberg−Kohn functional, $J_{HK}[n'(\boldsymbol{r})] = T_e[n'(\boldsymbol{r})] + V_{e-e}[n'(\boldsymbol{r})]$, yields the ground state of energy, if and only if the electron density $n'(\boldsymbol{r})$ is the true electron density $n(\boldsymbol{r})$.*

[1] For a comprehensive discourse encompassing historical context, enhancements, and applications, refer to: *Larry Spruch, Pedagogic notes on Thomas-Fermi theory (and on some improvements): Atoms, stars, and the stability of bulk matter, Rev. Mod. Phys.* ***63****, No.1 (Jan. 1991), pp. 151–209.*

In a nutshell, the electron density $n(\mathbf{r})$ is used to determine the number of electrons and the external potential $\hat{V}_{e-n}$. Hence, the ground state energy can be expressed as a functional of density as shown in Eq. (2.10)

$$E[n(\mathbf{r})] = T_e[n(\mathbf{r})] + V_{e-n}[n(\mathbf{r})] + V_{e-e}[n(\mathbf{r})] \tag{2.10}$$

$$= V_{e-n}[n(\mathbf{r})] + J_{HK}[n(\mathbf{r})] \tag{2.11}$$

where $J_{HK} = T_e[n(\mathbf{r})] + V_{e-e}[n(\mathbf{r})]$ is the Hohenberg−Kohn functional [129]. Although this simplifies the calculation from having $3N_e$ degrees of freedom to N_e degrees of freedom, an essential part of electronic interaction has to be approximated, which will be discussed in the next few sections.

Kohn and Sham [130] utilized the Hohenberg−Kohn theorems to give a scheme for calculating physical observables. At the heart of this scheme lies an *Ansatz* that maps the interacting many-body system onto a non-interacting system, ensuring the density of the non-interacting system, the Kohn-Sham density, equals the original density of the interacting system.

$$n_{KS}(\mathbf{r}) = n(\mathbf{r}). \tag{2.12}$$

This assumption creates independent particle equations that can be solved more easily, including all many-body effects as an exchange-correlation functional. The electron-electron interaction hence can be decomposed into the Hartree interaction V_H and the unknown non-ideal interaction V_{xc} (see Eq. (2.13)). Similarly, the kinetic energy of the electrons can be written in two parts, (i) $\hat{T}_R\,[n(\mathbf{r})]$ is the kinetic energy of the reference system and (ii) the unknown kinetic part $\hat{T}_{xc}$, given in Eq. (2.14). Here, R represents the non-interacting reference system,

$$\hat{V}_{e-e} = \hat{V}_H + \hat{V}_{\text{xc}}, \tag{2.13}$$

$$\hat{T}_e = \hat{T}_R + \hat{T}_{\text{xc}}. \tag{2.14}$$

The non-interacting reference kinetic energy is given by

$$\hat{T}_R = -\frac{\hbar^2}{2m_e}\sum_i f_i \nabla_i^2, \tag{2.15}$$

with f_i being the occupation probability, which is, in case of electrons, the Fermi-Dirac distribution [131],

$$f_i = \frac{1}{e^{\beta(E_i-\mu)}+1} \quad ; \quad \beta = \frac{1}{k_B T}. \tag{2.16}$$

Here, μ is the chemical potential and ϵ_i is the energy of the i^{th} state.

The Kohn-Sham approach to the fully interacting system is to write the Hohenberg−Kohn

equation for the ground state as a functional,

$$\begin{aligned} E_e &= V_{e-e} + V_{e-n} + T_e \\ &= V_H[n(\mathbf{r})] + V_{\text{xc}} + V_{e-n} + T_R[n(\mathbf{r})] + T_{\text{xc}} \\ &= V_H[n(\mathbf{r})] + V_{e-n} + T_R[n(\mathbf{r})] + E_{\text{xc}}, \end{aligned} \tag{2.17}$$

where

$$V_H = \frac{1}{2}\frac{e^2}{4\pi\epsilon_0}\int\int d\mathbf{r}_1 d\mathbf{r}_2 \frac{n(\mathbf{r}_1)n(\mathbf{r}_2)}{|\mathbf{r}_1 - \mathbf{r}_2|}, \tag{2.18}$$

$$V_{e-n} = -\sum_{j=1}^{N}\frac{Z_j e^2}{4\pi\epsilon_0}\int d\mathbf{r}\frac{n(\mathbf{r})}{|\mathbf{r} - \mathbf{R}_j|}. \tag{2.19}$$

Comparing the Kohn−Sham (Eq. (2.17)) and Hohenberg−Kohn (Eq. (2.11)) energy equations, we find that E_{xc} is the difference of the kinetic and internal energy between the interacting system and the fictitious KS *Ansatz* with the electron−electron interaction replaced by the Hartree energy. i.e:

$$E_{xc}[n(\mathbf{r})] = J_{HK}[n(\mathbf{r})] - (V_H[n(\mathbf{r})] + T_R[n(\mathbf{r})]). \tag{2.20}$$

However, a universal functional of E_{xc} is not known. Approximate approaches make the KS method an essential tool to calculate ground state properties. A more detailed discussion of DFT can be found in Refs. [131–139].

2.3.1 Kohn-Sham formalism at finite temperatures

As it is, the DFT version put forward by Hohenberg-Kohn only works for systems at $T = 0$ K. However, information about electronic structure is needed, as the impact of finite temperatures on electrons plays an important role in phenomena such as the heating of solids via laser fields, in WDM, for dynamo effects in giant planets, phase transitions, shock waves, and hot plasmas. Therefore, Mermin extended DFT to finite temperature [140]. This meant that the free energy of the electronic system, F_e, needs to be minimized:

$$F_e[n(\mathbf{r})] = E_e[n(\mathbf{r})] - TS[n(\mathbf{r})], \tag{2.21}$$

where T and $S[n(\mathbf{r})]$ represent the electronic temperature kept at the ionic temperature using a heat reservior and entropy, respectively. The entropy can also be split into two parts, as $S[n(\mathbf{r})] = S_R[n(\mathbf{r})] + S_{xc}[n(\mathbf{r})]$, and the non-interacting entropy functional is given as

$$S_R = -k_B\sum_{i=1}^{\infty}[f_i \ln f_i + (1 - f_i)\ln(1 - f_i)]. \tag{2.22}$$

The free energy functional modifies into

$$F_e[n(\mathbf{r})] = V_H[n(\mathbf{r})] + V_{xc}[n(\mathbf{r})] + V_{e-n}[n(\mathbf{r})] + T_R[n(\mathbf{r})] + T_{xc}[n(\mathbf{r})] - T(S_R[n(\mathbf{r})] + S_{xc}[n(\mathbf{r})]). \tag{2.23}$$

The free energy exchange-correlation functional then follows,

$$F_{xc}[n(\mathbf{r})] = V_{xc}[n(\mathbf{r})] + T_{xc}[n(\mathbf{r})] - TS_{xc}[n(\mathbf{r})]. \tag{2.24}$$

The modified free energy functional (Eq. (2.23)) becomes

$$F_e[n(\mathbf{r})] = V_H[n(\mathbf{r})] + V_{e-n}[n(\mathbf{r})] + T_R[n(\mathbf{r})] - TS_R[n(\mathbf{r})] + F_{xc}[n(\mathbf{r})]. \tag{2.25}$$

All terms in Eq. (2.25) are exact except for the free energy exchange-correlation functional F_{xc}. The effective potential, V_{eff} in which the electrons exist originates from the variation of the free energy functional with respect to the electron density $n(\mathbf{r})$,

$$V_{\text{eff}}[n(\mathbf{r})] = V_H[n(\mathbf{r})] + V_{e-n}[n(\mathbf{r})] + \frac{\delta F_{xc}}{\delta n(\mathbf{r})}. \tag{2.26}$$

If the i^{th} state of the reference one electron system has energy ϵ_i in the Kohn-Sham orbital $\phi_i(\mathbf{r})$ then the electron density results from

$$n(\mathbf{r}) = \sum_{i=1}^{\infty} f_i |\phi_i(\mathbf{r})|^2, \tag{2.27}$$

with the effective Schrödinger equation of the i^{th} state Kohn-Sham orbital [130] follows

$$\left[-\frac{\hbar^2}{2m_e}\nabla^2 + V_{\text{eff}}\right]\phi_i(\mathbf{r}) = \epsilon_i \phi_i(\mathbf{r}). \tag{2.28}$$

Eqs. (2.26), (2.27), and (2.28) describe the fictitious one electron system in a self-consistent manner. The ground state of the system is obtained via solving the above equations iteratively, determining the ground state electronic density and enabling the calculation of observable quantities.

2.3.2 Plane waves and pseudopotentials

For electrons under the influence of a static and periodic potential, such that $V(\mathbf{r}+\hat{\mathbf{T}}) = V(\mathbf{r})$, where $\hat{\mathbf{T}}$ is the translation operator, the potential can be expressed as Fourier expansion $V(\mathbf{r}) = \sum_{\mathbf{G}} V_{\mathbf{G}} e^{i\mathbf{G}\cdot r}$. Here $\mathbf{G}$ defines the reciprocal lattice and $V_{\mathbf{G}}$ are the Fourier coefficients.

This results in the wave function taking the form

$$\phi_i(\mathbf{r},\mathbf{k}) = u_i(\mathbf{r},\mathbf{k})e^{i\mathbf{k}\cdot\mathbf{r}}. \tag{2.29}$$

Eq. (2.29) is a periodic function that satisfies $u_i(\mathbf{r}+\hat{\mathbf{T}},\mathbf{k}) = u_i(\mathbf{r},\mathbf{k})$, $\mathbf{k}$ is a vector in first Brillouin zone and i enumerates over all states. Using Bloch's theorem [141], the KS orbitals $\phi_i(\mathbf{r},\mathbf{k})$ at a given wave vector $\mathbf{k}$ can be expanded in a plane−wave basis set, as given in Eq. (2.30).

$$\phi_i(\mathbf{r},\mathbf{k}) = \frac{1}{\sqrt{V}}u_i(\mathbf{r},\mathbf{k})e^{i\mathbf{k}\cdot\mathbf{r}} = \frac{1}{\sqrt{V}}\sum_{\mathbf{G}=\mathbf{0}}^{\infty} C_i(\mathbf{G},\mathbf{k})e^{i(\mathbf{k}+\mathbf{G})\cdot\mathbf{r}}, \tag{2.30}$$

where $C_i(\mathbf{G},\mathbf{k})$ are the Fourier coefficents [124, 138, 142] for the i^{th} state.
This reduces the problem to a single cell with periodic boundary conditions [138], where the wavefunctions are represented by Bloch functions (Eq. (2.30)). These functions are expanded in a plane–wave basis set and truncated at a finite energy for the calculations to be tractable. This is achieved by following the inequality Eq. (2.31). However, this truncation leads to an error, making E_{cut} an important convergence parameter.

$$E_{\text{cut}} > \frac{\hbar^2}{2m_e}\left|\mathbf{k}+\mathbf{G}\right|^2. \tag{2.31}$$

The electronic structure is then calculated by replacing the integral over the first Brillouin zone by the sum over KS orbitals evaluated at special $\mathbf{k}$-points such as the Baldereschi Mean Value Point [143] or Monkhorst Pack [144] sampling points. The Kohn-Sham equation with plane–wave expansion in the reciprocal space is given by [145]

$$\sum_{\mathbf{G'}}\left[\frac{\hbar^2}{2m_e}\left|\mathbf{k}+\mathbf{G}\right|^2\delta_{\mathbf{G},\mathbf{G'}} + \hat{V}_{eff}(\mathbf{G}-\mathbf{G'})\right]C_{\mathbf{k}\mu}(\mathbf{G'}) = \epsilon_{\mathbf{k}\mu}C_{\mathbf{k}\mu}(\mathbf{G}). \tag{2.32}$$

Valence wave functions are required to rapidly oscillate near the ion to hold orthogonality to the core states. This requires a large number of Fourier coefficients to describe the wavefunction [138, 145]. Pseudopotentials, such as the projected augmented wave (PAW) [146–149] method, are used to replace the rapidly oscillating wave function with a smooth wave function within an augmented sphere of radius r_c. Outside this sphere, the pseudo orbitals behave identical to the exact orbitals with the pseudo wave functions connected to the KS orbitals through projection operators [146, 147], making the simulation of real materials feasible.

2.3.3 Approximation of the exchange-correlation functional

The beauty of DFT is its requirement of very few parameters and its principal exactness. All terms have analytical functionals except for the exchange-correlation (XC) term F_{xc} (see Eq. (2.24)), which is defined as the difference between analytically known energies and some quantities which are numerically evaluated. In practice, however, F_{xc} has to be approximated. The quality of the chosen XC−functional matters a great deal, as it has direct significant impact on the quality of the simulations. The temperature effect

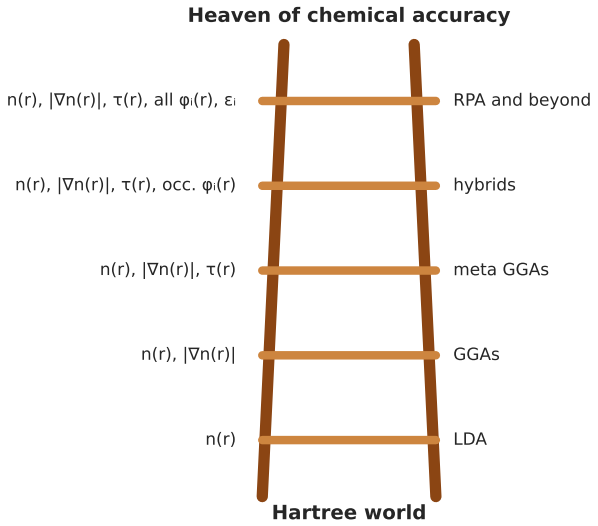


Figure 2.1.: *Jacob's Ladder* of exchange-correlation functionals [150]

on XC−functionals has been neglected for a very long time and only recently gathered some attention. For the most part the free−energy XC−functional is approximated to the XC−functional of ground state DFT, $F_{xc} = E_{xc}$. The ground state functionals are well proven to predict thermodynamic properties of WDM, which agrees very well with experiments. There are many ground state functionals with their own level of accuracy and computational cost. To better understand the accuracy see Fig. 2.1 which is a popular way to categorize density functional approximations dubbed as "Jacob's ladder". The lowest rung is the LDA (Local Density Approximation) [151, 152] which treats inhomogeneous electrons as homogenous. It works very well for weakly interacting electrons or free electronic systems but fails to describe properties such as molecules, bonding etc. Apart from LDA which uses only the information of electron density $n(\mathbf{r})$, the generalized gradient approximation (GGA) on the second rung takes the gradient of density, e.g., $\nabla n(\mathbf{r})$, as well as the density into account:

$$E_{xc}^{\mathrm{GGA}}[n(\mathbf{r})] = \int d\mathbf{r} n(\mathbf{r}) \epsilon_{xc}^{\mathrm{GGA}}[n(\mathbf{r}), \nabla n(\mathbf{r})]. \tag{2.33}$$

On the third rung, meta GGAs depend on the use of second derivates of the density, i.e., $\nabla^2 n(\mathbf{r})$, as well as a quantity referred to as KS kinetic energy density, $\tau(\mathbf{r}) = \frac{1}{2}\sum_{i=1}^{N} |\nabla\varphi_i(\mathbf{r})|^2$. Above that, we find functionals that depend on occupied KS orbitals i.e. hybrid functionals, and on unoccupied KS orbitals, such as the random−phase approximation (RPA) [153], GW methods [154, 155], etc.
This work uses the XC−functional proposed by Perdew, Burke, and Ernzerhof (PBE) [156]. It provides a good balance between accuracy and computational cost. PBE works very well in estimating lattice constants, binding energies, and thermodynamical properties such as the enthalpy compared to LDA [157] but it underestimates the band gap due to its self−interaction error. This underestimation of the band gap is overcome by hybrid functionals such as HSE [158–160]. These functionals are extremely computationally demanding and very few DFT−MD work has been done [64] with HSE in the WDM regime, mostly for transport properties calculations.

2.4 Molecular Dynamics Simulation

The KS equations only regard the electronic properties of systems in which the ions/nuclei are in static configurations. The positions of the nuclei are a parameter in the KS equations rather than being a variable. As mentioned previously, the masses of nuclei are very high compared to the mass of electrons, resulting different in timescales of the respective dynamics. In this section, we focus on MD simulations where the dynamics of the nuclei are governed by the Hellmann–Feynman forces [161, 162], calculated using DFT. We propagate the nuclei in time, considering them as classical particles, using Newton's equation of motion. The simulation box of volume V consists of arranged particles and is then repeated in all directions to mimic an infinite system and minimize surface effects.

$$m_I \frac{d^2}{dt^2}\mathbf{r}_I = \underbrace{-\nabla_I E_{nn}\big(\{\mathbf{r}_I\}\big)}_{\mathbf{F}_{I,nn}} + \underbrace{-\nabla_I E_m\big(\{\mathbf{r}_I\}\big)}_{\mathbf{F}_{I,ne}} - m_I \dot{\mathbf{R}}_I \frac{\dot{s}}{s}. \tag{2.34}$$

The resulting force on the ions (Eq. (2.34)) consists of three parts. The first term, $\mathbf{F}_{I,nn}$, denotes the contribution due to nuclei-nuclei interaction, the second term $\mathbf{F}_{I,ne}$, represents the Hellman-Feynman forces [161, 162] of the electrons on the nuclei and the third term $M_I \dot{R}_I \dot{s}/s$ signifies an additional force on the nuclei due to coupling with the heat bath to realise a canonical ensemble. For the heat bath, the Nosé-Hoover thermostat [163, 164] is used. The Hamiltonian of the heat bath is given as

$$H_{\text{bath}} = \frac{1}{2} Q \left(\frac{\dot{s}}{s}\right)^2 + 3(N-1) k_b T \ln s. \tag{2.35}$$

s additionally introduces another degree of freedom, satisfying the equation of motion,

$$Q\ddot{s} = s\sum_{i=1}^{N} M_I \dot{R}_I{}^2 - 3(N-1)k_bTs + Q\frac{\dot{s}^2}{s}. \tag{2.36}$$

Q is the frictional mass parameter. The heat bath maintains the temperature of the system at the desired value by periodically adding or subtracting from the time averaged kinetic energy of the nuclei,

$$\langle T \rangle = \frac{3}{2}(N-1)k_bT. \tag{2.37}$$

The energy coupling is controlled via the characteristic frequency of the thermostat,

$$\omega_T = \sqrt{\frac{6(N-1)K_bT}{Q}}. \tag{2.38}$$

The force due to nuclei-nuclei and nuclei-bath interaction is determined directly from molecular dynamics. Additional insights into the MD are provided in Refs. [136, 165, 166].

2.5 DFT−MD simulations with VASP

The DFT−MD technique is implemented in the **V**ienna **A**b − **I**nitio **S**imulation **P**ackage (**VASP**) [167–170] which is used throughout this work. Fig. 2.2 shows a brief outline of the workflow.

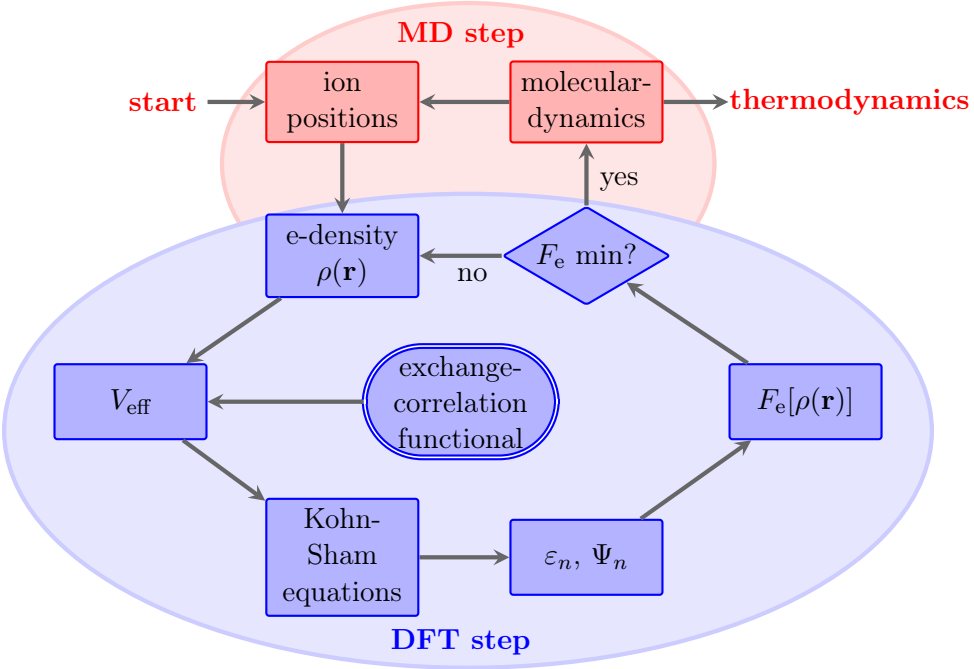


Figure 2.2.: Workflow of a DFT-MD simulation in VASP. Illustration borrowed from the Ph.D. thesis of W. Lorenzen [171]

For a given number of particles N and box size of volume V, the simulation starts by guessing an electron density and calculating the electron free energy from the effective one particle Schrödinger's equation as derived by Kohn and Sham. This process is repeated until the free energy reaches the specified convergence criteria. Then the forces on the nuclei are calculated using the Hellmann−Feynmann theorem. These forces are then embraced into the N_n−Newtonian equations of motion [172] governing the dynamics of nuclei. The positions of the nuclei are updated by integrating the Newton's equations using the Verlet algorithm [136, 173] and these updated positions produce a new updated electron density.
This process is repeated over many MD steps and lets the system evolve dynamically over time. The Nosé−Hoover thermostat [163, 164] maintains the temperature in the simulation. Although this work is done using VASP [167], there are many ab−initio codes such as CASTEP [174], SIESTA [175], ABINIT [176], FHI-AIMS [177], QUANTUM ESPRESSO [178], and many more.

Throughout this study, comprehensive convergence tests with respect to the particle number, **k**-point set and energy cutoff were performed to ensure the convergence of the simulations, which is presented in Appendix A.2. Similar apporaches to ensure the convergence of simulations can also be found in the following Refs. [179, 180].

3. Additional theoretical means

The previous section briefly discusses the means of solving the many−body problem under the effect of high temperature and densities. However, to obtain useful insights of the thermal, caloric, structural and electronic properties at WDM conditions, extensive data analysis of the DFT−MD data is required. In this section, we briefly discuss the theoretical part of obtaining the EOS in tandem with structural properties. We discuss the background of the electronic band gap problem, and we conclude the section with discussing the evaluation of electrical properties using Linear Response Theory (LRT).

3.1 Equation of state (EOS)

For a particular density and temperature, DFT−MD simulations reach thermodynamic equilibrium after some time, resulting in a corresponding $p(\rho, T)$ and $U(\rho, T)$. The EOS is then obtained by doing the same for a series of points on the density−temperature grid. The total pressure p and the internal energy U is obtained from

$$p = \frac{N\rho k_B T}{m} + \langle p_{nn} \rangle + \langle p_e \rangle, \tag{3.1}$$

$$U = \frac{3}{2} N k_B T + \langle E_{nn} \rangle + \langle F[\rho(\mathbf{r})] + T S_R[\rho(\mathbf{r})] \rangle. \tag{3.2}$$

The first term in both the equations is the ideal contribution of the ions. For Eq. (3.1), the second term is due to the interaction between ions and is evaluated using a virial theorem [165, 173]. Finally, the pressure from the electronic system is calculated using an analogous quantum mechanical virial theorem [138, 181, 182]. Please note that all the results presented use the specific internal energy $u(\rho, T)$, which is defined as internal energy divided by total mass, an intensive quantity.

3.2 Structural properties of fluids

External forces can induce phase transitions. Changes in the slopes of the thermal and caloric EOS are indications of such. Usually, this is accompanied by some structural changes of ions and electrons. Here, the pair distribution function and the diffusion coefficient is used alongside the mean square displacement to analyze the structural properties of the concerned phase dictated by pressure and temperature.

3.2.1 Pair distribution function (PDF)

The pair distribution function measures the probability of a species α to find an atom of identical species at distance r. This can be generalized to a two particle distribution by only using radial symmetry [173]:

$$g(\mathbf{r}) = g_{\alpha\beta}(\mathbf{r}) = \frac{V}{4\pi r^2 N_\alpha (N_\beta - \delta_{\alpha\beta})} \left\langle \sum_{j=1}^{N_\alpha} \sum_{j=1}^{N_\beta} \delta(\mathbf{r} - \mathbf{r}_{ij}) \right\rangle . \tag{3.3}$$

Here, N_α and N_β are the particle numbers of respective species, $\mathbf{r}_{ij}$ is the distance between two particles i and j, $\delta_{\alpha\beta}$ is the Kronecker delta, whereas $\delta(\mathbf{r}-\mathbf{r}_{ij})$ is the Dirac delta. For $\alpha = \beta$, i.e., a single species system, an additional summation $j > i$ must be considered. However, calculating the PDF is only possible via theory and simulations. In reality, experiments capture structure factors, which are probed in momentum space. PDFs can be obtained by inverse transforming structure factors. To our knowledge, there are no studies of high-pressure CH_4–H_2 mixtures in fluid phase.

3.2.2 Diffusion coefficient

For an isotropic system, the Green–Kubo formula [173] provides self diffusion coefficents D_α using the auto–correlation function of the velocity vectors $\mathbf{v}$.

$$D_\alpha = \frac{1}{3N_\alpha} \lim_{\tau\to\infty} \int_0^\tau dt \sum_{i=1}^{N} \langle \mathbf{v}_i(t) \cdot \mathbf{v}_i(0) \rangle. \tag{3.4}$$

This formulation provides us results with a typical error of 10 percent. However, it does not provide a clear picture of the mobility of ions over the duration of our simulations,

$$\langle (\Delta R_I)^2 \rangle = \sum_{i=1}^{N} \langle |\mathbf{r}_i(t) - \mathbf{r}_i(0)|^2 \rangle. \tag{3.5}$$

Instead, we use the mean square displacement $\langle (\Delta R_I)^2 \rangle$ to determine the mobility of the ions and to determine the stability of crystal lattices in former works [183, 184].

3.3 Electronic properties

Planetary materials are subjected to extreme conditions in planetary bodies. Electronic properties provide insight into the behavior of materials under WDM conditions, which in turn helps to distinguish phases and phases changes. Here, we outlay the methods, namely the calculation of electronic band gaps, electrical, and thermal conductivities.

3.3.1 Band gap calculation

The estimation of band gaps of semiconductors is a long-standing problem in DFT [185, 186]. It is not only due to the XC potential, but it originates from the mathematical construction of non–interacting, non–physical KS states, yielding the true ground state density of a real many body system from a fictitious one.

At a temperature of absolute zero, the band gap of materials is evaluated by the energy difference between the highest occupied molecular orbital (HOMO) and the lowest unoccupied molecular orbital (LUMO). At finite temperatures, however, the HOMO–LUMO definition loses its meaning due to the smearing of the Fermi edge. However, it predicts the center of the band gap, i.e., the chemical potential in the framework of the VASP code, exactly [187]. This fact is utilized in one of the techniques to calculate the band gap, as HOMO–LUMO are in vicinity of the chemical potential. For high temperatures, smearing of the Fermi function depletes the HOMO and populates the LUMO according to Fermi–Dirac statistics. In this thesis, the evaluation of the band gap is done using the technique developed by Preising and Redmer [179, 188].

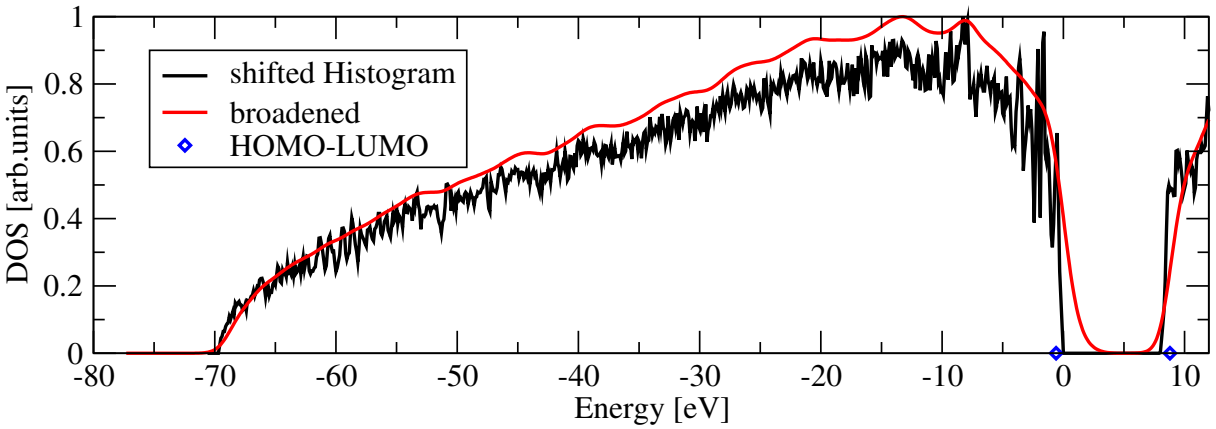


Figure 3.1.: The DOS of helium at $T = 0$ K and $\rho = 10$ g/cm^3 with different evaluation techniques: shifted histogram (Black solid line), broadened (Red solid line), and HOMO−LUMO (Blue diamonds). *(Figure courtesy of Martin Preising's thesis [179])*

Other two approaches are (i) Broadened: Where the band energies are recorded, and a histogram is created, shifting the band energies by the chemical potential, and then multiplied with a Gaussian function having 1% of the Valence Band Width (VBW) [189]. (ii) Shifted histogram: This method is the same as broadened but omits the process of broadening the DOS. Fig. 3.1 shows the variation in using different methods at $T = 0$ K and $\rho = 10$ g/cm^3 with a simulation cell containing 864 helium atoms and a very dense **k**-mesh of 25×25×25 for sampling the Brillouin zone. An upper bound of the histogram results is obtained from HOMO−LUMO. The Broadened method produces a smaller band gap compared to other methods due to the smearing of the DOS compared to the sharp

features of the DOS of the histogram method. [1] Along with these techniques the higher order XC functionals (HSE, SCAN) [190–192] or GW methods [193–195] can improve the estimation of the band gap close to experimental values [196].

The information of the band gap of a system is an important tool in understanding the changes in electronic configurations, such as transitions from a direct to an indirect band gap and vice versa in solids due to external influences [197–200], as well as insulator–to–metal transitions in solids [201–203] and fluids [188, 192, 204]. To properly assess the electronic configuration, we calculate the electronic and thermal conductivity.

3.3.2 Electrical and thermal conductivity

Under the influence of external fields, we observe phenomena of electrical transport, [2] i.e., charge and heat transport. Macroscopically, these non–equilibrium dynamic states obey Ohm's law, stating that a steady-state electric current density $\mathbf{J}$ in the system is directly proportional to the external electric field $\mathbf{E}$ such that $\mathbf{J} = \sigma\mathbf{E}$, where σ is the constant of proportionality also known as electrical conductivity. On the other hand, the thermal conductivity, $\lambda = c_v \tau \langle v_F^2 \rangle /3$, is proportional to the heat capacity (c_v), the mean free path (τ) of the free electrons, and the Fermi velocity (v_F). Historically, two of the most celebrated theories for electrical transport frequently employed to study the electronic dynamics are: Boltzmann transport equation (BTE) [205] and Kubo's quantum-statistical linear response theory (LRT).
In this thesis, we use the latter, as the semi-classical nature and well-defined quasi-particle assumption of BTE breaks down in the WDM regime as quantum degeneracy, strong coupling, and thermal excitation coexist.

Within the framework of LRT and DFT, the general expression for Onsager coefficients [206] is given by

$$L_n(\omega) = \frac{2\pi(-1)^n}{V\omega} \sum_{\mathbf{k}\alpha\beta} \mathbf{Re}\Big(\langle \mathbf{k}\alpha|\mathbf{v}|\mathbf{k}\beta\rangle \otimes \langle \mathbf{k}\beta|\mathbf{v}|\mathbf{k}\alpha\rangle\Big)(f_{\mathbf{k}\alpha} - f_{\mathbf{k}\beta}) \times \left(\frac{\epsilon_{\mathbf{k}\alpha} + \epsilon_{\mathbf{k}\beta}}{2} - h_e\right)^n \delta(\epsilon_{\mathbf{k}\alpha} - \epsilon_{\mathbf{k}\beta} - \hbar\omega)\,, \tag{3.6}$$

where e is the electronic charge, ω is the frequency, V is the volume of the simulation box and α is the sum of the average of contribution from the three spatial directions. $f(\epsilon_{i,\mathbf{k}})$ and $\epsilon_{i,\mathbf{k}}$ are the Fermi distribution function and eigenvalues of the i^{th} Bloch state $|\mathbf{k}\alpha\rangle$ at a wavevector $\mathbf{k}$. Optical routines of VASP allow to calculate the dipole matrix $\langle \mathbf{k}\alpha|\mathbf{v}|\mathbf{k}\beta\rangle$. To integrate the Brillioun zone, a special discrete set of $\mathbf{k}$-points are used with a weighted summation $\sum_{\mathbf{k}} W(\mathbf{k})$.

[1] *For an extensive detail on the above please refer to Preising et al. [188] and the PhD thesis of Martin Preising [179].*
[2] *Here, we neglect the effect of magnetic fields.*

The macroscopic transport coefficients are then determined by the zero frequency ($\omega \rightarrow 0$) value of the Onsager coefficients given by Eq. (3.6). Hence, the electrical and thermal conductivity are determined via

$$\sigma = e^2 \lim_{\omega \to 0} L_0(\omega), \tag{3.7}$$

$$\lambda = \frac{1}{T} \lim_{\omega \to 0} \left(L_2(\omega) - L_1(\omega) L_0^{-1}(\omega) L_1(\omega) \right) . \tag{3.8}$$

Due to the finite size of the simulation box constrained by periodic boundary conditions the spectrum of eigenvalues is discrete. To leviate this unphysical behavior the δ function is replaced by a Gaussian smearing function of finite width [206]. [3]

With the knowledge of the electrical and thermal conductivity, we calculate the Lorenz number given by Eq. (3.9),

$$L = \frac{\lambda}{T\sigma} \left(\frac{e}{k_b} \right)^2 . \tag{3.9}$$

For a degenerate electron gas, this yields a constant $L_0 = \pi^2/3$ (units of e^2/k_b^2) known as Wiedemann-Franz law [208].

Results shown in this work have been thoroughly checked and are well converged. Since it is computationally impossible to calculate electrical conductivity over the complete DFT-MD simulation, 40 to 60 snapshots of the simulation are used depending on the condition and the system.

[3] *For a complete and detailed comprehension refer to Chapter 6: Electron Transport, Conceptual Foundations of Materials, P.B. Allen [207]*

4. Stochastic density functional theory

4.1 Bottelneck of traditional KS-DFT

Kohn−Sham density functional theory is highly successful as an ab initio theory in predicting electronic structure properties of materials and molecules at zero kelvin. For our purposes, finite−temperature KS−DFT fulfils the requirements and has been used extensively for the theoretical study of WDM. However, the computational complications increase with temperature, which restricts the usability of traditional DFT at high temperatures.

Under the KS−"*Ansatz*", the finite temperature density of many electrons system is calculated using Eq. (2.27), which can be written as

$$n(\mathbf{r}) = 2 \times \sum_{k} \left| f_{\beta,\mu}(\epsilon_i)\psi_i(\mathbf{r}) \right|^2 , \tag{4.1}$$

where $f_{\beta,\mu}(\epsilon_i)$ are the eigenvalues of the square root Fermi-Dirac operator $F^{\beta,\mu} \equiv f(H;\beta,\mu)$. The process of extracting eigenvalues $f_{\beta,\mu}(\epsilon_i)$ requires diagonalizing the Hamiltonian matrix, which involves $\Theta(N^3)$ operations and $\Theta(N^2)$ memory [138]. This computational complexity often becomes a barrier to investigate large simulation cells and/or high temperature conditions where large number of unoccupied states are required. For example, in temperatures above 100,000 K other techniques such as the extended KS method, *orbital−free* DFT [38, 39], *Spectral Quadrature* DFT [40, 209], and Stochastic DFT utilised to mitigate some computational cost.

4.2 The Essence of Stochastic DFT (sDFT)

The foundation of this technique is to repeatedly generate specially crafted random variable samples, statistically independent. The idea is to measure a physical quantity (density, forces on nuclei, elastic constants, etc.) without knowing the variable's distribution [210–212].

4.2.1 Random Variables

For a random variable $\mathcal{X}$, the probability distribution is given by $p(\mathcal{X})$, such that the total probability is $\sum_{\mathcal{X}} p(\mathcal{X}) = 1$. Hence, the expected value of the random variable is

$$\mathbf{E}[\mathcal{X}] = \sum_{\mathcal{X}} \mathcal{X} p(\mathcal{X}). \tag{4.2}$$

Any function $f(r)$, also a random variable, and its expected value is given by

$$\mathbf{E}\left[f(\mathcal{X})\right] = \sum_{\mathcal{X}} f(\mathcal{X}) p(\mathcal{X}). \tag{4.3}$$

The variation of the random variable can be calculated from the general expression $\sigma^2[\mathcal{X}] = \mathbf{E}\left[|\mathcal{X}|^2 - |\mathbf{E}[\mathcal{X}]|^2\right]$ and the standard deviation (SD) as $\mathrm{SD} = \sigma^2[\mathcal{X}]$.
The mean, m_I, calculated from the set of sampled random variables $\{\mathcal{X}\}$, is itself a random variable (see Eqn. (4.4)):

$$m_I = \frac{1}{I} \sum_{\alpha=1}^{I} \mathcal{X}_\alpha, \tag{4.4}$$

and the expected value of the mean provides an unbiased estimate for the expected value of $\mathbf{E}[\mathcal{X}]$, i.e, $\mathbf{E}[\mathcal{X}]$=$\mathbf{E}[m_I]$.

Hence, the variance can be shown to decrease with the increment of number of samples.

$$\sigma^2[m_I] = \frac{1}{I}\sigma^2[\mathcal{X}] \Longleftrightarrow \sigma[m_I] = \frac{\sigma[\mathcal{X}]}{\sqrt{I}}. \tag{4.5}$$

However, the formal way of estimating the uncertainty of the mean of a random sample is using the notion of p-level confidence:

$$s_I^2 = \frac{1}{I-1} \sum_{\alpha=1}^{I} (\mathcal{X}_\alpha - m_I)^2. \tag{4.6}$$

4.2.2 Stochastic vectors

The stochastic column vectors χ_k consist of K independent random variables, with the modulus being $|\chi_k| = 1$ with uniform probability. Depending on whether the variables are considered to be real, χ_k is drawn from a uniform distribution of $\{\pm 1\}$, or if complex, a number is obtained from the complex unit circle $e^{i\theta}$, where θ is a random angle between $\{0,$

$2\pi\}$.

$$\chi = \begin{pmatrix} \chi_1 \\ \chi_2 \\ .. \\ .. \\ .. \\ \chi_K \end{pmatrix}. \tag{4.7}$$

Leading to the identity matrix $\mathcal{I}$ to be defined as:

$$\mathbf{E}\left[\chi_k \chi_{k'}^*\right] = \delta_{kk'}. \tag{4.8}$$

This establishes a claim, i.e., the trace of a $K \times K$ matrix A can be expressed as the expected value of the random variable $\chi^\dagger A \chi$ as shown in the following, i.e., the stochastic trace formula [213].

$$\begin{aligned} \mathbf{Tr}[A] = \mathbf{Tr}[IA] = \mathbf{Tr}\,\mathbf{E}[[\chi^\dagger \chi]A] = \mathbf{Tr}[\mathbf{E}[\chi^\dagger \chi A]] \\ = \mathbf{E}[\mathbf{Tr}[\chi^\dagger \chi A]] = \mathbf{E}[\mathbf{Tr}[\chi^\dagger A \chi]] = \mathbf{E}[\chi^\dagger A \chi]. \end{aligned} \tag{4.9}$$

4.2.3 sDFT

sDFT is based on the concept of random wave functions [211],

$$\eta(\mathbf{r}) \equiv \sum_G \tilde{\eta}^{\mathbf{G}} \frac{e^{i\mathbf{G}\cdot\mathbf{r}}}{\sqrt{\Omega}}, \tag{4.10}$$

where the wave function is expressed in a plane-wave basis set such that, $G = \frac{2\pi}{L}(m_x, m_y, m_z)$ is the reciprocal wave vector. Ω is the volume of the simulation cell, $\tilde{\eta}^{\mathbf{G}}$ are the random coefficients (in vector notation), which are obtained from the square root of the Fermi–Dirac operator on the random wave vector [214] (see Eq. (4.7)).

$$\tilde{\eta} \equiv \sqrt{f_{\beta\mu}(H)}\tilde{\chi}. \tag{4.11}$$

Note, the components of the random vectors are based on Euler's formula, with the independent random phases $\theta_{\mathbf{G}} = [0, 2\pi]$. Utilizing the above, it is easy to establish Eq. (4.8) and $\tilde{\eta}^{\mathbf{G}'}\tilde{\eta}^{\mathbf{G}^*}$ acts as an unbiased estimator of the KS density. The electron density can be estimated by

$$n(\mathbf{r}) = 2 \times \mathbf{E}[|\eta(\mathbf{r})|^2]. \tag{4.12}$$

Eq. (4.12) is the heart of stochastic KS-DFT, which describes how to obtain the electron density from KS-DFT eigenstates and eigenvalues by statistically sampling the random variable $|\eta(\mathbf{r})|^2$. For a sample of I independent random vectors $\tilde{\eta}_i$, the density can be

calculated as an average, using Eq. (4.10) and (4.11) [212].

$$n(\mathbf{r}) = 2 \times \frac{1}{I} \sum_{i=1}^{I} [|\eta_i(\mathbf{r})|^2]. \tag{4.13}$$

The important step in this stochastic calculation is the operation of the Fermi–Dirac operator on the random vector Eq. (4.11). Using the Chebyshev expansion, this step can be linearized as shown in the next section.

4.2.4 Chebyshev methods

The rate-determining step as mentioned above (Eq. 4.11) is the evaluation of the Fermi−Dirac operation on the random vector. To linearize the computational scaling of this operation, a sparse representation of the Hamiltonian H is used while expanding the operator $f_{\beta\mu}(H)$ using the Chebyshev expansion [215]. Let $z(H)$ be an operator dependent on the Hamiltonian such that $|\xi\rangle = z(H)\,|\chi\rangle$,

$$|\xi\rangle = \sum_{n=0}^{N_c-1} Z^{(n)}\,|\chi_n\rangle\,, \tag{4.14}$$

where the Chebyshev coefficients are defined by

$$Z^{(n)} = \frac{2}{N_c} \exp\left(i\frac{\pi}{N_c} n \tilde{z}^{(n)}\right). \tag{4.15}$$

An approximation for the length of the Chebyshev expansion is given by

$$N_c \approx \frac{3d}{4} \times \beta \times \Delta E, \tag{4.16}$$

where $\Delta E = \frac{E_{\max} - E_{\min}}{2}$ and $E_{\max,\min}$ is the largest and smallest eigenvalue of H [214]. Usually, the N_c is chosen to be large such that $\left|Z^{(n)}\right|$ are smaller than the threshold value of 10^{-d}. Due to the recurrence relationship between the Chebyshev polynomials [216] presented in Eq. (4.17), the necessity to store and operate on a large number of coefficients of KS-orbitals is reduced to keeping only three consecutive Chebyshev polynomials in memory at any given time.

$$\begin{aligned} |\chi_n\rangle &= 2H_s\,|\chi_{n-1}\rangle - |\chi_{n-2}\rangle\,; \;\; n \geq 2, \\ |\chi_0\rangle &= |\chi\rangle\,, \\ |\chi_1\rangle &= H_s\,|\chi_0\rangle\,. \end{aligned} \tag{4.17}$$

This enables the iterative computation of the Chebyshev vectors.

Energy windows

Using the *Energy windows* technique [217], the above is calculated iteratively. We define N_w chemical potentials Eq. (4.18) and the energy windows projections Eq. (4.19):

$$\mu_{N_w} \equiv \mu \geq \mu_{N_w-1} \geq .... \geq \mu_1, \tag{4.18}$$

$$\begin{aligned} z_w(H) &= \sqrt{f_{\beta\mu_m} - f_{\beta\mu_{m-1}}}, \quad m = 2, ..., N_w, \\ z_1(H) &= \sqrt{f_{\beta\mu_1}}. \end{aligned} \tag{4.19}$$

Between the chemical potentials, each of these functions delineates a different energy range and the Fermi–Dirac projector is produced by aggregating the square of each function.

$$f_{\beta\mu}(H) = z_{N_w}(H)^2 + z_{N_w-1}(H)^2 + ... + z_1(H)^2. \tag{4.20}$$

Hence, for any one-body operator A, the expectation value is obtained by summing up the contribution from each different energy window,

$$\langle A \rangle = \sum_{m=1}^{N_w} \mathbf{Tr}\left[z_m(H) A z_m(H)\right], \tag{4.21}$$

with the equivalent stochastic expression

$$\langle A \rangle = \sum_{m=1}^{N_w} \mathbf{E}\left[\langle \xi_m | A | \xi_m \rangle\right]. \tag{4.22}$$

Importantly, this procedure helps to reduce fluctuations in the expectation values as ξ_m and $\xi_{m'}$ occupy non overlapping energy windows.

Chebyshev moments

The trace of Chebyshev polynomial is called Chebyshev trace $M_n = \mathbf{E}\left[\langle \chi | \chi_n \rangle\right]$ [214]. Calculating the moments allows to compute the trace of any function of the KS Hamiltonian H using

$$\mathbf{Tr}\left[z(H)\right] = \sum_{n=0}^{N_c-1} Z^{(n)} M_n. \tag{4.23}$$

This is extremely useful for calculating the number of electrons N_e,

$$N_e = 2 \times \sum_{n=0}^{N_c-1} P_{\beta\mu}^{(n)} M_n. \tag{4.24}$$

To calculate the chemical potential μ, a numerical root-searching algorithm is employed. As the moments are independent of μ, calculating and storing them once is sufficient while

a single fast Fourier transform is enough to calculate the Chebyshev coefficients for any value of μ.
Other quatities such as the non–interacting electron entropy is calculated via a stochastic form of Eq. (2.22),

$$S_s = 2 \times \sum_{n=0}^{N_c-1} S_{\beta\mu}^{(n)} M_n, \tag{4.25}$$

where $S_{\beta\mu}^{(n)}$ are the Chebyshev coefficients of the function $s_{\beta\mu}^{(n)} = -[f_{\beta\mu}(\epsilon)\log f_{\beta\mu}(\epsilon) + (1 - f_{\beta\mu}(\epsilon))(1 - \log f_{\beta\mu}(\epsilon))]$. The orbital energy is given by

$$E_{\text{orb}} = 2 \times \sum_{n=0}^{N_c-1} E_{\beta\mu}^{(n)} M_n, \tag{4.26}$$

where $E_{\beta\mu}$ are the Chebyshev coefficients to $e_{\beta\mu} = f_{\beta\mu}(\epsilon)\epsilon$.

4.3 Langevin dynamics

Using Langevin equations of motion (EOM) and the stochastic force for a given atomic nuclei configuration, the series of coordinates and momenta are sampled. From these samples, thermodynamic properties of the system are evaluated. This requires solving the following Langevin EOM:

$$\begin{aligned} \dot{\mathbf{P}}(t) &= \psi(\mathbf{R}(t)) - \gamma\mathbf{P}(t), \\ \dot{\mathbf{R}}(t) &= M^{-1}\mathbf{P}(t), \end{aligned} \tag{4.27}$$

where M^{-1} and γ are the diagonal matrices of the inverse nuclei mass and friction coefficient, respectively. Using a time–discretized solver [218] for the stochastic differential equation results in a set of discretized trajectories of atomic configurations $\mathbf{R}^{(n)} = \mathbf{R}(n\Delta\tau)$ for $n = 1, ...N_T$, as well as their associated momenta $\mathbf{P}^{(n)} = \mathbf{P}[n - \frac{1}{2}\Delta\tau]$, where $\Delta\tau$ is the time step. Finally, the complete evolution of the phase space trajectory is obtained from the following steps:

$$\begin{aligned} \mathbf{P}^{(n+1)} &= e^{-\gamma\Delta\tau}\mathbf{P}^{(n)} + \left(\frac{1 - e^{-\gamma\Delta\tau}}{\gamma}\right)\psi(\mathbf{R}^{(n)}), \\ \mathbf{R}^{(n+1)} &= \mathbf{R}^{(n)} + M^{-1}\mathbf{P}^{(n+1)}\Delta\tau. \end{aligned} \tag{4.28}$$

For the limit $\Delta\tau \to 0$, a Langevin trajectory is obtained, while the frictional matrix γ is evaluated using the fluctuation dissipation theorem.

$$\sigma^2 = \frac{\gamma\Delta\tau/2}{\tanh(\gamma\Delta\tau/2)} \cdot \frac{2\gamma M}{\beta}. \tag{4.29}$$

For a detailed breakdown refer to the following articles [210–212, 219–221].

5. Results

5.1 $CH_4 + H_2$

Diamond rain is believed to occur in the deep interior of Neptune-like planets where a significant amount of methane coexists with ammonia and water. The potential decomposition of methane under the extreme pressure-temperature conditions of ice giants and the separation of carbon and hydrogen could lead to the formation of diamonds that sink towards the core. This intriguing process forms the motivation of our research.
Employing the computational tools mentioned in the previous two chapters, the mixture of methane and hydrogen is investigated. The results are published in papers I [204] and II [222]. Paper III [214] presents the efficacy and accuracy of FT-sDFT combined with Langevin dynamics, using pure hydrogen as test bed.

5.1.1 Evaluation of the Linear Mixing Approximation (LMA)

Our investigation starts with a binary mixture of methane and hydrogen within a density-temperature grid bounded by 0.74 g/cm^3 $\leq \rho \leq$ 3.70 g/cm^3 and 700 K $\leq T \leq$ 16000 K. Figure A.1 presents the thermal and caloric EOS. We observed significant changes in the slope in both thermal and caloric EOS of the mixture, characterizing the dissociation.

Apart from EOS of the mixture, we also studied the validity of the linear mixing approximation up to 16000 K and 1 TPa. The EOS was obtained for pure systems, and the mixture was interpolated using Akima splines [223] for pressures along the isotherms.

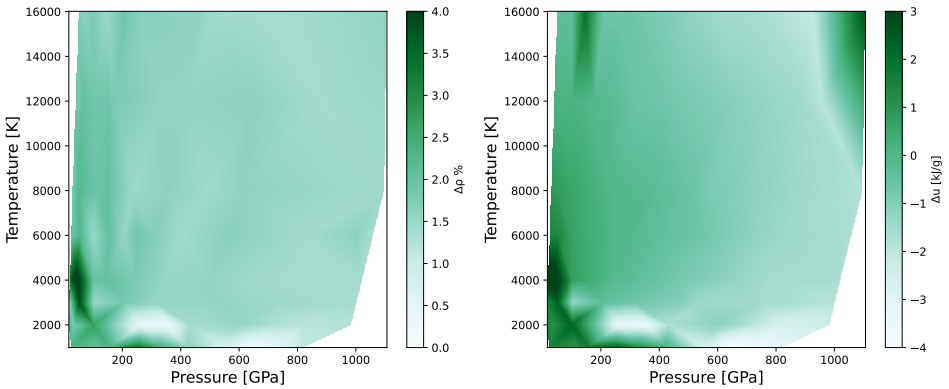


Figure 5.1.: Deviation in density $\Delta\rho$ and specific internal energy Δu (kJ/g) of the real binary mixture from the linear mixing approximation.

Temperatures were linearly interpolated. The deviations in specific internal energy and density were calculated using the LMA. Fig. 5.1 shows the resulting deviations; we find moderate deviation throughout, with the maximum deviation arising between 2000 − 4000 K and low pressure where methane molecules are intact and hydrogen molecules disintegrate, leading to a deviation of 3 kJ/g in specific internal energy. We also observe the maximum deviation of −4 kJ/g at 2000 K and between 200 − 400 GPa. Deviations in density are observed to be 4% around 4000 K. It is clear that the dissociation of methane and hydrogen molecules occurs, however the deviations observed in density cannot be used directly to infer a specific phase of the mixture. Bethkenhagen et al. [224] observed the same deviations in $P - T$ space for binary and ternary mixtures of CH_4−NH_3−H_2O. To delve deeper into the observed changes in the slope of EOS and the deviations of the mixture of CH_4−H_2, we discuss the structural changes by evaluating the self−diffusion coefficients and pair distribution function as presented in the next section.

5.1.2 Structural Changes

Fig. 5.2 presents the findings of self−diffusion coefficients in the mixture. For both species, temperature and density show significant effects on the diffusion coefficients. However, the diffusion coefficient of hydrogen molecules in the mixture shows a significant minimum at 2000 K and 1.58 g/cm^3, indicating the dissociation of hydrogen molecules but not the dissociation of methane as mentioned in paper I [204]. This minimum becomes less pronounced as the temperature is increased and vanishes at 6000 K. For temperature of 3000 K, the diffusion coefficient of hydrogen is shifted towards higher values compared to the diffusion coefficient of hydrogen in pure methane. The excess hydrogen in the mixture also provides electrostatic repulsion to carbon atoms, increasing the diffusion of carbon atoms in the mixture. At higher temperature, due to thermal dissociation we do not see a huge difference between the diffusion coefficients of the mixture and of pure methane. When compared to the self-diffusion coefficient of the components in pure methane [224] (see Fig. 5.2), at high densities, the diffusion coefficients are almost constant.
The structural arrangement of the fluid is better understood with the aid of the pair distribution function. For low temperatures and density, the system behaves molecular with sharp peaks observed at 0.74 Å and 1.09 Å, corresponding to the ambient bond length of molecular hydrogen and methane, respectively [204]. For the hydrogen subsystem, we observe a second peak at 1.76 Å, due to the hydrogen atoms in methane. The change in the slope of the thermal and caloric EOS due to the dissociation of the molecules is observed, and this effect is more clearly seen in the PDFs. The narrow peak from hydrogen molecules becomes less sharp and eventually flattens out as the temperature rises, indicating the dissociation of the molecules. We observe similar effects for methane for g_{HC}(r), the peak decreases to half of the value that it was at 2000 K. Furthermore, the increment of temperature leads to a new peak of g_{CC} at 1.4 Å [204], forming carbon

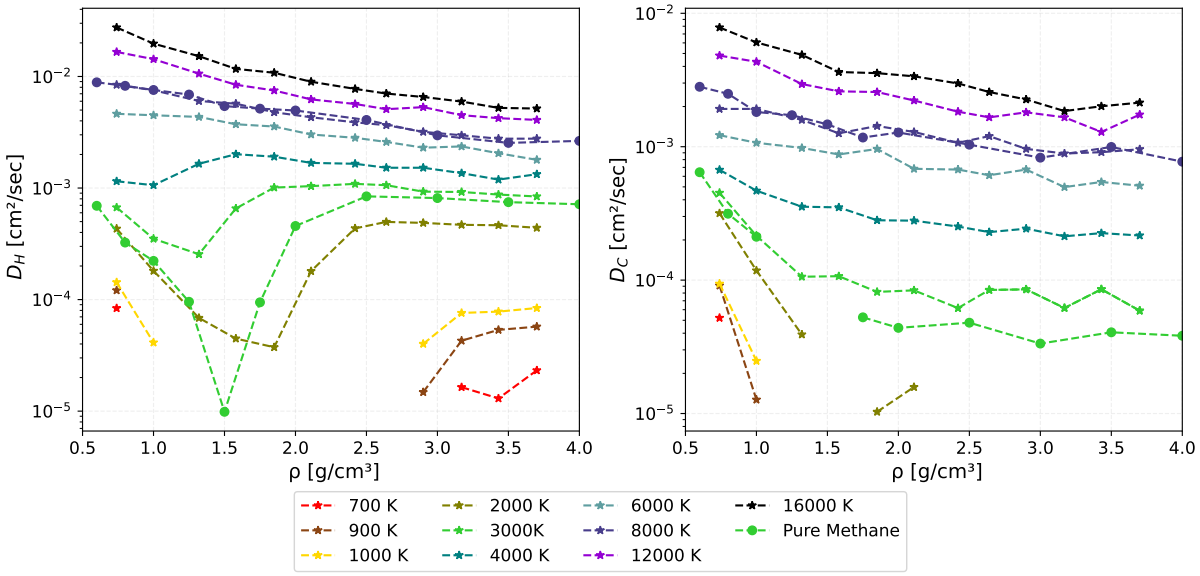


Figure 5.2.: Self diffusion coefficients of hydrogen (left) and carbon (right) in the mixture at temperatures between $700 - 16000$ K. Self diffusion coefficients of carbon and hydrogen in pure methane for 3000 K and 8000 K [224]. For accuracy purposes, any value below 10^{-5} cm^2/sec to be zero or non-diffusive.

chains, consistent with other studies: Spanu et al. [225] observed a distinct feature at 1600 cm^{-1} in the vibrational DOS, attributing to threefold coordinated carbon atoms. Furthermore, an experimental campaign on shock−compressed methane [226] revealed changes in the Hugoniot shock velocity slope predicting a polymeric region, consistent with our [204] and previous findings [224, 227]. Under ambient conditions, C−H bonds are characterized by sp^3−hybridization, similar to the C−C bonds in diamonds with a length of 1.54 Å. With the formation of carbon clusters, we find the minimum distance between C−C to be 1.4 Å, suggesting sp^2−hybridisation. However, this cannot be established with certainty, for which more analysis such as bond angle distribution, Millikan analysis, etc., would be required. Finally, as the temperature is increased, the C−C bonds are of transient [227]/unstable nature, signified by the reduction of peak height and broadening of $g_{CC}(r)$. In Fig. 5.3, we compare the PDFs of pure methane and the mixture at 4000 K and 40 GPa; additional hydrogen molecules lead to dissociation and clustering of carbon atoms forming a polymer at a lower pressure than in pure methane. This process leads to free ionized hydrogen atoms, closing the band gap. The impact of hydrogen on electronic properties is significant, leading us to calculate the band gap and electronic properties using the methods described in Sec. 3.3.2 in the following subsections.

5.2 Modeling the EOS and electronic properties

This section discusses the behavior of the mixture of methane and hydrogen for a hydrogen molecular fractions of $\mathcal{X}_{H_2} = 0.059, 0.116, 0.2008$. We outline the effect on the thermal EOS and electronic properties as a function of hydrogen concentration. We focus on a

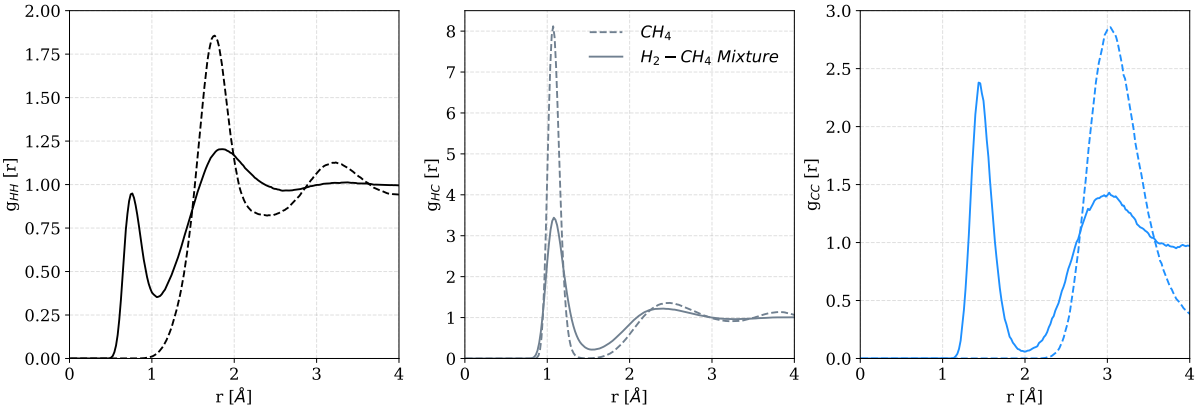


Figure 5.3.: PDFs of the constituents in the methane–hydrogen mixture and pure methane [224] at $T = 4000$ K and $P \approx 40$ GPa

temperature range of $T = 3000 - 6000$ K, especially relevant for the interior conditions of Uranus and Neptune, as it coincides with $20 - 70\%$ of the planets' radii.

5.2.1 Thermal EOS

The thermal EOS is particularly important, as the compositional gradient within the interior of any planet is not constant and can significantly impact the interior. One such phenomenon is the demixing of H−He and He−Ne in the interior of Jupiter and Saturn, resulting in helium/neon droplets which sink deeper into the planets. X-Ray Thomson scattering experiments on polystyrene $(C_8H_8)_n$ [228, 229] shows demixing of C–H with a presence of liquid metallic hydrogen. Hence, knowledge of the thermal EOS of a mixture is required, ideally from the information of pure components. Using the thermal EOS of pure methane and hydrogen, we propose an analytical model to describe the thermal EOS of CH_4−H_2 mixtures, as shown in Eq. (5.1):

$$P_{\text{fit}}(\mathcal{X}, \rho, T) = \sum_i \mathcal{X}_i P_i(\rho, T) + RT\rho \sum_i \mathcal{X}_i \log \mathcal{X}_i + \Delta P. \tag{5.1}$$

The model consists of ideal gas contributions, i.e., linear mixing of the partial pressures, P_i of the pure components and their configuration entropy, each weighted by the molecular fraction. Here, R is the universal gas constant and ΔP is the correction term to represent non-ideal effects of the mixture given in Eq. (5.2):

$$\Delta P(\mathcal{X}, \rho) = \mathcal{X}_{H_2}(1 - \mathcal{X}_{H_2})(A + B\rho^c). \tag{5.2}$$

The excess part of the pressure is modelled using the polynomial expansion technique shown by Redlich and Kister [230], which is used to map excess thermodynamic quantities in binary mixtures. The expansion fails at 50–50 concentration for the thermal EOS, the difference between the linear mixing and real DFT-MD results grows as ρ^c. We

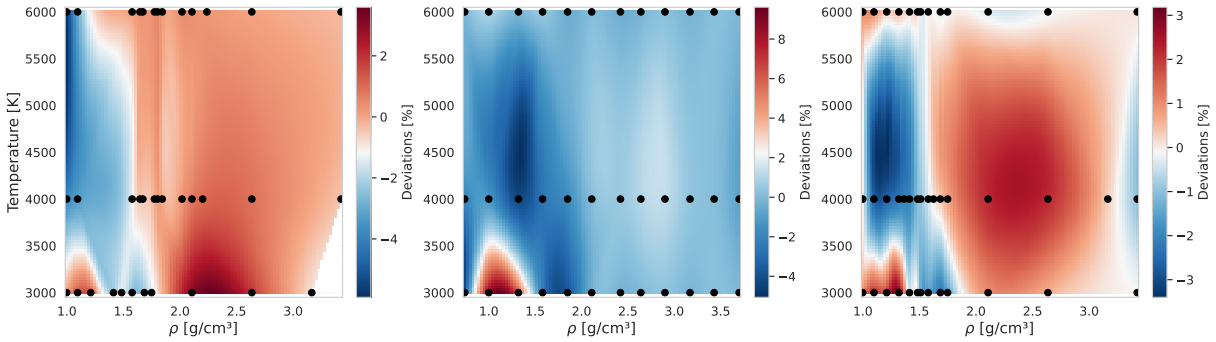


Figure 5.4.: Deviations in pressure from the real CH_4–H_2 mixtures $\mathcal{X}_{H2} = 0.059$ (Left), $\mathcal{X}_{H2} = 0.116$ (Middle), $\mathcal{X}_{H2} = 0.2008$ (Right) and the prediction from our analytical model Eq. (5.1). Black dots denote the DFT–MD points. Between the isotherms and isochores, we cubically interpolated the deviations.

therefore replace the summation with a polynomial fit. In order to ensure injectiveness, the interpolation of P_i is done on the density axis of the respective mixture. The parameters are fitted using the least-square technique. Figure 5.4 presents the calculated deviation of the thermal EOS of the all the considered mixtures from the DFT-MD simulations. For the lowest and the highest concentration of hydrogen molecules in the mixture, i.e., 5.9% and 20.8%, the deviation does not increase beyond 5% throughout the whole $\rho - T$ space. However, for a concentration of 11.6%, the deviation of modelled thermal EOS and the real mixtures is just above 8%. For all mixtures, the maximum deviations are observed at the lowest temperature, where the pressure triggers dissociation.

5.2.2 Transport Properties

To understand the impact of hydrogen molecules, we show the average electronic band gap for a mixture of $\mathcal{X}_{H_2} = 0.116$ in Fig 5.5, presented in Paper I [204]. To calculate the band gap, we use the technique as mentioned in Sec. 3.3.1. The mixture remains in an insulating state with a band gap of more than 3 eV up to 3000 K where the band gap closes, coinciding with the dissociation process as mentioned in the previous section. In comparison, for pure methane the band gap closes at 4000 K and for the methane–water mixture, the gap closes at 5000 K due to formation of stable ions such as OH^- and H_3O^+ [232]. Furthermore, we evaluate the electrical properties of both pure and mixed systems under the framework of LRT, by calculating Onsager coefficients, as mentioned in Sec. 3.3.2. Our work provides, for the first time, the dataset of dc electrical and thermal conductivity for pure methane and methane-hydrogen mixtures, presented in Fig. 5.6. A systematic increase in both electrical and thermal conductivities is observed with increasing pressure, a trend that is well-documented for fluids such as hydrogen and nitrogen. For pure methane the trend is the same. However, it remains substantially less pronounced than that of pure hydrogen, primarily due to the large scattering cross-section of the carbon atoms.

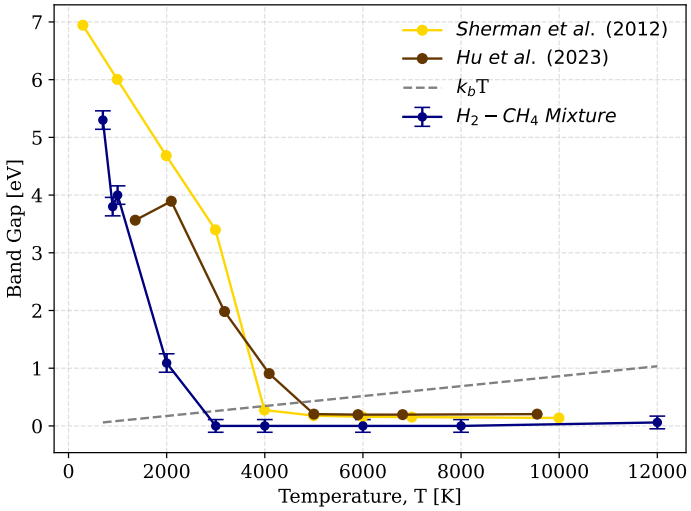


Figure 5.5.: Average electronic band gap of the methane-hydrogen mixture along the 1.58 g/cm^3 isochore as a function of the temperature (blue). The band gaps of pure methane given by Sherman et al. [227] (yellow) and of the methane-water mixture of Hu et al. [231] (brown) are also shown.

For varying molecular fractions of hydrogen, denoted by $\mathcal{X}_{H_2}$, we observe a slight increment in conductivities from pure methane. For $\mathcal{X}_{H_2} = 0.2008$, there is only a 1.5−fold increase in overall electrical conductivity compared to pure methane; however, it is only 0.4 % of pure hydrogen. The increase in electrical conductivity in pure methane and its mixtures can be attributed to the closing of the band gap by free hydrogen, which exhibits a high sensitivity to pressure and temperature effects. The carbon atoms do not play a significant role in this context due to their substantial overlap among p–orbitals, which makes them resilient to increases in pressure and temperature. The thermal conductivity

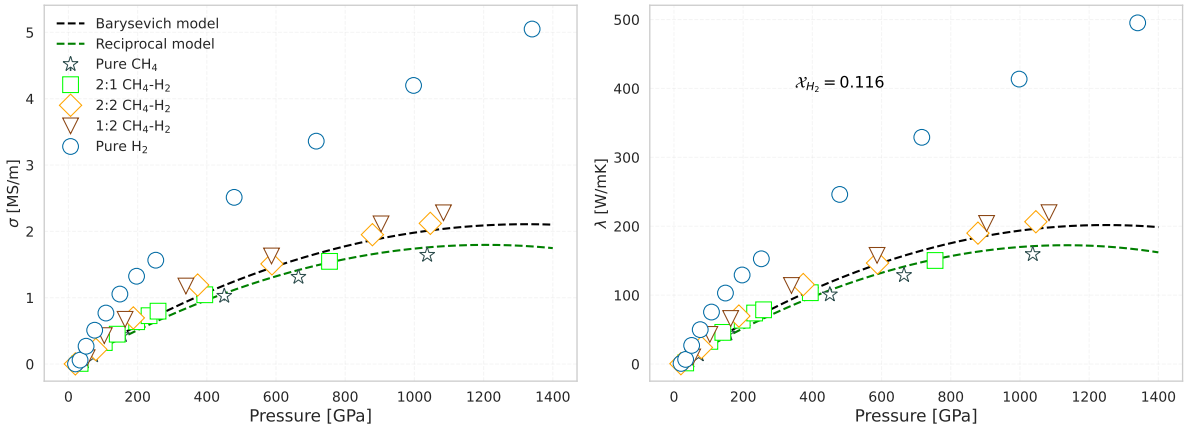


Figure 5.6.: Electrical and thermal conductivity mixing models as function of pressure along an isotherm of 4000 K. Black: (i) Barysevich model [233] (Eq. (5.3)) with $n = -2.8$. Green: (ii) reciprocal mixing (Eq. (5.4)). DFT–MD data are color coded symbols; circles denote pure H_2 and stars denote pure CH_4. Diamonds, triangles, and squares denote various mixed systems.

follows a trend similar to that of the electrical conductivity; the presence of polymers provides thermal insulation, which ultimately makes the heat transfer less efficient. Prior studies conducted by Lorenzen et al. [234] and French et al. [235] suggest a decrease in electrical and thermal conductivity with increased helium concentration. Compared to H−He mixtures, where Lorenzen et al. [10] predict the metallization in H–He mixtures to occur around 100 GPa at 4000 K for a hydrogen concentration of 66%. In the mixture with 5% hydrogen molecules, we find similar metallization pressures at the same temperature.

Similar to the mixing model for the thermal EOS, analytical models describing electrical properties based on the data of pure species are incredibly challenging and very few exist. White et al. [236] put forward an analytical model for CH mixtures, describing low−frequency excitations, however, the model fails to describe the same at high−frequency. Other approximate models can be found in the following Refs. [237–240]. Nonetheless, most of these models or mixing rules are suited for conditions relevant for ICF experiments and not necessarily for planetary conditions where intermolecular interactions are pivotal. Since there is a lack of models for electrical properties in planetary conditions, we employ two numerical models: (i) Proposed by Barysevich et al. [233], Eq. (5.3) was employed to evaluate the electrical conductivity of copper from wire explosions based on the theory of transport for heterogeneous systems, i.e., two–phase regions. (ii) the reciprocal model according to Eq. (5.4):

$$\varphi_{\text{mix}} = \varphi_{H_2} \left(1 + \frac{1 - \mathcal{X}_{H_2}}{\frac{\mathcal{X}_{H_2}}{n} - \frac{\varphi_{H_2}}{\varphi_{H_2} - \varphi_{CH_4}}} \right) , \tag{5.3}$$

$$\frac{1}{\varphi_{\text{mix}}} = \sum_i \frac{\mathcal{X}_i}{\varphi_i} . \tag{5.4}$$

Here, φ denotes the electrical (σ) and thermal conductivity (λ), n in Eq. (5.3) is a parameter to incorporate non–ideal effects. The results of the models are shown in Fig. 5.6. Both models agree well with DFT data, however, the reciprocal model deviates substantially with increasing pressure. The numerical model (i) provides a way to calculate the dc electrical values from the values of pure species, and the inclusion of non–ideal effects makes it more effective for planetary modelling.

Finally, we explore the well-established relationship between electrical and thermal conductivity, specifically the Lorenz number L (see section 3.3.2), as illustrated in Fig. 5.7. At lower temperatures and pressures, molecular bonds are intact, leading to a significant deviation from L_0. Pure hydrogen and methane exhibit no temperature dependency at high pressures, which is typical for metallic systems, and thus satisfy the Wiedemann–Franz law. However, in the case of methane, the deviation from L_0 at lower pressure−temperature conditions is considerably more pronounced than in pure hydrogen (H_2) [222]. For the mixture with the highest molecular hydrogen content ($\mathcal{X}_{H_2} = 0.2008$

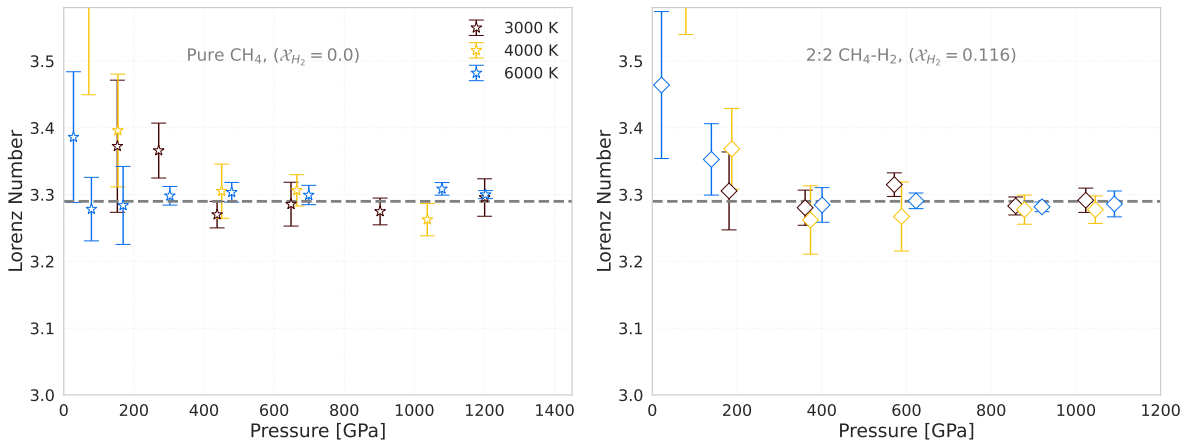


Figure 5.7.: Lorenz number of pure methane and methane-hydrogen mixture ($\mathcal{X}_{H_2}$) as a function of pressure for different temperatures. Symbols $\star$ denote pure methane and $\Diamond$ denotes the methane and hydrogen mixture. Brown, yellow, and blue color symbols denote 3000, 4000, and 6000 K, respectively. The dashed gray line shows the limiting value of $L_0 = \pi^2/3$ known as the Wiedemann-Franz law.

at 3000 K), the observed Lorenz number is significantly lower than L_0, even at high pressures. One possible explanation for this could be the enhancement of electron scattering due to the presence of stable carbon clusters, which results in a reduction in thermal conductivity. At $T = 6000$ K, we find L_0 valid for all mixtures. Similarly, we encounter the same deviation for $\mathcal{X}_{H_2} = 0.059$ and $\mathcal{X}_{H_2} = 0.116$, although not as strong as for the mixture with molecular mass fraction of 0.2008.

5.3 sDFT-MD: Hydrogen as a test case

In this section we outline the results of linear scaling DFT combined with Langevin dynamics, i.e., sDFT−Langevin dynamics on pure hydrogen at 30,000 and 60,000 K. The fundamentals are briefly mentioned in Section 4.1 and Paper III [214] presents the findings. For all the sDFT calculations 40 stochastic orbitals, the LDA XC functional, and norm-conserving pseudopotentials are used and compared with deterministic DFT (dDFT), i.e., VASP, whenever possible. Fig. 5.8 presents the pressure estimate at $\rho = 1.00$ g/cm^3 as a function of system size. Pressure values from sDFT show an increment of up to 5% when the cutoff is increased from 9 to 25 E_h (1 $E_h \approx 27$ eV). Compared to the dDFT results, the sensitivity is slightly higher. This could be due to the difference in the type of pseudopotential used when converging to the infinite energy cutoff limit [214]. However, sDFT agress well with the established converged VASP results.

Finally, we find the computational time of a single cycle of an SCF calculation to scale as $x = N_e \log N_e$. The overall scaling becomes $x^{1.3}$ with the system size. We also note that, due to the use of the Chebyshev expansion and its dependency on inverse temperature (see section 4.2.4), simulations at higher temperature conditions will be faster. This is

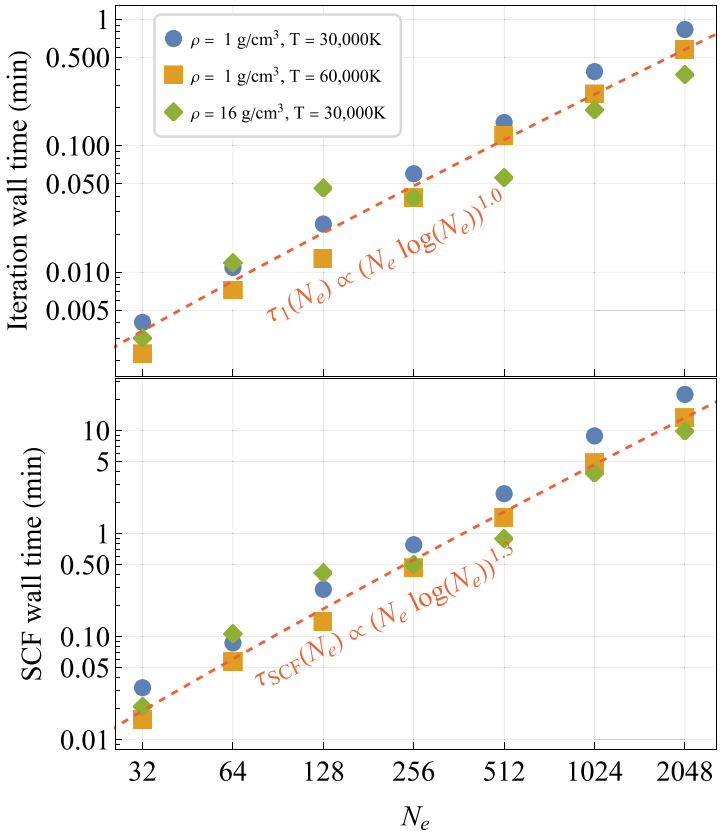


Figure 5.8.: Self−consistent field wall times as a function of the number of electrons N_e for hydrogen at different densities and temperatures: Blue circles: $\rho = 1.00\ \mathrm{g/cm^3}$ and $T = 30,000$ K, orange squares: $\rho = 1.00\ \mathrm{g/cm^3}$ and $T = 60,000$ K and green diamonds: $\rho = 16.00\ \mathrm{g/cm^3}$ and $T = 30,000$ K. Upper panel: a single SCF iteration; lower panel: entire SCF calculation [214].

a very useful development for the field of WDM, as conventional DFT requires more computational resources with increasing temperature.

5.4 Summary and Outlook

In this work, the thermodynamic, structural, and transport properties of the mixture of CH_4-H_2 at high pressures have been investigated using density functional theory molecular dynamics simulations. Reaching up to a pressure of 1 TPa and a temperature of 16000 K, our database covers conditions relevant for ice giant planets of our solar system. It provides accurate data regarding EOS and transport properties. We tested the linear mixing approximation and tested the accuracy and efficiency of sDFT−MD on pure hydrogen.

Initially, we investigated the characteristics of a mixture of methane and hydrogen [204]. We observe the dissociation of hydrogen molecules, which catalyses the decomposition of methane at a lower pressure than in pure methane by introducing disorder into the system. Diffusion coefficients and pair distribution functions were calculated to characterize thermodynamic phases. However, contrary to specific experiments and theoretical investigations [19] nano−diamonds were not observed, which might be due to finite size effects concerning the nucleation rate of diamond. For the first time, we provide electrical properties for CH_4-H_2 mixtures; we observe the band gap to be more sensitive with respect to temperature than in pure methane and methane−water mixtures. Using Mott's minimum conductivity criteria [241, 242], we can predict the occurrence of an insulator-metal transition, which is driven by the dissociation of its constituent particles. Furthermore, as a test case, we calculated the electrical conductivity along the isentrope of Uranus based on a model of Nettelmann et al. [243] and we find the mixture to be metallic around $\approx$ 60% of the planet's radius [204].

Extending on the foundational work, we study the effect of different hydrogen molecular mass fractions ($\mathcal{X}_{H_2} = 0.059, 0.116, 0.2008$) within a smaller range of temperature from 3000 to 6000 K. We propose an analytical model for the thermal EOS of the mixture including non−ideal effects based on the EOS of pure systems. For all mixtures, we obtain a maximum deviation of 8% between the LMA and the real thermal EOS. Similar to the model for the EOS, we also propose a model for electrical and thermal conductivities based on data for pure methane and hydrogen, agreeing very well at high pressure; however, there is a slight disagreement at lower pressure, where the system remains molecular. We also observe the dc values of electronic properties to be substantially lower in the mixture than in pure hydrogen, despite the dominant number of hydrogen atoms [222]. This can have a substantial effect on the modeling of planetary interiors as lower values of thermal conductivity may reduce the convective nature of heat. This situation becomes more complex when other high−pressure phases such as superionic water and/or ammonia are taken into consideration. The nonmetallic nature of some of these phases can enhance phonon scattering, further reducing the thermal conductivity, and this may mediate into the variations in the age and radius of the planet.

Using the sDFT implementation, we investigate hydrogen at 30,000 K. We observe a

linear computational scaling with the number of atoms or wave functions, representing a substantial improvement over the cubic scaling of traditional DFT. The overall scaling is observed to be $x^{1.3}$ where, $x = N_e \log N_e$. Pressure estimates match well with the results from traditional DFT. The sensitivity to the cutoff energy is seen to be reduced as the density is increased [214].

The future pathway to build on this work involves an extensive investigation of electronic and ionic transport properties, including conductivities (electrical and thermal), viscosity, and compressibility of methane−ammonia/water mixtures. This would provide an extensive data set that could be applied to interior structure models and dynamo simulations of the ice giant planets. A similar dataset of H−He mixtures is used very well and relatively frequently to model the interiors of Jupiter, Saturn, and their respective dynamos. Additionally, we note that the nature of heat conduction in ice giants is relatively unknown; hence, we see knowledge of viscosity becoming of paramount importance. For example, a wide range of EOS and electronic properties for methane-hydrogen mixtures at various concentrations can enhance our understanding of the mass-radius relationship and dynamo process in methane-rich planets, such as Kepler−89c, GJ 3470b, Kepler−20c, etc. [244]. Another pathway is to investigate WDM properties of mixtures of methane/water/ammonia and rocks such as olivine (Mg_2SiO_4), enstatite ($MgSiO_3$), etc., to better understand the properties of Super−Earths such as Kepler−22b [245], TOI−1846 b [246], and Kepler−452b [247]. The demixing of hydrocarbons (polystyrene, polyethyelene) into diamonds is also a hot topic. Similar to the demixing of H−He [67] and H_2−H_2O [70, 248], the onset of demixing between carbon and other constituents is triggered by the metallization of hydrogen. We plan to apply coupling constant integration [249–252] to calculate entropies which are very important when dealing with demixing. This not only aims to improve theoretical understanding of the phenomena but to also aid experimental campaigns. Finally, we note that the computational complexity of DFT−MD restricts usability for the conditions in the interior of white and brown dwarfs and fusion conditions, where temperatures reach up to millions of Kelvin. We find that sDFT−MD provides a gateway and alleviates the complexity by linearizing the calculations, allowing us to study the state of matter in the aforementioned conditions.

The wide range of datasets and new techniques for conditions in celestial bodies, provided in this thesis, serve to improve and conceptualize more sophisticated models for planets, as well as white and brown dwarfs, leading to a better understanding of the evolution of our Solar System and, in turn, our Universe.

6. Publications

This chapter contains two first author publications [204, 222] and one second author publication [214]. The titles, authors and their contributions are given prior to every publication.

6.1 Mixture of hydrogen and methane under planetary interior conditions

- **A. J. Roy:** Preparation of the manuscript, conducting DFT-MD simulation, data analysis and interpretation of the results.
- **A. Bergermann:** Preparation of the manuscript, interpretation of the results.
- **M. Bethkenhagen:** Preparation of the manuscript, interpretation of the results.
- **R. Redmer:** Supervision of the project, preparation of the manuscript, interpretation of the results

PCCP

ROYAL SOCIETY OF CHEMISTRY

PAPER

Check for updates

Cite this: *Phys. Chem. Chem. Phys.*, 2024, **26**, 14374

Mixture of hydrogen and methane under planetary interior conditions†

Argha Jyoti Roy, *[a] Armin Bergermann, [a] Mandy Bethkenhagen [b] and Ronald Redmer [a]

Received 5th January 2024,
Accepted 24th April 2024

DOI: 10.1039/d4cp00058g

rsc.li/pccp

We employ first-principles molecular dynamics simulations to provide equation-of-state data, pair distribution functions (PDFs), diffusion coefficients, and band gaps of a mixture of hydrogen and methane under planetary interior conditions as relevant for Uranus, Neptune, and similar icy exoplanets. We test the linear mixing approximation, which is fulfilled within a few percent for the chosen P–T conditions. Evaluation of the PDFs reveals that methane molecules dissociate into carbon clusters and free hydrogen atoms at temperatures greater than 3000 K. At high temperatures, the clusters are found to be short-lived. Furthermore, we calculate the electrical conductivity from which we derive the non-metal-to-metal transition region of the mixture. We also calculate the electrical conductivity along the P–T profile of Uranus [N. Nettelmann *et al.*, *Planet. Space Sci.*, 2013, **77**, 143–151] and observe the transition of the mixture from a molecular to an atomic fluid as a function of the radius of the planet. The density and temperature ranges chosen in our study can be achieved using dynamic shock compression experiments and seek to aid such future experiments. Our work also provides a relevant data set for a better understanding of the interior, evolution, luminosity, and magnetic field of the ice giants in our solar system and beyond.

1 Introduction

Hydrogen and carbon, the most and fourth most abundant elements in the universe,[1] are fundamental building blocks of organic compounds and, thus, the very essence of life that we know today, encompassing an astounding array of molecules that have captivated the attention of scientists across various disciplines. From astrophysics to astrobiology and materials science to quantum physics, researchers have focused on these elemental mixtures, seeking a deeper understanding of our observable universe.

Hydrogen, the first element in the periodic table, exhibits a rich tapestry of physical phenomena such as a first-order liquid–liquid phase transition, a pressure-induced atomic solid, and quantum rotational phases, see ref. 2–9 Additionally, under high temperature and pressure conditions, hydrogen not only reacts with other materials but also can produce van der Waals compounds.[10–13]

Methane (CH_4), a molecule consisting of an sp^3-hybridized carbon atom surrounded by four hydrogen atoms, is very important for planetary physics as it is one of the major constituents of ice-giant planets like Uranus and Neptune.[14,15] Hydrocarbons are, *e.g.*, the reason for the distinct bluish hue of these planets as they absorb red light and reflect blue light.[16] Space missions like Cassini[17] and New Horizon[18] revealed huge lakes and seas of liquid hydrocarbons and mountains covered with frozen methane on Titan and Pluto, respectively.

Therefore, many studies investigated the behavior of hydrocarbons under pressure and temperature conditions relevant to planetary interiors. Interestingly, early gas gun-driven shock wave experiments on methane found evidence of diamond formation under pressure and temperature conditions as relevant for the interior of Uranus and Neptune.[19–21] Since then, numerous high-pressure experiments using diamond anvil cells (DACs) have investigated the formation of diamond from compressed methane and hydrocarbons.[21–26] Note that more complex mixtures containing hydrogen, carbon, nitrogen, and oxygen were also studied.[27–29] In particular, evidence for diamond formation under conditions typical for the deep interior of Uranus has been found in laser-driven shock compression experiments on plastics like polystyrene.[28,30–32]

Molecular dynamics (MD) simulations combined with density functional theory (DFT) were used to calculate the equation of state (EOS) and analyze the dissociation, polymerization into carbon chains, and chemical bonding properties of methane.[33–37] Although there are various EOSs for a pure methane fluid and solid[34,38–40] and for the mixture of methane with other compounds,[41,42] such as water and ammonia, the mixture of CH_4

[a] *Institut für Physik, Universität Rostock, D-18051 Rostock, Germany*
[b] *LULI, CNRS, CEA, Sorbonne Université, École Polytechnique - Institut Polytechnique de Paris, 91128 Palaiseau, France.*
E-mail: argha.roy@uni-rostock.de

† Electronic supplementary information (ESI) available. See DOI: https://doi.org/10.1039/d4cp00058g

This journal is © the Owner Societies 2024

and H_2 under these conditions remains an area of ongoing research. For instance, the stability of methane–hydrogen solid compounds exceeding 160 GPa was studied by[43] using XRD, DAC, and DFT techniques, which resulted in different structures depending on the concentration of hydrogen. However, in the liquid region, the database is extremely sparse.

The *P*–*T* conditions under study are relevant not only for the interior of ice-giant planets such as Uranus and Neptune but also for industrial purposes[44–50] and inertial confinement fusion (ICF).[51,52] Accordingly, further investigation of the EOS of methane and hydrocarbons and subsequent analysis of their behavior under high *P*–*T* conditions are important for modeling the interior, evolution, and magnetic field of ice-giant planets.[14,53–56]

Given these important applications, we have assessed the behavior of hydrocarbons and performed extensive DFT-MD simulations to determine the EOS. We analyze the EOS data and assess the question of whether the linear mixing approximation (LMA), often used to model giant planets,[57,58] is applicable to hydrogen and methane or not and found it valid within 4%. We further analyze our hydrocarbon simulations by calculating the pair distribution function (PDF), coordination number and self-diffusion coefficient using the velocity autocorrelation function. This analysis supports the formation of hydrocarbon polymers after dissociation of the methane molecules. Finally, we provide the electrical conductivity calculated using the Kubo–Greenwood formula[59,60] and the band gap of mixtures of hydrogen and methane over a wide range of different densities and pressures relevant to the interiors of giant planets.

Our paper is organized as follows: Section 2 summarizes the details of the DFT-MD simulations. Sections 3.1 and 3.2 provide EOS data and check the validity of the LMA. Structural changes are discussed in Section 3.3 using the self-diffusion coefficient, PDF and coordination number. Section 3.4 discusses the band gaps and our schema for calculating the electrical conductivity. Finally, a summary of our work is presented in Section 4.

2 Computational methods

We use the Vienna *ab initio* simulation package (VASP)[61–65] for the DFT-MD simulations and derive the relevant data for the mixture of CH_4 and H_2. Use of the Born–Oppenheimer approximation allows us to ignore any kind of coupling between the movement of electrons and of the nuclei. The nuclei then undergo classical motion in an effective potential generated by their mutual Coulomb interaction and the interaction with the electronic charge distribution calculated with the Hellman–Feynman theorem. This procedure involves a combination of DFT and classical MD at finite temperatures.[66–69] The electronic interactions are evaluated using DFT. We use classical MD simulations and the Verlet algorithm to propagate the nuclei in time. Projector augmented wave (PAW) potentials,[70,71] implemented in VASP as PAW PBE H h 06Feb2004 and PAW PBE C h 06Feb2004, and the Perdew–Burke–Ernzerhof (PBE)[72] exchange–correlation functional were used. The temperature of the ions is controlled by the Nosé–Hoover thermostat with a Nosé-mass of 10 fs.[73,74] Similar simulation approaches had been applied very successfully to warm dense matter, see ref. 34, 41 and 75.

We used a cubic periodic simulation box containing 54 CH_4 and 54 H_2 molecules and a plane-wave energy cutoff of 1100 eV to calculate the EOS for hydrogen and methane mixtures. The EOS for pure hydrogen is calculated using 256 atoms and a plane-wave cutoff energy of 1200 eV. The Brillouin zone is evaluated using the Baldereschi mean value point (BMVP).[76] This simulation parameter led to results that converged better than 1% in pressure and 0.05 kJ g^{-1} in specific internal energy. All MD simulations were run for at least 8–12 ps using a time step of 0.25 fs. Neglecting the first 4000 time steps of our simulation allowed us to calculate the thermodynamic averages of the equilibrated system. For pure methane, we used the EOS provided by Bethkenhagen *et al.*[41]

3 Results

3.1 Equation of state

The EOS data are obtained from thermodynamic properties such as pressure *P*, energy *U*, and temperature *T* by averaging over the entire simulation time after equilibration. We have studied a density–temperature grid bounded by 0.74 g $cm^{-3} \leq \rho \leq$ 3.70 g cm^{-3} and 700 K $\leq T \leq$ 16 000 K. It is important to note that as carbon atoms can undergo various hybridization states, the simulations have to start with the same configuration in order to avoid bias towards certain structures.

Fig. 1 shows the EOS along various isochores. A very smooth behavior is observed for both the thermal (top) and caloric EOSs (bottom). The pressure increases systematically with increasing temperature. A small plateau at T = 3000 K for ρ = 1.32 g cm^{-3} at about 83 GPa indicates the onset of dissociation of methane molecules; the pressure rises again with temperature afterwards. As density increases we observe a more pronounced drop in pressure. This behavior indicates the onset of a phase transition from a molecular to a polymeric fluid consistent with previous works.[34,77] This feature has a resemblance to the behavior of pure molecular hydrogen. DFT-MD simulations for dense fluid hydrogen show that dissociation of molecules can lead to a region with $(\partial P/\partial T)_V < 0$ as hydrogen atoms can be packed more efficiently than molecules at high densities.[7,78,79] It is essential to note that hydrogen molecules undergo a dissociation process at a lower pressure than methane, which leads the hydrogen atoms to contribute to the process of methane dissociation.

3.2 Testing the linear mixing approximation

Models for giant planets employ EOS data for different materials and mix them linearly at constant pressure and temperature based on the work of DeMarcus and Peebles.[57,58] The LMA allows the density to be extracted,(eqn 1)

$$\frac{1}{\rho_{\mathrm{LM}}(p,T)} = \sum_{j=1}^{N} \frac{\xi_j}{\rho_j(p,T)}, \tag{1}$$

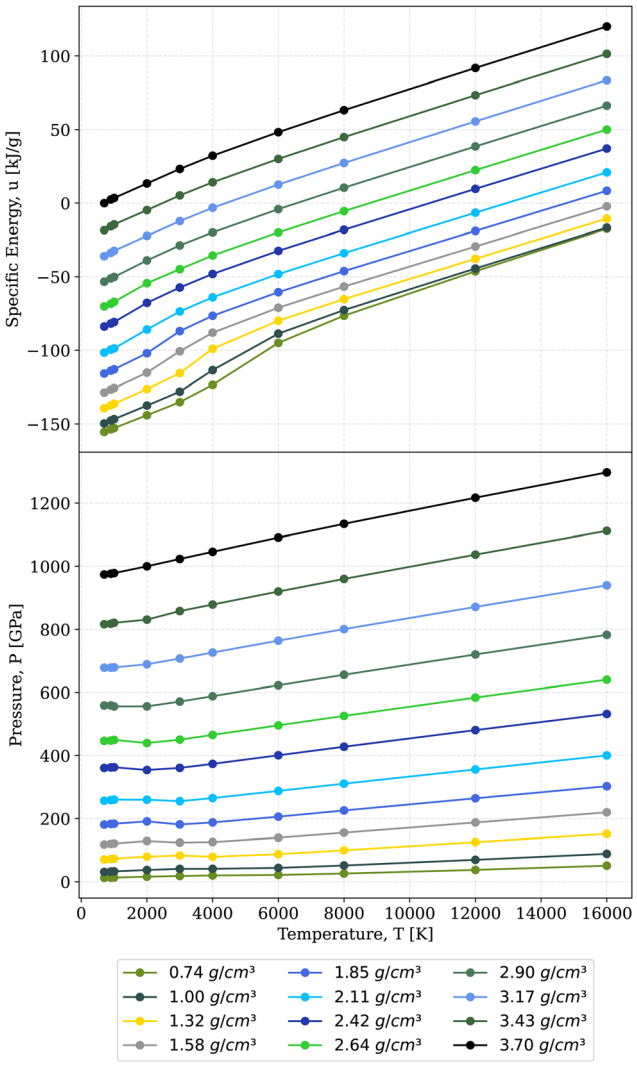


Fig. 1 Caloric (top) and thermal (bottom) EOSs of the mixture of H_2 and CH_4 along the isochores.

and the specific internal energy,

$$u_{\mathrm{LM}}(p,T) = \sum_{j=1}^{N} \xi_j u_j(p,T), \tag{2}$$

where ρ_j, u_j, and ξ_j are the density, specific internal energy, and mass fraction, respectively, of individual components j of the mixture composed of N components. The validity of the LMA has been tested using Monte Carlo simulations[80,81] and later extended to DFT studies.[82,83]

Although several mixing rules exist in the case of the H–He mixtures, the additive volume rule at constant pressure and temperature performed the best.[84] The LMA was tested for the dilute limit of ternary mixtures of H–He for gas giants[85] with high Z elements such as C, N, O, Si, and Fe, as well as for C_2H_3 as a mixture of carbon and hydrogen.[86] The icy mixtures have been studied before with DFT-MD, *e.g.*, for binary and ternary mixtures of CH_4–H_2O–NH_3.[41]

We define the deviations in density and specific internal energy between the linear (LM) and real mixtures as,

$$\Delta\rho(P,T) = \rho_{\mathrm{LM}}(P,T)/\rho_{\mathrm{real}}(P,T) - 1 \tag{3}$$

and

$$\Delta u(P,T) = u_{\mathrm{LM}}(P,T) - u_{\mathrm{real}}(P,T) \tag{4}$$

The EOS obtained for pure hydrogen, pure methane and the mixture was interpolated onto a P–T grid, to interpolate the pressure values along the isotherm we used Akima splines, and temperatures were interpolated linearly. The deviation in energy varies between -4 kJ g^{-1} and 3 kJ g^{-1} and 4% for the density (see Fig. 2). The region of large deviations signals the presence of different phases. For instance, in the case of binary mixtures of CH_4 with H_2O and NH_3 as studied by Bethkenhagen *et al.*,[41] the maximum deviation in energy was observed to lie between -4 kJ g^{-1} and 2 kJ g^{-1}, which was due to the formation of superionic phases in water and ammonia,[87–89] where the energy was released by forming these lattices. In our case, it is mostly atomic hydrogen and polymeric chains of carbon that

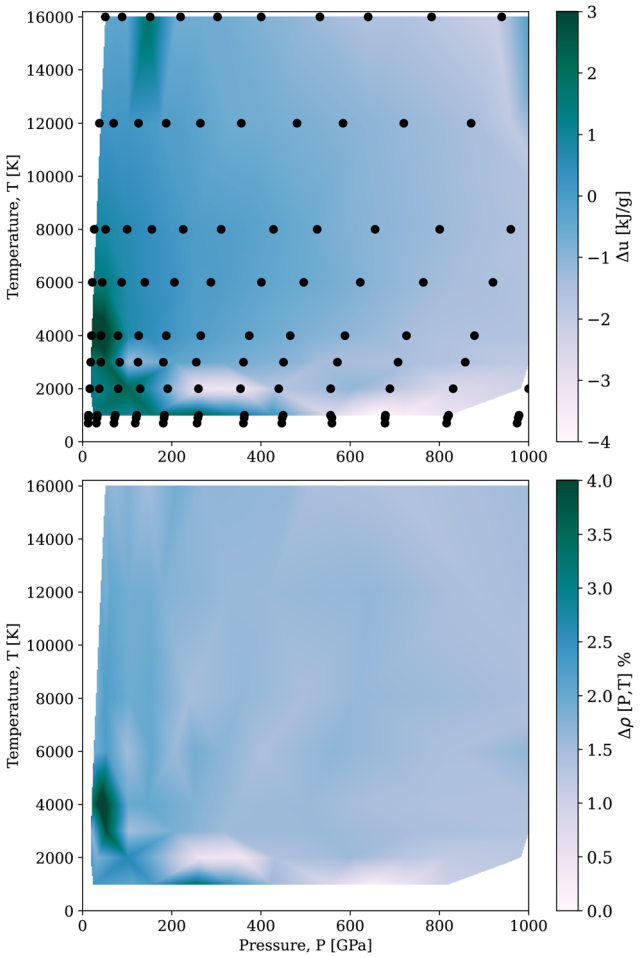


Fig. 2 Deviations of internal energy (top) and densities (bottom) of the real 1 : 1 hydrogen and water mixture from the LMA. Black dots denote the underlying data for the real binary mixture of methane and hydrogen.

This journal is © the Owner Societies 2024

lead to such deviations as the bonds formed by the carbon atom release energy.

It should be noted that our density deviation always remains positive, $V_{REAL} > V_{LMA}$. This suggests that the constituents occupy a larger phase space as long as the system remains fluid throughout the entire P–T space studied here. Although carbon polymerizes into long chains, free hydrogen atoms occupy the phase space. In the study of Bethkenhagen *et al.*,[41] some regions in P–T space were observed where the atoms are more closely packed occupying less volume due to the formation of superionic lattices of nitrogen and oxygen.

3.3 Structural analysis

We have determined self-diffusion coefficients shown in Fig. 3 and PDFs displayed in Fig. 4. The self-diffusion coefficients were calculated *via* the velocity autocorrelation function,

$$D_\alpha = \lim_{t\to\infty} \frac{1}{3N_\alpha} \int_0^t \sum_{i=1}^{N_\alpha} \mathrm{d}\tau \langle v_i(0) \cdot v_i(\tau) \rangle, \qquad (5)$$

where α is the species, $v_i(\tau)$ is the velocity autocorrelation function, and N_α is the particle number.

Diffusion coefficients of both species show a strong dependence on temperature and density, rising with increasing temperature. Interesting features, however, pop up with increasing density. The diffusion coefficients of hydrogen exhibit minima at 2000 K and 1.85 g cm^{-3}, indicating the transition from a molecular to an atomic fluid. At a temperature of 3000 K the diffusion coefficient of hydrogen is shifted towards higher values compared to the diffusion coefficient of hydrogen in pure methane. This shift is attributed to the excess hydrogen and dissociation of methane giving rise to more hydrogen atoms in the box. The excess hydrogen also provides electrostatic repulsion to carbon atoms, making them more mobile and leading to a slightly higher carbon diffusion coefficient in the mixture. At higher temperature, due to thermal dissociation we do not see a huge difference between the diffusion coefficients of the mixture and of pure methane. The minima of the hydrogen diffusion coefficient shift to lower densities with increasing temperatures. This feature finally vanishes at 6000 K. The diffusion coefficients of carbon and hydrogen are almost constant at higher densities, as already obtained by Bethkenhagen *et al.*[87] for ammonia. Due to the formation of polymeric chains of carbon, it is difficult to calculate the diffusion coefficients with sufficient numerical accuracy. Especially, at high density and low temperatures for carbon, the thermal energy provided is not sufficient for the clusters to exhibit translational degrees of freedom. Therefore, coefficients smaller than 10^{-5} cm^2 s^{-1} are considered to be zero.

To better understand the structural changes of the fluid with respect to temperature and density variations, we calculated PDFs. Exemplarily we show results for the 1.32 g cm^{-3} isochore for the temperature range considered here in Fig. 4. The system exhibits molecular properties at lower temperatures. The narrow peak of $g_{HC}(r)$ occurs at an intermolecular distance of 1.09 Å under ambient conditions and the same for $g_{HH}(r)$ where

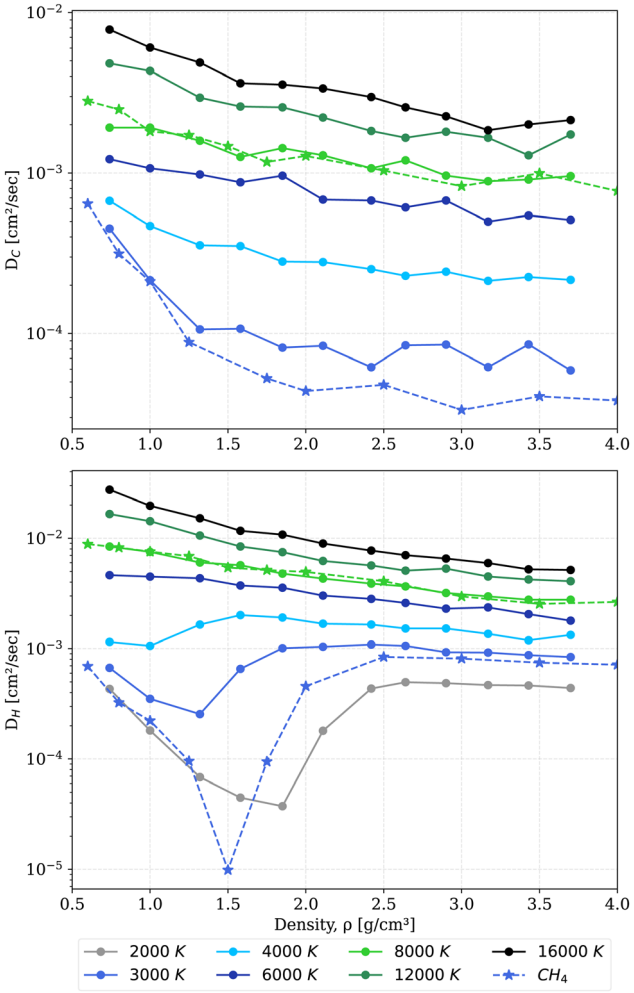


Fig. 3 Diffusion coefficients of carbon (top) and hydrogen (bottom) in the mixture at temperatures between 2000 K and 16 000 K (color coded solid lines). Diffusion coefficients of carbon and hydrogen in pure methane[41] (the star symbol with dotted lines).

the peak occurs at 0.74 Å, followed by a minimum. Note that we see two peaks for the PDF of the hydrogen subsystem. The first maximum is due to the presence of hydrogen molecules and the second is due to hydrogen atoms in methane at 1.76 Å. Increasing temperatures results in a decrease in peak heights of the hydrogen–carbon and hydrogen–hydrogen PDFs. The peak of $g_{HH}(r)$ is flattened as a consequence of the dissociation of hydrogen molecules and hydrogen from methane. For $g_{HC}(r)$ the peak decreases to half of the value that it was at T = 2000 K. Higher temperatures result in a higher peak of $g_{CC}(r)$ and a lower peak of $g_{HC}(r)$ diminishes furthermore and at T = 4000 K a new peak of $g_{CC}(r)$ occurs at 1.4 Å, indicating the appearance of longer carbon chains. This observation was also reported by Spanu *et al.*[35] when a distinct feature at 1600 cm^{-1} in the vibrational density of states appeared, which can be attributed to threefold coordinated carbon atoms. In recent experimental work on shock-compressed methane,[91] the observed changes in the Hugoniot shock velocity–particle velocity slope predict a polymeric region, which is consistent with our and previous

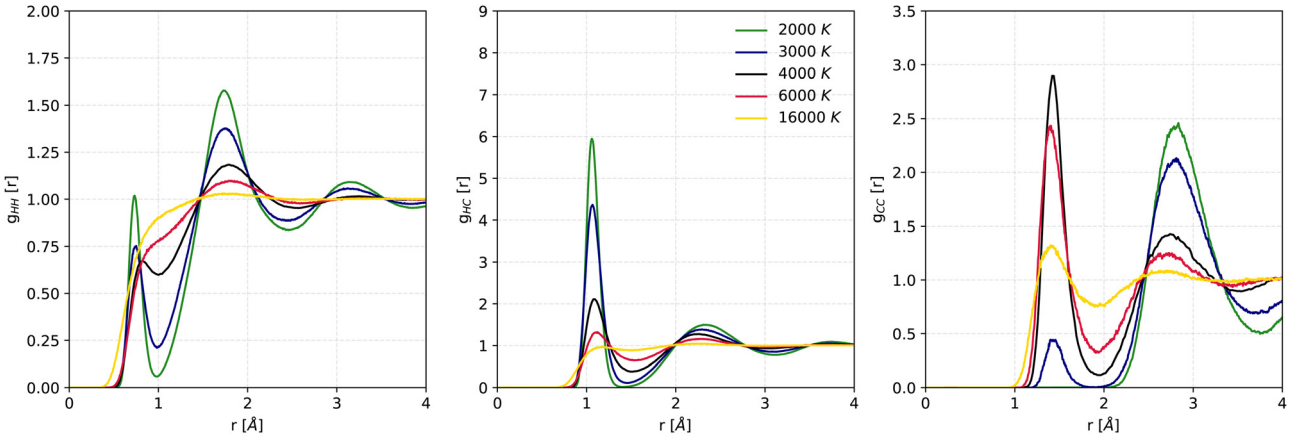


Fig. 4 PDFs of the constituents in the hydrogen–methane 1 : 1 mixture at a constant density of 1.32 g cm^{-3} and temperatures of 2000, 3000, 4000, 6000 and 16 000 K. Left panel: Hydrogen–hydrogen interaction, middle panel: hydrogen–carbon interaction, and right panel: carbon–carbon interaction.

DFT-MD simulations.[34,92] The peak of $g_{CC}(r)$ suggests an sp^2-hybridization between the carbon atoms, whereas in diamond all carbon atoms are single-bonded, *i.e.* sp^3-hybridized with the nearest carbon atom located at 1.54 Å under ambient conditions. Finally, at 16 000 K the peak of $g_{CC}(r)$ is reduced and broadened, indicating the short-lived and unstable nature of the molecules.

The coordination number is calculated to analyse the structural changes in carbon upon compression in more detail and shown in Fig. 5. This number is obtained by integrating the PDF under spherical symmetry consideration to the first minimum.

$$N_c c(r') = 4\pi\rho \int_0^{r'} g_{CC}(r) r^2 \mathrm{d}r. \quad (6)$$

At temperatures of 1000 and 2000 K and densities below 2 g cm^{-3}, the coordination number is greater than 8 due to the molecular nature of the system and many of methane molecules being in the first coordination sphere. Note that the occurrence of the first minima for $g_{CC}(r)$ is found to be at a distance greater than 3 Å. At densities above 2 g cm^{-3}, the dissociation of methane molecules starts and a new peak of $g_{CC}(r)$ arises at 1.4 Å. This leads to a sharp drop in the coordination number. An increase in the coordination number of up to two indicates the gradual transition from the molecular to the polymeric regime. The increase in the coordination number becomes slower at the highest temperatures due to the tendency of shorter carbon chains.

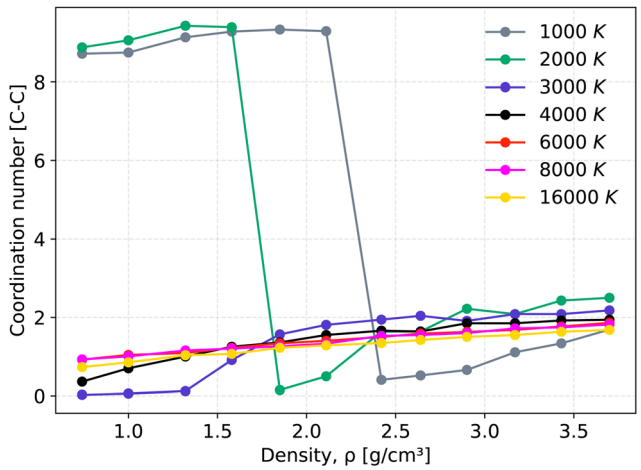


Fig. 5 Coordination number of carbon–carbon as a function of density along the isotherms of 1000, 2000, 3000, 4000, 6000, 8000 and 16 000 K.

In Fig. 6, the PDFs of methane $g_{XY}^{mixture}(r)$ and the hydrogen–methane mixture $g_{XY}^{mixture}(r)$ at a temperature of 4000 K are presented at a comparable pressure. The first peak of $g_{HC}^{mixture}(r)$ is lowered compared to pure hydrogen indicating dissociation. Additionally, a peak arises at $r \approx 1.34$ Å for $g_{HC}^{mixture}(r)$, indicating the presence of carbon chains. This change indicates that the onset of the formation of carbon clusters in the mixture takes place at a lower pressure than that in pure methane.

Despite experiments suggesting diamond formation[22,24,25,93] from various mixtures of C/H, we do not observe such a feature in our calculations. Due to the starting symmetry of our simulation box, it is impossible to distinguish between long carbon chains and the early stage of diamond nucleation, which is also aided by small system sizes.[93] Also, we do not rule out the possibility of observing demixing in our system even though it is not the goal of this work.

3.4 Electronic properties

In Fig. 7, we show the average electronic band gap along the 1.58 g cm^{-3} isochore as a function of the temperatures averaged over the MD trajectory after equilibration and compare with results on pure methane[34] and a mixture of water and methane.[42] To calculate the band gap we use the technique developed by Preising and Redmer.[94] We observe our system to be in an insulating state with a band gap of more than 5 eV. With increasing temperature, the band gap decreases. At 3000 K the dissociation of the constituent leads to a polymeric state in carbon and additional hydrogen atoms so that the band gap closes. Compared to pure methane[34] and methane–water

 This journal is © the Owner Societies 2024

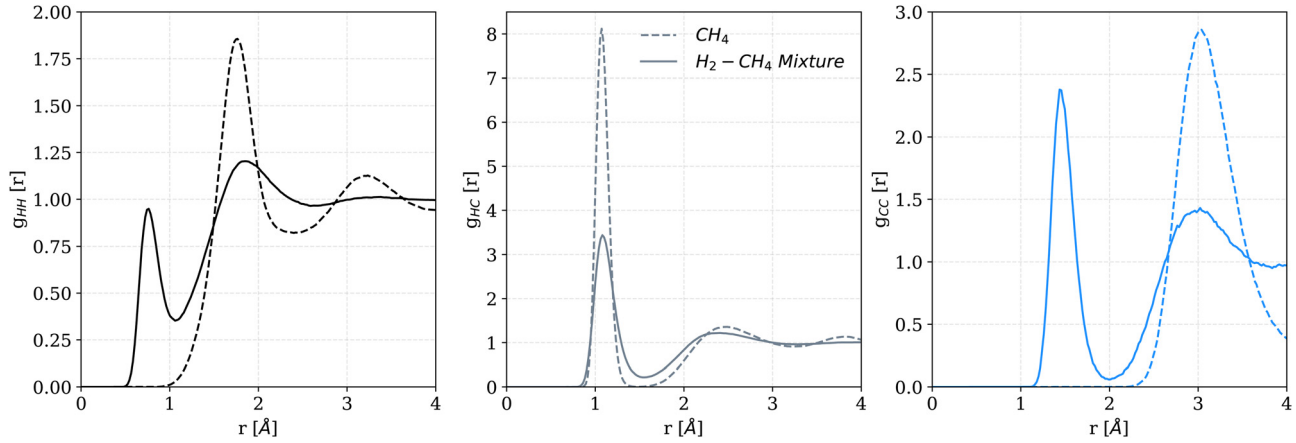


Fig. 6 PDFs of the constituents in the hydrogen–methane 1 : 1 mixture and pure methane[41] (dotted lines) at T = 4000 K and $P \approx$ 40 GPa.

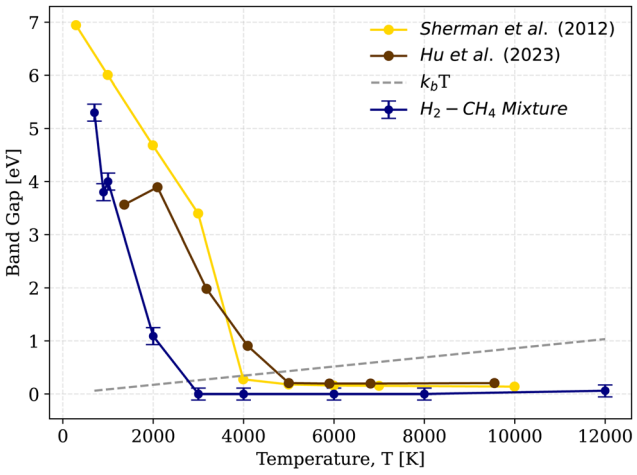


Fig. 7 Average electronic band gap of the hydrogen–methane mixture along the 1.58 g cm^{-3} isochore as a function of the temperature (the blue line with symbols). The band gaps of pure methane given by Sherman *et al.*[34] (yellow) and of the methane–water mixture of Hu *et al.*[42] (brown) are also shown.

mixtures,[42] it is clear that the presence of hydrogen molecules has a great impact on the electronic properties. The insulator-to-metal transition in hydrogen–methane mixtures is driven by disorder that dissociation introduces into the fluid. The mixture becomes metallic at lower temperatures compared with pure methane and methane–water mixtures.

To calculate the dynamic electronic electrical conductivity we used the Kubo–Greenwood formula:[59,60,95–97]

$$\sigma(\omega) = \frac{2\pi e^2\hbar^2}{3m^2\Omega}\sum_{\mathbf{k}} w(\mathbf{k}) \sum_{i,j=1}^{N}\sum_{\alpha=1}^{3}\left[F(\varepsilon_{i,\mathbf{k}}) - F(\varepsilon_{j,\mathbf{k}})\right] \times |\langle\psi_{j,\mathbf{k}}|v|\psi_{i,\mathbf{k}}\rangle|^2 \delta(\varepsilon_{j,\mathbf{k}} - \varepsilon_{i,\mathbf{k}} - \hbar\omega), \quad (7)$$

where m is the mass, ω is the frequency, α is the sum of the average of contribution from the three spatial directions, e is the electronic charge and Ω is the volume of the simulation box. $F(\varepsilon_{i,\mathbf{k}})$ and $\varepsilon_{i,\mathbf{k}}$ are the Fermi distribution functions describing the occupation of the Bloch state $|\psi_{i,\mathbf{k}}\rangle$ having energy $\varepsilon_{i,\mathbf{k}}$ at $\mathbf{k}$ and the dipole matrix elements with the velocity operator $\langle\psi_{j,\mathbf{k}}|v|\psi_{i,\mathbf{k}}\rangle$ are calculated using optical routines of VASP.[61–65] As the simulation box is constrained by periodic boundary conditions, this leads to a discrete spectrum of eigenvalues; hence, the δ function has to be broadened to a finite width for which we use a Gaussian function. Brillouin zone summation is performed using special $\mathbf{k}$-point sets with weighting factors.[75,97–99] Finally, the DC conductivity follows from the static limit:

$$\sigma_0 = \lim_{\omega\to 0}\sigma(\omega). \quad (8)$$

We evaluated the formula (7) for 100 snapshots of equilibrated MD simulations chosen at equivalent time intervals using a Monkhorst–Pack $\mathbf{k}$-point mesh of 2 × 2 × 2 to sample the Brillouin zone. Fig. 8 shows the calculated DC conductivities along the isotherms. At low temperature and pressure, the conductivity is very small and the system exhibits an insulating behavior. At 1000, 3000, and 4000 K the molecular-to-atomic transition can be seen as a sharp increase in the electrical conductivity. For isotherms at lower temperatures, the transition occurs at higher pressures. At 3000 K and a pressure of 181 GPa the value of the DC conductivity is 0.44 MS m^{-1}. Using a two-stage light-gas gun Nellis *et al.*[21] determined the electrical conductivity of shock compressed methane at pressures between 20 and 60 GPa and temperatures in the range of 2000 to 4000 K, finding that conduction is predominantly caused by hydrogen from methane. Similarly, quantum molecular dynamic simulations performed by Li *et al.*[77] on shocked methane predicted that the conductivity is negligible up to 40 GPa, but at pressures above 55 GPa, the DC conductivity increased up to values of more than 0.1 MS m^{-1}, see Fig. 8. A similar behavior can be seen in our results, and the rise of the conductivity is attributed to the dissociation of methane and of hydrogen molecules as well. The dissociated constituents can only contribute to the magnetic field in the form of metallic hydrogen, and the radio waves are generated due to the trapping of such charged particles in the magnetic fields as the

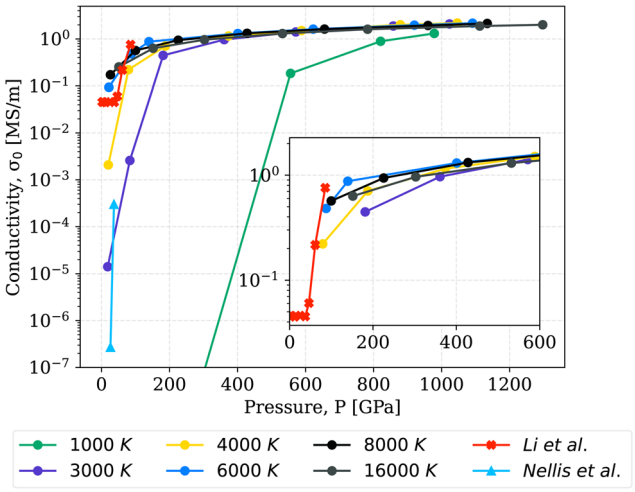


Fig. 8 DC electrical conductivity of a dense hydrogen–methane 1 : 1 mixture as a function of pressure along five isotherms (color coded). For comparison, the theoretical results of Li *et al.*[77] (red crosses) and the experimental data of Nellis *et al.*[21] (blue triangle up) for pure methane are also shown.

Voyager II flyby mission detected radio emissions from Uranus and Neptune.[90,100]

It should be noted that the conductivity does not rise forever. With increasing pressure and temperature, the scattering rate of electrons on ions increases as a result of the broadening of the Fermi function, and their mobility is reduced, a typical characteristic of metals. The effect of both processes almost cancels out and, therefore, the conductivity does not rise significantly at high pressure and temperature, see Fig. 8. A physical explanation was given by Mott[102] and Ioffe *et al.*,[103] which states that any disordered system will remain metallic if the characteristic mean free path of charge carriers is greater than the average distance between the constituent ions. Based on these arguments, the minimum metallic conductivity was estimated to be 2000 Ω^{-1} cm^{-1} and 0.2 MS m^{-1} in fluid hydrogen and expanded metallic fluids such as rubidium, cesium, and mercury. This criterion can also be applied to locate the metallization transition of nonmetallic chemical elements like oxygen and nitrogen when exposed to high temperatures and pressures.[77,104,105] By obtaining conductivity values beyond this minimum metallic conductivity for our system (see Fig. 8), we conclude that a nonmetal-to-metal transition occurred in our mixture of methane and hydrogen.

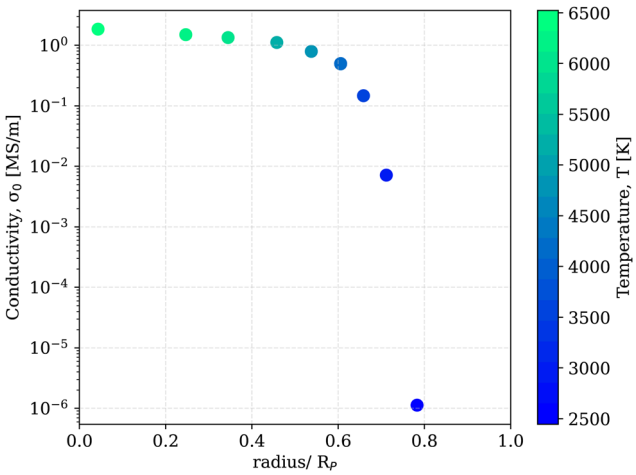


Fig. 9 DC electrical conductivity of a dense hydrogen–methane 1 : 1 mixture along the pressure and temperature profile of Uranus.[101]

Finally, in Fig. 9, we calculate the electrical conductivity along the *P*–*T* profile of Uranus as proposed by Nettelmann *et al.*[101] This model consists of a rocky core surrounded by two envelopes of hydrogen, helium and water with a constant mass ratio of 0.275 : 0.725 in the envelopes. The model predicts a density jump at ∼75% of the planet's radius.[101] From our calculations we observe a metallic behaviour of the mixture at ∼60% of the planet's radius corresponding to a temperature of $T \approx 4176$ K and a pressure of $P \approx 126$ GPa, and a subsequent conductivity of $\sigma \approx 0.49$ MS m^{-1}. Note that the PBE functional underestimates the band gap. Therefore, the metallisation pressures might be slightly low.

The complete data set for DC electrical conductivities is provided in the ESI.†

4 Conclusion

We have calculated the EOS, structural properties, band gaps, and electrical conductivities of methane–hydrogen mixtures at temperatures between 700 K and 16 000 K and pressures between 12 GPa and 1300 GPa. We found that the dissociation of hydrogen molecules increases the disorder and aids in the process of decomposition of methane into carbon clusters and hydrogen atoms. As an example, we choose an isochore of 1.32 g cm^{-3} to demonstrate the evolution of the PDFs of the mixture from a molecular to an atomic phase as a function of temperature. However, contrary to experiments and theoretical prediction of Cheng *et al.*,[93] our simulations yield no nano-diamonds, which might be due to the symmetry of the simulation box, an insufficient number of carbon atoms to form diamond, or finite size effects with respect to the kinetics of diamond nucleation. Our work does not rule out the possibility of observing demixing and future work will be dedicated to this problem. Calculations of the band gap of the mixture show that it closes at lower temperatures than for pure methane. The metallic nature of the fluid is demonstrated by calculating the electrical conductivity and interpreted by using the physical assertions of Mott[102] and Ioffe *et al.*[103] As an example we calculate the electrical conductivity along the *P*–*T* profile of Uranus[101] and observe that the mixture turns metallic at ∼60% of the planet's radius. Testing the LMA yields a limit of 4% deviation in density and of 4 kJ g^{-1} in specific energy for all *P*–*T* conditions considered. Accordingly, we find the LMA to be appropriate for applications such as planetary modeling. Interior models of Uranus and Neptune assume that the planet is made up of several layers: a rocky core in the center, an "icy" middle layer rich in water, ammonia, and methane, and an outer gaseous envelope rich in H_2 and He,[15,56,101,106] albeit more rock-dominated structures are also possible.[14,107]

This journal is © the Owner Societies 2024

The fact that the observed internal heat production of Neptune was twice the energy received from the Sun can be explained *via* gravitational sinking of crystalline, complex or amorphous carbon clusters precipitating towards the planetary center. Also, the lighter hydrocarbons such as ethane and propane formed due to the dissociation inside the planets cannot sink into the planetary core but levitate to the atmosphere by the convection process. This would explain the large amounts of hydrogen molecules in the atmosphere of both planets and for Neptune, the huge abundance of ethane in its atmosphere.[90,108] Although insight into the pure systems is of fundamental interest, planets are composed of a mixture of materials and their combined behavior determines the interior structure as well as the cooling and magnetic field generation. Crucial physical quantities for characterizing the internal structure and evolution of planets include the EOS and fundamental transport properties such as conductivity and diffusivity of the planetary materials.

Information on the EOS and on possible phase transitions of planetary materials helps to advance models for such planets. Furthermore, our findings will facilitate new experiments on the behavior of matter under extreme conditions, in particular at free-electron-laser facilities like LCLS, SACLA, and European XFEL.[26,28,30,32]

Conflicts of interest

There are no conflicts to declare.

Acknowledgements

We thank Martin Preising, Uwe Kleinschmidt, and Martin French for their helpful discussions and technical support. We also thank Roi Baer and Rebecca E. Hadad of the Hebrew University of Jerusalem for their useful notes. This work was supported by the ITMZ of the University of Rostock and the German Israel Foundation for Scientific Research and Development (GIF) within the Research Grant No. I-1486-303.7/2019. Armin Bergermann thanks the Evangelische Studienwerk e.V. for support.

References

1 H. E. Suess and H. C. Urey, *Rev. Mod. Phys.*, 1956, **28**, 53–74.
2 H.-K. Mao and R. J. Hemley, *Rev. Mod. Phys.*, 1994, **66**, 671–692.
3 R. T. Howie, C. L. Guillaume, T. Scheler, A. F. Goncharov and E. Gregoryanz, *Phys. Rev. Lett.*, 2012, **108**, 125501.
4 R. T. Howie, P. Dalladay-Simpson and E. Gregoryanz, *Nat. Mater.*, 2015, **14**, 495–499.
5 E. Gregoryanz, C. Ji, P. Dalladay-Simpson, B. Li, R. T. Howie and H.-K. Mao, *Matter Radiat. Extremes*, 2020, **5**, 038101.
6 P. Loubeyre, F. Occelli and P. Dumas, *Nature*, 2020, **577**, 631–635.
7 W. Lorenzen, B. Holst and R. Redmer, *Phys. Rev. B: Condens. Matter Mater. Phys.*, 2010, **82**, 195107.
8 J. M. McMahon, M. A. Morales, C. Pierleoni and D. M. Ceperley, *Rev. Mod. Phys.*, 2012, **84**, 1607–1653.
9 R. Helled, G. Mazzola and R. Redmer, *Nat. Rev. Phys.*, 2020, **2**, 562–574.
10 P. Loubeyre, R. Letoullec and J.-P. Pinceaux, *Phys. Rev. Lett.*, 1994, **72**, 1360–1363.
11 T. A. Strobel, P. Ganesh, M. Somayazulu, P. R. C. Kent and R. J. Hemley, *Phys. Rev. Lett.*, 2011, **107**, 255503.
12 R. Turnbull, M.-E. Donnelly, M. Wang, M. Peña Alvarez, C. Ji, P. Dalladay-Simpson, H.-K. Mao, E. Gregoryanz and R. T. Howie, *Phys. Rev. Lett.*, 2018, **121**, 195702.
13 D. K. Spaulding, G. Weck, P. Loubeyre, F. Datchi, P. Dumas and M. Hanfland, *Nat. Commun.*, 2014, **5**, 5739.
14 R. Helled, N. Nettelmann and T. Guillot, *Space Sci. Rev.*, 2020, **216**, 1–26.
15 J. J. Fortney and N. Nettelmann, *Space Sci. Rev.*, 2010, **152**, 423–447.
16 P. G. Irwin, N. A. Teanby, L. N. Fletcher, D. Toledo, G. S. Orton, M. H. Wong, M. T. Roman, S. Pérez-Hoyos, A. James and J. Dobinson, *J. Geophys. Res. Planets*, 2022, **127**, e2022JE007189.
17 M. Mastrogiuseppe, V. Poggiali, A. Hayes, J. Lunine, R. Seu, G. Mitri and R. Lorenz, *Nat. Astron.*, 2019, **3**, 535–542.
18 T. Bertrand, F. Forget, B. Schmitt, O. L. White and W. M. Grundy, *Nat. Commun.*, 2020, **11**, 5056.
19 M. Ross, *Nature*, 1981, **292**, 435–436.
20 W. Nellis, F. Ree, M. Van Thiel and A. Mitchell, *Chem. Phys.*, 1981, **75**, 3055–3063.
21 W. Nellis, D. Hamilton and A. Mitchell, *Chem. Phys.*, 2001, **115**, 1015–1019.
22 H. Hirai, K. Konagai, T. Kawamura, Y. Yamamoto and T. Yagi, *Phys. Earth Planet*, 2009, **174**, 242–246.
23 H. Radousky, A. Mitchell and W. Nellis, *J. Chem. Phys.*, 1990, **93**, 8235–8239.
24 L. R. Benedetti, J. H. Nguyen, W. A. Caldwell, H. Liu, M. Kruger and R. Jeanloz, *Science*, 1999, **286**, 100–102.
25 S. S. Lobanov, P.-N. Chen, X.-J. Chen, C.-S. Zha, K. D. Litasov, H.-K. Mao and A. F. Goncharov, *Nat. Commun.*, 2013, **4**, 2446.
26 M. Frost, R. S. McWilliams, E. Bykova, M. Bykov, R. J. Husband, L. M. Andriambariarijaona, S. Khandarkhaeva, B. Massani, K. Appel, C. Baehtz, O. B. Ball, V. Cerantola, S. Chariton, J. Choi, H. Cynn, M. J. Duff, A. Dwivedi, E. Edmund, G. Fiquet, H. Graafsma, N. Jaisle, J. Kim, Z. Konopkova, T. Laurus, Y. Lee, H.-P. Liermann, J. D. McHardy, M. I. McMahon, G. Morard, M. Nakatsutsumi, L. A. Nguyen, S. Ninet, V. B. Prakapenka, C. Prescher, R. Redmer, S. Stern, C. Strohm, J. Sztuk-Dambietz, M. Turcato, Z. Wu, S. H. Glenzer and A. F. Goncharov, *Nat. Astron.*, 2024, **8**, 174–181.
27 M. C. Marshall, M. G. Gorman, D. N. Polsin, J. H. Eggert, M. K. Ginnane, J. R. Rygg, G. W. Collins and L. D. Leininger, *J. Appl. Phys.*, 2022, **131**, 085904.
28 Z. He, M. Rödel, J. Lütgert, A. Bergermann, M. Bethkenhagen, D. Chekrygina, T. E. Cowan,

A. Descamps, M. French and E. Galtier, *et al.*, *Sci. Adv.*, 2022, **8**, eabo0617.
29 A. S. Naumova, S. V. Lepeshkin, P. V. Bushlanov and A. R. Oganov, *J. Phys. Chem. A*, 2021, **125**, 3936–3942.
30 D. Kraus, J. Vorberger, A. Pak, N. Hartley, L. Fletcher, S. Frydrych, E. Galtier, E. Gamboa, D. O. Gericke and S. Glenzer, *et al.*, *Nat. Astron*, 2017, **1**, 606–611.
31 D. Kraus, N. J. Hartley, S. Frydrych, A. K. Schuster, K. Rohatsch, M. Rödel, T. E. Cowan, S. Brown, E. Cunningham, T. van Driel, L. B. Fletcher, E. Galtier, E. J. Gamboa, A. Laso Garcia, D. O. Gericke, E. Granados, P. A. Heimann, H. J. Lee, M. J. MacDonald, A. J. MacKinnon, E. E. McBride, I. Nam, P. Neumayer, A. Pak, A. Pelka, I. Prencipe, A. Ravasio, R. Redmer, A. M. Saunders, M. Schölmerich, M. Schörner, P. Sun, S. J. Turner, A. Zettl, R. W. Falcone, S. H. Glenzer, T. Döppner and J. Vorberger, *Phys. Plasmas*, 2018, **25**, 056313.
32 A. K. Schuster, N. J. Hartley, J. Vorberger, T. Döppner, T. van Driel, R. W. Falcone, L. B. Fletcher, S. Frydrych, E. Galtier, E. J. Gamboa, D. O. Gericke, S. H. Glenzer, E. Granados, M. J. MacDonald, A. J. MacKinnon, E. E. McBride, I. Nam, P. Neumayer, A. Pak, I. Prencipe, K. Voigt, A. M. Saunders, P. Sun and D. Kraus, *Phys. Rev. B*, 2020, **101**, 054301.
33 F. Ancilotto, G. L. Chiarotti, S. Scandolo and E. Tosatti, *Science*, 1997, **275**, 1288–1290.
34 B. L. Sherman, H. F. Wilson, D. Weeraratne and B. Militzer, *Phys. Rev. B: Condens. Matter Mater. Phys.*, 2012, **86**, 224113.
35 L. Spanu, D. Donadio, D. Hohl, E. Schwegler and G. Galli, *Proc. Natl. Acad. Sci. U. S. A.*, 2011, **108**, 6843–6846.
36 G. Gao, A. R. Oganov, Y. Ma, H. Wang, P. Li, Y. Li, T. Iitaka and G. Zou, *Chem. Phys.*, 2010, **133**, 144508.
37 D. Murayama, S. Ohmura, R. Kodama and N. Ozaki, *J. Appl. Phys.*, 2023, **134**, 095902.
38 G. Kerley, *J. Appl. Phys.*, 1980, **51**, 5368–5374.
39 U. Setzmann and W. Wagner, *J. Phys. Chem. Ref. Data*, 1991, **20**, 1061–1155.
40 M. Bykov, E. Bykova, C. J. Pickard, M. Martinez-Canales, K. Glazyrin, J. S. Smith and A. F. Goncharov, *Phys. Rev. B*, 2021, **104**, 184105.
41 M. Bethkenhagen, E. R. Meyer, S. Hamel, N. Nettelmann, M. French, L. Scheibe, C. Ticknor, L. A. Collins, J. D. Kress and J. J. Fortney, *et al.*, *Astrophys. J.*, 2017, **848**, 67.
42 R. Hu, Y. Li, C. Wang, Y. Hu and M. Lv, *Phys. Rev. B*, 2023, **107**, 174108.
43 U. Ranieri, L. J. Conway, M.-E. Donnelly, H. Hu, M. Wang, P. Dalladay-Simpson, M. Peña-Alvarez, E. Gregoryanz, A. Hermann and R. T. Howie, *Phys. Rev. Lett.*, 2022, **128**, 215702.
44 M. Somayazulu, L. Finger, R. Hemley and H. Mao, *Science*, 1996, **271**, 1400–1402.
45 W. L. Mao, V. V. Struzhkin, H.-K. Mao and R. J. Hemley, *Chem. Phys. Lett.*, 2005, **402**, 66–70.
46 Y. Liu, D. Duan, F. Tian, X. Huang, D. Li, Z. Zhao, X. Sha, B. Chu, H. Zhang and B. Liu, *et al.*, *RSC Adv.*, 2014, **4**, 37569–37574.
47 G. Saleh and A. R. Oganov, *Sci. Rep.*, 2016, **6**, 32486.
48 A. S. Naumova, S. V. Lepeshkin and A. R. Oganov, *J. Phys. Chem. C*, 2019, **123**, 20497–20501.
49 W. Cui, T. Bi, J. Shi, Y. Li, H. Liu, E. Zurek and R. J. Hemley, *Phys. Rev. B*, 2020, **101**, 134504.
50 A. F. Goncharov, E. Bykova, M. Bykov, X. Zhang, Y. Wang, S. Chariton, V. B. Prakapenka and J. S. Smith, *J. Appl. Phys.*, 2022, **131**, 025902.
51 A. B. Zylstra, A. L. Kritcher, O. A. Hurricane, D. A. Callahan, J. E. Ralph, D. T. Casey, A. Pak, O. L. Landen, B. Bachmann, K. L. Baker, L. Berzak Hopkins, S. D. Bhandarkar, J. Biener, R. M. Bionta, N. W. Birge, T. Braun, T. M. Briggs, P. M. Celliers, H. Chen, C. Choate, D. S. Clark, L. Divol, T. Döppner, D. Fittinghoff, M. J. Edwards, M. Gatu Johnson, N. Gharibyan, S. Haan, K. D. Hahn, E. Hartouni, D. E. Hinkel, D. D. Ho, M. Hohenberger, J. P. Holder, H. Huang, N. Izumi, J. Jeet, O. Jones, S. M. Kerr, S. F. Khan, H. Geppert Kleinrath, V. Geppert Kleinrath, C. Kong, K. M. Lamb, S. Le Pape, N. C. Lemos, J. D. Lindl, B. J. MacGowan, A. J. Mackinnon, A. G. MacPhee, E. V. Marley, K. Meaney, M. Millot, A. S. Moore, K. Newman, J.-M. G. Di Nicola, A. Nikroo, R. Nora, P. K. Patel, N. G. Rice, M. S. Rubery, J. Sater, D. J. Schlossberg, S. M. Sepke, K. Sequoia, S. J. Shin, M. Stadermann, S. Stoupin, D. J. Strozzi, C. A. Thomas, R. Tommasini, C. Trosseille, E. R. Tubman, P. L. Volegov, C. R. Weber, C. Wild, D. T. Woods, S. T. Yang and C. V. Young, *Phys. Rev. E*, 2022, **106**, 025202.
52 A. B. Zylstra, O. A. Hurricane, D. A. Callahan, A. L. Kritcher, J. E. Ralph, H. F. Robey, J. S. Ross, C. V. Young, K. L. Baker, D. T. Casey, T. Döppner, L. Divol, M. Hohenberger, S. Le Pape, A. Pak, P. K. Patel, R. Tommasini, S. J. Ali, P. A. Amendt, L. J. Atherton, B. Bachmann, D. Bailey, L. R. Benedetti, L. Berzak Hopkins, R. Betti, S. D. Bhandarkar, J. Biener, R. M. Bionta, N. W. Birge, E. J. Bond, D. K. Bradley, T. Braun, T. M. Briggs, M. W. Bruhn, P. M. Celliers, B. Chang, T. Chapman, H. Chen, C. Choate, A. R. Christopherson, D. S. Clark, J. W. Crippen, E. L. Dewald, T. R. Dittrich, M. J. Edwards, W. A. Farmer, J. E. Field, D. Fittinghoff, J. Frenje, J. Gaffney, M. Gatu Johnson, S. H. Glenzer, G. P. Grim, S. Haan, K. D. Hahn, G. N. Hall, B. A. Hammel, J. Harte, E. Hartouni, J. E. Heebner, V. J. Hernandez, H. Herrmann, M. C. Herrmann, D. E. Hinkel, D. D. Ho, J. P. Holder, W. W. Hsing, H. Huang, K. D. Humbird, N. Izumi, L. C. Jarrott, J. Jeet, O. Jones, G. D. Kerbel, S. M. Kerr, S. F. Khan, J. Kilkenny, Y. Kim, H. Geppert Kleinrath, V. Geppert Kleinrath, C. Kong, J. M. Koning, J. J. Kroll, M. K. G. Kruse, B. Kustowski, O. L. Landen, S. Langer, D. Larson, N. C. Lemos, J. D. Lindl, T. Ma, M. J. MacDonald, B. J. MacGowan, A. J. Mackinnon, S. A. MacLaren, A. G. MacPhee, M. M. Marinak, D. A. Mariscal, E. V. Marley, L. Masse, K. Meaney, N. B. Meezan, P. A. Michel, M. Millot, J. L. Milovich, J. D. Moody, A. S. Moore, J. W. Morton, T. Murphy, K. Newman, J.-M. G. Di Nicola, A. Nikroo, R. Nora, M. V. Patel, L. J. Pelz, J. L. Peterson, Y. Ping, B. B. Pollock, M. Ratledge, N. G. Rice, H. Rinderknecht, M. Rosen, M. S. Rubery, J. D. Salmonson, J. Sater, S. Schiaffino, D. J. Schlossberg, M. B. Schneider, C. R. Schroeder, H. A. Scott, S. M. Sepke, K. Sequoia, M. W. Sherlock, S. Shin, V. A. Smalyuk, B. K. Spears, P. T. Springer, M. Stadermann, S. Stoupin, D. J. Strozzi, L. J. Suter, C. A. Thomas, R. P. J. Town, E. R. Tubman, C. Trosseille, P. L. Volegov, C. R. Weber,

 This journal is © the Owner Societies 2024

K. Widmann, C. Wild, C. H. Wilde, B. M. Van Wonterghem, D. T. Woods, B. N. Woodworth, M. Yamaguchi, S. T. Yang and G. B. Zimmerman, *Nature*, 2022, **601**, 542–548.
53 M. Podolak, R. Helled and G. Schubert, *Mon. Not. R. Astron. Soc.*, 2019, **487**, 2653–2664.
54 R. Redmer, T. R. Mattsson, N. Nettelmann and M. French, *Icarus*, 2011, **211**, 798–803.
55 L. Scheibe, N. Nettelmann and R. Redmer, *Astron. Astrophys.*, 2019, **632**, A70.
56 R. Helled, J. D. Anderson, M. Podolak and G. Schubert, *Astrophys. J.*, 2010, **726**, 15.
57 P. Peebles, *Astrophys. J.*, 1964, **140**, 328.
58 W. C. Demarcus, *Astron. J.*, 1958, **63**, 2.
59 R. Kubo, *JPSJ*, 1957, **12**, 570–586.
60 D. Greenwood, *Proc. Phys. Soc.*, 1958, **71**, 585.
61 G. Kresse and J. Hafner, *Phys. Rev. B: Condens. Matter Mater. Phys.*, 1993, **47**, 558–561.
62 G. Kresse and J. Hafner, *Phys. Rev. B: Condens. Matter Mater. Phys.*, 1994, **49**, 14251–14269.
63 G. Kresse and J. Furthmüller, *Phys. Rev. B: Condens. Matter Mater. Phys.*, 1996, **54**, 11169–11186.
64 G. Kresse and J. Furthmüller, *Comput. Mater. Sci.*, 1996, **6**, 15–50.
65 J. Hafner, *J. Comput. Chem.*, 2008, **29**, 2044–2078.
66 P. Hohenberg and W. Kohn, *Phys. Rev.*, 1964, **136**, B864–B871.
67 N. D. Mermin, *Phys. Rev.*, 1965, **137**, A1441–A1443.
68 M. Weinert and J. W. Davenport, *Phys. Rev. B: Condens. Matter Mater. Phys.*, 1992, **45**, 13709–13712.
69 R. M. Wentzcovitch, J. L. Martins and P. B. Allen, *Phys. Rev. B: Condens. Matter Mater. Phys.*, 1992, **45**, 11372–11374.
70 P. E. Blöchl, *Phys. Rev. B: Condens. Matter Mater. Phys.*, 1994, **50**, 17953–17979.
71 G. Kresse and D. Joubert, *Phys. Rev. B: Condens. Matter Mater. Phys.*, 1999, **59**, 1758–1775.
72 J. P. Perdew, K. Burke and M. Ernzerhof, *Phys. Rev. Lett.*, 1996, **77**, 3865–3868.
73 W. G. Hoover, *Phys. Rev. A*, 1985, **31**, 1695–1697.
74 N. Shuichi, *Prog. Theor. Phys.*, 1991, **103**, 1–46.
75 B. Holst, R. Redmer and M. P. Desjarlais, *Phys. Rev. B: Condens. Matter Mater. Phys.*, 2008, **77**, 184201.
76 A. Baldereschi, *Phys. Rev. B: Condens. Matter Mater. Phys.*, 1973, **7**, 5212–5215.
77 D. Li, P. Zhang and J. Yan, *Phys. Rev. B: Condens. Matter Mater. Phys.*, 2011, **84**, 184204.
78 B. Militzer, W. B. Hubbard, J. Vorberger, I. Tamblyn and S. Bonev, *Astrophys. J*, 2008, **688**, L45.
79 M. A. Morales, C. Pierleoni, E. Schwegler and D. M. Ceperley, *Proc. Natl. Acad. Sci. U. S. A.*, 2010, **107**, 12799–12803.
80 W. Hubbard, *Astrophys. J.*, 1972, **176**, 525.
81 D. J. Stevenson, *Phys. Rev. B: Condens. Matter Mater. Phys.*, 1975, **12**, 3999–4007.
82 J. Vorberger, I. Tamblyn, B. Militzer and S. A. Bonev, *Phys. Rev. B: Condens. Matter Mater. Phys.*, 2007, **75**, 024206.
83 C. Wang, X.-T. He and P. Zhang, *Phys. Rev. E*, 2013, **88**, 033106.
84 F. Soubiran and B. Militzer, *Astrophys. J*, 2015, **806**, 228.
85 F. Soubiran and B. Militzer, *Astrophys. J*, 2016, **829**, 14.
86 J.-F. Danel and L. Kazandjian, *Phys. Rev. E*, 2015, **91**, 013103.
87 M. Bethkenhagen, D. Cebulla, R. Redmer and S. Hamel, *J. Phys. Chem. A*, 2015, **119**, 10582–10588.
88 B. Cheng, M. Bethkenhagen, C. J. Pickard and S. Hamel, *Nat. Phys.*, 2021, **17**, 1228–1232.
89 C. Cavazzoni, G. Chiarotti, S. Scandolo, E. Tosatti, M. Bernasconi and M. Parrinello, *Science*, 1999, **283**, 44–46.
90 D. Richters and T. D. Kühne, *JETP Lett.*, 2013, **97**, 184–187.
91 G. Tabak, J. R. Rygg, M. Millot, Y.-J. Kim, S. Hamel, P. M. Celliers, D. E. Fratanduono, S. Ali, D. Erskine, T. R. Boehly, T.-A. Suer, N. Dasenbrock-Gammon, R. Dias, S. Zhang, S. X. Hu, L. E. Hansen, B. J. Henderson, M. Zaghoo, T. Ogawa, D. Murayama, K. Miyanishi, N. Ozaki, T. Sano, R. Jeanloz, D. G. Hicks, J. H. Eggert and G. W. Collins, *Phys. Rev. B*, 2024, **109**, 064102.
92 S. Zhang, K. P. Driver, F. Soubiran and B. Militzer, *Phys. Rev. E*, 2017, **96**, 013204.
93 B. Cheng, S. Hamel and M. Bethkenhagen, *Nat. Commun.*, 2023, **14**, 1104.
94 M. Preising and R. Redmer, *Phys. Rev. B*, 2020, **102**, 224107.
95 M. French and R. Redmer, *Phys. Plasmas*, 2017, **24**, 092306.
96 M. Gajdoš, K. Hummer, G. Kresse, J. Furthmüller and F. Bechstedt, *Phys. Rev. B: Condens. Matter Mater. Phys.*, 2006, **73**, 045112.
97 B. Holst, M. French and R. Redmer, *Phys. Rev. B: Condens. Matter Mater. Phys.*, 2011, **83**, 235120.
98 M. French, G. Röpke, M. Schörner, M. Bethkenhagen, M. P. Desjarlais and R. Redmer, *Phys. Rev. E*, 2022, **105**, 065204.
99 D. Knyazev and P. Levashov, *Comput. Mater. Sci.*, 2013, **79**, 817–829.
100 J. W. Warwick, D. R. Evans, G. R. Peltzer, R. G. Peltzer, J. H. Romig, C. B. Sawyer, A. C. Riddle, A. E. Schweitzer, M. D. Desch and M. L. Kaiser, *et al.*, *Science*, 1989, **246**, 1498–1501.
101 N. Nettelmann, R. Helled, J. Fortney and R. Redmer, *Planet. Space Sci.*, 2013, **77**, 143–151.
102 N. Mott, *Metal-Insulator Transitions*, Taylor and Francis, London, 2nd edn, 1990.
103 A. Ioffe and A. Regel, *Non-crystalline, amorphous, and liquid electronic semiconductors: Progress in semiconductors*, 1960, pp. 237–291.
104 W. Nellis, R. Chau, P. P. Edwards and R. Winter, *Z. Phys. Chem.*, 2003, **217**, 795–802.
105 W. Nellis, *J. Condens. Matter Phys.*, 2004, **16**, S923.
106 W. B. Hubbard and J. J. MacFarlane, *J. Geophys. Res. Solid Earth*, 1980, **85**, 225–234.
107 N. Teanby, P. Irwin, J. Moses and R. Helled, *Philos. Trans. R. Soc., A*, 2020, **378**, 20190489.
108 R. V. Yelle, F. Herbert, B. R. Sandel, R. J. Vervack and T. M. Wentzel, *Icarus*, 1993, **104**, 38–59.

Supporting information

Mixture of Hydrogen and Methane under planetary interior conditions

Argha Jyoti Roy[1*], Armin Bergermann[1], Mandy Bethkenhagen[2], and Ronald Redmer[1]

[1]Institut für Physik, Universität Rostock, D-18051 Rostock, Germany
[2]LULI, CNRS, CEA, Sorbonne Université, École Polytechnique- Institut Polytechnique de Paris, 91128 Palaiseau, France

Table 1: DC Electrical conductivity data table of a dense hydrogen-methane mixture as a function of pressure along five isotherms.

Temperature [K]	Pressure [GPa]	ρ [g/cm³]	σ_0 [MS/m]
1000	73.329	1.32	7.245e-13
1000	183.56	1.85	9.438e-11
1000	555.88	2.90	0.18403
1000	820.58	3.43	0.89112
1000	978.44	3.70	1.3114
3000	18.340	0.74	1.55e-05
3000	83.345	1.32	0.001652
3000	181.253	1.85	0.44612
3000	360.770	2.42	0.96726
3000	571.341	2.90	1.41040
3000	857.916	3.43	1.89140
3000	1023.22	3.70	2.08960
4000	20.029	0.74	0.0020762
4000	79.360	1.32	0.22072
4000	187.621	1.85	0.70642
4000	373.578	2.42	1.1537
4000	588.299	2.90	1.5101
4000	878.583	3.43	2.0087
4000	1045.93	3.70	2.1885
6000	21.818	0.74	0.0937
6000	87.634	1.32	0.48127
6000	139.541	1.85	0.8759
6000	400.853	2.42	1.3064
6000	622.585	2.90	1.6207
6000	919.991	3.43	1.9678
6000	1090.9	3.70	2.1701
8000	26.165	0.74	0.173
8000	99.789	1.32	0.5657
8000	225.617	1.85	0.9328
8000	427.99	2.42	1.3204
8000	655.760	2.90	1.6239
8000	959.95	3.43	1.9382
8000	1134.19	3.70	2.1547
16000	51.0504	0.74	0.2536
16000	151.645	1.32	0.6311
16000	302.54	1.85	0.9636
16000	532.03	2.42	1.3016
16000	782.378	2.90	1.6067
16000	1112.14	3.43	1.8874
16000	1297.24	3.70	2.0104

*corresponding author: argha.roy@uni-rostock.de

Table 2: Electrical conductivity data along the P-T profile of Uranus[1] as a function of radius of the planet.

Pressure [GPa]	**Temperature [K]**	**r/R_p**	**σ_0 [MS/m]**
17.157	2445.52	0.783	1.123e-06
39.40	3000	0.7117	0.007115
78.90	3646.30	0.6587	0.1473
126.78	4176.87	0.6057	0.4967
194.26	4758.55	0.5377	0.7894
279.60	5285.71	0.4577	1.1097
400.853	6000	0.3447	1.338
499.44	6231.78	0.2467	1.4953
773.66	6523.89	0.0432	1.8446

References:

1. N. Nettelmann, R Helled, J. Fortney and R. Redmer, Planet. Space Sci., 2013, 77, 143-151.

6.2 Understanding the transport properties of methane–hydrogen mixtures under the interior conditions of ice giants

- **A. J. Roy:** Preparation of the manuscript, conducting DFT-MD simulation, data analysis and interpretation of the results.
- **M. Bethkenhagen:** Preparation of the manuscript, interpretation of the results.
- **A. Bergermann:** Preparation of the manuscript, interpretation of the results.
- **R. Redmer:** Supervision of the project, preparation of the manuscript, interpretation of the results

The Astrophysical Journal, 990:212 (13pp), 2025 September 10 https://doi.org/10.3847/1538-4357/adf5be
© 2025. The Author(s). Published by the American Astronomical Society.
OPEN ACCESS

Understanding the Transport Properties of Methane–Hydrogen Mixtures under the Interior Conditions of Ice Giants

Argha Jyoti Roy[1,2], Mandy Bethkenhagen[3], Armin Bergermann[1,4], and Ronald Redmer[1]
[1] Institut für Physik, Universität Rostock, D-18051 Rostock, Germany; argha.roy@uni-rostock.de
[2] Helmholtz-Zentrum Dresden-Rossendorf, Bautzner Landstr. 400, 01328 Dresden, Germany
[3] LULI, CNRS, CEA, Sorbonne Université, École Polytechnique, Institut Polytechnique de Paris, 91128 Palaiseau, France
[4] SLAC National Accelerator Laboratory, 2575 Sand Hill Road, MS 72 Menlo Park, CA 94025, USA
Received 2025 April 22; revised 2025 July 22; accepted 2025 July 28; published 2025 September 10

Abstract

Inaccuracy in our knowledge of the transport properties of relevant mixtures under planetary interior conditions is a roadblock in predicting the observable properties of planets in our solar system and beyond. In this work, we investigate methane–hydrogen mixtures using data sets obtained from density functional theory calculations for the electronic structure, combined with molecular dynamics simulations for the ions for a wide range of pressure and temperature. Hydrogen concentration significantly affects the equation of state (EOS) but has little influence on transport properties. We provide an analytical expression to model thermal EOS and transport properties as a function of hydrogen content, with the maximum deviation observed at low P–T conditions. These insights are particularly relevant to improve the planetary models and enhance our ability to predict the properties of "ice" giants and beyond.

Unified Astronomy Thesaurus concepts: Uranus (1751); Neptune (1096); Methane (1042)

1. Introduction

Ice giants Uranus and Neptune are the least explored and are still relatively unknown planets in our solar system. Besides the Voyager 2 flyby, both planets still await dedicated orbiter missions similar to Juno (Jupiter) and Cassini-Huygens (Saturn) (see M. Dougherty et al. 2009; S. J. Bolton et al. 2017) respectively. Ideally, we need missions that include entry probes to gather essential data for a better understanding of their interior structure, chemical composition, thermal evolution, and magnetic field structure. The recent Planetary Science and Astrobiology Decadal Survey (National Academies of Sciences, Engineering, and Medicine 2022) has recommended such an orbiter and probe to in situ explore Uranus as NASA's highest-priority mission (see K. E. Mandt 2023). In order to study the planetary properties, interior models are used that solve the structure equations (D. J. Stevenson et al. 1982; T. Guillot 1999; T. Guillot et al. 2015). Standard three-layer models are used as long as accurate gravity data from an orbiter mission are unavailable. Many such models have been proposed for the concerned planets; e.g., adiabatic cooling schemes using the equation of state (EOS) of "ice" materials at 0 K fail to explain the rate of cooling concerning the present-day luminosity (W. Hubbard 1978; W. B. Hubbard & J. J. MacFarlane 1980). Thermal evolution calculations (J. J. Fortney et al. 2011; N. Nettelmann et al. 2013; E. F. Linder et al. 2019; L. Scheibe et al. 2019), assuming adiabatic cooling of three-layer models, are used to explain the present-day luminosity of Uranus and Neptune.

With the different approaches to the problem, the basic input is EOS of the relevant materials, i.e., H–He (outer envelope), an icy mixture H-C-N-O (inner envelope), and rocks (core). For instance, R. Redmer et al. (2011), found excellent agreement of their interior model based on ab initio EOS data of hydrogen, helium, and water mixture with the proposed thin shell geometry of dynamo models by S. Stanley & J. Bloxham (2004) and S. Stanley & J. Bloxham (2006).

The ice giants are predominantly composed of so-called "ices" and "rocks," unlike Jupiter and Saturn, which are dominated by hydrogen and helium. The term "ices" subsumes compounds such as water (H_2O), ammonia (NH_3), and methane (CH_4), while "rocks" stand for silicate materials ($MgSiO_3$, SiO_2). Deep within the planetary interior, the chemistry and physical nature of these "ices" play an important role in their properties. For instance, water and ammonia transform into superionic phases (M. French et al. 2009; M. Bethkenhagen et al. 2013), and methane decomposes into diamond and sinks deeper into the planet due to gravity, leaving possibly a metallic hydrogen-rich phase (M. Ross 1981; L. R. Benedetti et al. 1999; B. Cheng et al. 2023). This could also be a source of heating in these planets, especially in Neptune, due to its higher luminosity than Uranus (M. Podolak & R. Helled 2012; L. Scheibe et al. 2019). Even in the atmospheres of Uranus and Neptune, due to the abundance of hydrocarbons, these two planets appear in a distinct bluish hue due to absorption of the red light (P. G. Irwin et al. 2022). While studying pure systems offers useful insights, it is essential to recognize that hydrogen, methane, and other hydrocarbons are typically found in mixtures in nature, and the interaction among the atoms can substantially affect the understanding of planet's observable properties.

Recent experimental campaigns have provided critical insights into the behaviors of pure fluids under these extreme conditions, which are particularly relevant to understanding the interiors of ice giants. For example, G. Tabak et al. (2024) reached about 400 GPa on precompressed pure methane samples in diamond-anvil cells (DACs), where the experiments showed consistency with density functional theory-molecular dynamics (DFT–MD) simulations predicting a polymeric region. Additionally, laser-driven shock compression on complex hydrocarbons such as polystyrene by

Original content from this work may be used under the terms of the Creative Commons Attribution 4.0 licence. Any further distribution of this work must maintain attribution to the author(s) and the title of the work, journal citation and DOI.

D. Kraus et al. (2017) and Z. He et al. (2022) showed the formation of diamonds under conditions similar to Uranus and Neptune. Findings from M. Frost et al. (2024) showed diamond formation from statically compressed polystyrene above a temperature of 2500 K, at pressures ranging from 19 to 27 GPa.

Several stable high-pressure compounds of methane–hydrogen mixture were studied in combination with X-ray diffraction experiments performed in DACs and ab initio simulation, as shown by U. Ranieri et al. (2022). Various mixtures under the same conditions have also been studied using DFT–MD techniques; however, the additive volume rule, applied at constant pressure and temperature, also known as linear mixing approximation (LMA), is the consistent one. The method is used for many different mixtures such as H–He (F. Soubiran & B. Militzer 2015), for gas giants with the inclusion of heavier species such as C, N, O, Si, and Fe (F. Soubiran & B. Militzer 2016), and for hydrocarbon C_2H_3 as a C and H mixture (J.-F. Danel & L. Kazandjian 2015). Similarly, M. Bethkenhagen et al. (2017) showed a maximum deviation of 4% in a mixture of CH_4, H_2O, and NH_3. Our previous work (A. J. Roy et al. 2024) testing the LMA also showed the same deviation of 4% in a binary mixture of CH_4 and H_2, as we found the clustering of carbon to occur at lower pressure in the presence of hydrogen than in pure methane and band gap closure is driven by metallic hydrogen at a lower temperature in comparison to pure methane (B. L. Sherman et al. 2012) and methane–water mixture (R. Hu et al. 2023).

Hence, we focus on extending the database of mixture and focus on transport properties. We use ab initio simulations and the Kubo–Greenwood formalism (R. Kubo 1957; D. Greenwood 1958) to understand better the EOS and transport properties of CH_4–H_2. Based on these results, we present an analytical model for the EOS and the transport properties as a function of hydrogen concentration. Our paper is organized as follows: In section 2, we explain the computational methods. Section 3 outlines the findings of this work. The EOS of the methane–hydrogen mixtures is discussed in Section 3.1, and we test the LMA with respect to the hydrogen molecular mass fraction. The transport properties of the pure substances and of the mixtures, as well as analytical model, are presented in Section 3.2. We discuss the behavior of the pure components and mixtures in the degenerate domain, i.e., the Wiedemann–Franz law in Section 3.3. In Section 4, we discuss the implications of our results, and Section 5 summarizes our findings.

2. Computational Details and Methods

The entire data set was obtained from DFT–MD simulations using the Vienna Ab Initio Simulation Package (VASP; G. Kresse & J. Hafner 1993, 1994; G. Kresse 1996; G. Kresse & J. Furthmüller 1996; J. Hafner 2008). The electronic and ionic dynamics are decoupled according to the Born–Oppenheimer approximation. The choice of the exchange-correlation (XC) functional plays a crucial role in determining the accuracy and computational costs of DFT calculations. As shown by A. Bergermann et al. (2024), computationally expensive XC functionals such as that of Heyd, Scuseria, and Ernzerhof (J. Heyd et al. 2003; see also J. Heyd & G. E. Scuseria 2004a, 2004b) shift the critical point of the first-order liquid–liquid phase transition in pure hydrogen by 22% in pressure and 150 K in temperature. However, the costs of such DFT–MD are almost 25 times and optical routines about 100 times (depending on the k-mesh grid) more than conventional generalized gradient approximation (GGA) calculations, and the cost increases further for complex molecules such as methane. Hence, for the evaluation of electronic properties, we used the GGA of Perdew, Burke, and Ernzerhof (PBE; J. P. Perdew et al. 1996) as the XC functional. The ionic trajectories are calculated using classical equations of motion and the Verlet algorithm, with the forces between electrons and ions obtained from the Hellman–Feynman theorem. This procedure combines DFT and classical MD simulations and allows us to treat systems at finite temperatures (P. Hohenberg & W. Kohn 1964; N. D. Mermin 1965; M. Weinert & J. Davenport 1992; R. M. Wentzcovitch et al. 1992). We set the plane wave cutoff energy to 1100 eV for every simulation and use projected augmented wave (PAW) pseudopotentials for hydrogen (PAW PBE H_h 06Feb2004) and carbon (PAW PBE C_h 06Feb2004; P. E. Blöchl 1994; G. Kresse & D. Joubert 1999). We control the temperature with the Nosé–Hoover thermostat (W. G. Hoover 1985; N. Shuichi 1991) with a Nosé–mass parameter corresponding to a temperature oscillation period of one per 40 time steps. The simulation box contains either two number combinations, i.e., 54 and 27 number of molecules of methane and hydrogen (2:1) and vice versa (1:2). We sampled the Brillouin zone with Baldereschi k-point (A. Baldereschi 1973). We choose a time step of 0.25 fs for every simulation. We continued the simulations for 8–12 ps after equilibration to evaluate thermodynamic and electrical properties. For pure H_2 and the 2:2 mixture, i.e., 54 molecules of methane and hydrogen, the data were obtained from the previous publication (A. J. Roy et al. 2024). For pure methane, we used the work of M. Bethkenhagen et al. (2017). All number permutations utilized in this work correspond to the molecular mass fractions (see Table 1) according to the following equation:

Table 1
Molecular Mass Fraction according to Equation (1) Related to the Molecule Number Combination

System	$\mathcal{X}_{H_2}$	$\mathcal{X}_{CH_4}$
Pure CH_4	0.000	1.000
[2:1] CH_4–H_2	0.059	0.941
[2:2] CH_4–H_2	0.116	0.884
[1:2] CH_4–H_2	0.2008	0.7992
Pure H_2	1.000	0.000

$$\mathcal{X}_i = \frac{n_i M_i}{\sum_i M_i}, \tag{1}$$

where n_i and M_i are the number and molar mass of element i in the mixture, respectively.

The framework of linear response theory provides a means of calculating transport properties for our DFT–MD simulations. Though DFT, in principle, is a single-particle mean-field theory, the Kubo–Greenwood formalism works very well in tandem. In order to calculate the electronic properties for our DFT–MD simulations, we evaluate 40–100 snapshots for each simulation, depending on the system, using a Monkhorst-Pack k-point mesh of $4 \times 4 \times 4$ to sample the Brillouin zone and perform static DFT runs to evaluate dynamic Onsager coefficients (see Equation (2)) in the framework of linear

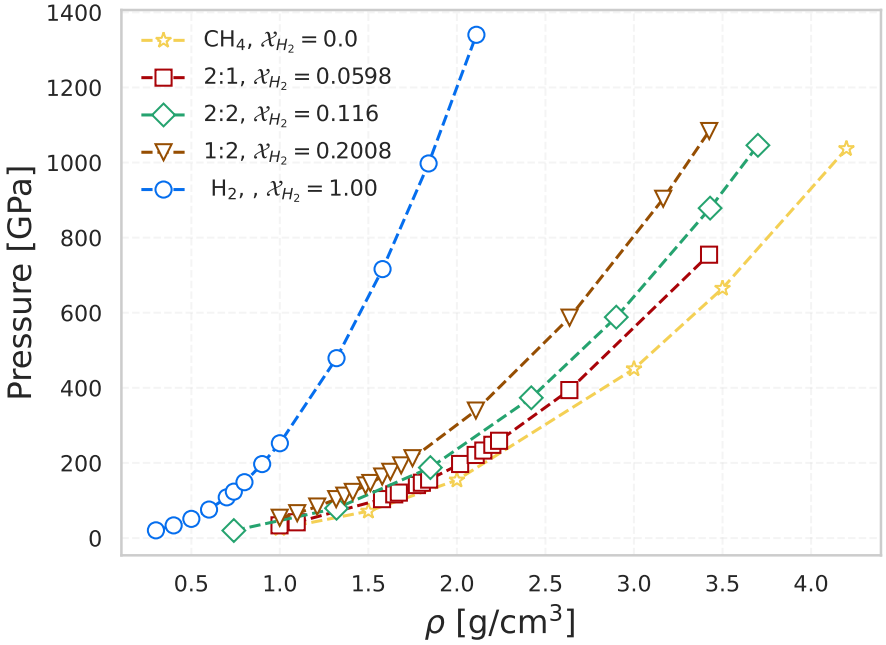


Figure 1. EOS along an isotherm of $T = 4000$ K as a function of density for all the considered systems (color coded).

response theory (B. Holst et al. 2011):

$$L_n(\omega) = \frac{2\pi(-1)^n}{V\omega} \sum_{\boldsymbol{k}\alpha\beta} \mathbf{Re}(\langle \boldsymbol{k}\alpha|\boldsymbol{v}|\boldsymbol{k}\beta\rangle \otimes \langle \boldsymbol{k}\beta|\boldsymbol{v}|\boldsymbol{k}\alpha\rangle)(f_{\boldsymbol{k}\alpha} - f_{\boldsymbol{k}\beta}) \times \left(\frac{\epsilon_{\boldsymbol{k}\alpha} + \epsilon_{\boldsymbol{k}\beta}}{2} - h_e\right)^n \delta(\epsilon_{\boldsymbol{k}\alpha} - \epsilon_{\boldsymbol{k}\beta} - \hbar\omega)\,, \quad (2)$$

where ω is the frequency, $\hbar$ is the reduced Planck constant, V is the volume of the simulation box, $|\boldsymbol{k}\alpha\rangle$ are the Bloch states—where, $\boldsymbol{k}$ is the reciprocal wavevector and α, β are the band indices, having eigen energy $\epsilon_{\boldsymbol{k}\alpha}$, $\boldsymbol{v}$ is the velocity operator, $f_{\boldsymbol{k}\mu}$ is the Fermi distribution function, and h_e is the enthalpy per electron. The matrix elements $\langle \boldsymbol{k}\alpha|\boldsymbol{v}|\boldsymbol{k}\beta\rangle$ are calculated using optical routines of VASP. The delta function is replaced by a Gaussian broadening, which is required to circumvent the discrete spectrum of eigenvalues arising from the periodic boundary constraining the simulation box (B. Holst et al. 2008, 2011; D. Knyazev & P. Levashov 2013; M. French et al. 2022).

The macroscopic transport coefficients are determined by the zero-frequency value of the Onsager coefficients given by Equation (2). The electrical conductivity follows from

$$\sigma = e^2 \lim_{\omega\to 0} L_0(\omega)\,, \quad (3)$$

and the thermal conductivity is determined via

$$\lambda = \frac{1}{T} \lim_{\omega\to 0} (L_2(\omega) - L_1(\omega) L_0^{-1}(\omega) L_1(\omega))\,. \quad (4)$$

3. Results

3.1. EOS

In Figure 1, we present a comprehensive analysis of the EOS of pure and mixed methane–hydrogen systems at $T = 4000$ K. For the isotherms of T= 3000 K and 6000 K, we provide the EOS in Figure 6 in the Appendix. Quantities such as pressure P and temperature T are calculated by averaging over the simulation after equilibration. Temperature is determined through the motion of ions, while pressure is assessed according to the relation

$$P_T = \rho k_b T + P_e, \quad (5)$$

where P_e is the virial pressure of electrons, ρ the ion number density, and k_b is the Boltzmann constant. Our findings reveal a significant difference in the slope $\frac{\Delta P}{\Delta \rho}$, with hydrogen exhibiting a steeper slope. As the volume of the simulation box decreases, the dissociation of the molecules starts to increase, leading to a sharp rise, particularly for hydrogen. Dissociation creates a more homogeneous electronic charge density, intensifying the forces between electron clouds. Importantly, we have chosen our conditions to avoid any discontinuous first-order phase transition in pure hydrogen (W. Lorenzen et al. 2010; M. Zaghoo et al. 2016), although we cross the 50% dissociated line at $T = 3000$ K, as noted by I. Tamblyn & S. A. Bonev (2010). The structural transformation of the pure components significantly influences electronic arrangements in the mixture. However, it is unclear whether the hydrogen molecules in the mixture or the mixture of C–H altogether undergo a first-order phase transition. Notably, D. Murayama et al. (2023) demonstrated that the strong covalent nature of C–C remains intact at densities up to 3 g cm^{-3} at low temperatures, while methane starts to become unstable at around 4000 K.

In the case of pure methane, the rise of pressure with increasing density is at a slower rate compared to hydrogen, as methane remains molecular. However, as density increases further, methane dissociates, releasing hydrogen. When we increase the number of hydrogen molecules in the mixture to a molecular mass fraction of $\mathcal{X}_{H_2} = 0.2008$, we see a sharp rise

Table 2
Fitted Parameters Obtained from Equation (7) for Different Hydrogen Mass Fractions at Selected Temperatures

$\mathcal{X}_{H_2}$ / T [K]	A [GPa]			B [GPa]$^{1/c}$			c		
	3000	4000	6000	3000	4000	6000	3000	4000	6000
0.059	556.086	67.965	60.5415	−555.514	67.102	−31.589	0.6	2.36	2.16
0.116	157.324	63.5897	80.0283	−179.596	−41.995	−34.809	1.3	2.6	2.16
0.2008	282.103	153.063	243.737	152.890	−76.5746	−128.436	2.9	2.0	1.00

in the pressure. In the mixture with a molecular mass fraction of $\mathcal{X}_{H_2} = 0.059$, where the methane molecule is twice the hydrogen molecule, we see a decremental effect on pressure. Notably, the pressure for $\mathcal{X}_{H_2} = 0.2008$ mixture is 100 GPa higher than the pressure of the $\mathcal{X}_{H_2} = 0.059$ mixture at the same density, and this difference grows with the increasing density. For the mixture with $\mathcal{X}_{H_2} = 0.116$, the isotherm sits almost in the middle of the other isotherms of either mixture. The sharp changes in the slopes as a function of hydrogen concentration are attributed to additional hydrogen and the hydrogen from the methane. When either component dominates in molecular mass fraction, the overall motion of ions slightly dominates over the other.

The robust bonding between the carbon atoms results in larger molecules that occupy volume and make the pure methane hard to compress as a whole. This effect is observed in the all the mixtures, with formation of cluster of carbon at a lower pressure due to added hydrogen molecules (A. J. Roy et al. 2024); this may influence carbon cluster structures formed within these temperature and pressure conditions inside a planet such that they will be amorphous before reaching the deep interior.

Modeling the interior of planets requires not only the knowledge of the EOS of relevant materials but also an understanding of how it changes due to varying composition. Therefore, we provide a means of modeling the thermal EOS of the mixture of methane and hydrogen as a function of hydrogen molecular mass fraction ($\mathcal{X}$), incorporating nonideal effects. Our model consists of the ideal contributions, i.e., the linear mixing of pressure and ideal configuration entropy, each weighted by the molecular mass fraction. Here, P_i represents the pressure of the pure components methane and hydrogen, respectively, and R is the universal gas constant. To encapsulate the nonideal effect, an additional term ΔP is introduced:

$$P_{\rm fit}(\mathcal{X}, \rho, T) = \sum_i \mathcal{X}_i P_i(\rho, T) + RT\rho \sum_i \mathcal{X}_i \log \mathcal{X}_i + \Delta P, \quad (6)$$

$$\Delta P(\mathcal{X}, \rho) = \mathcal{X}_{H_2}(1 - \mathcal{X}_{H_2})(A + B\rho^c). \quad (7)$$

The excess pressure ΔP is modeled using the polynomial expansion technique given by O. Redlich & A. T. Kister (1948) to map the excess thermodynamic quantity in binary mixtures. However, we modify the expression by replacing the summation with a polynomial fit to incorporate the increasing difference between the pressure from DFT–MD and ideal mixing, as given in Equation (7). We interpolate the pressure of pure components on to the density axis of the respective mixture, and we utilize least-square fitting to determine the best-fit values for the coefficients A, B, and c. The fitted parameters are given in Table 2 for each isotherm. In Figure 2, we present deviation of the thermal EOS from the DFT–MD for all the mixtures using Equations (6) and (7). For the lowest and highest concentration of hydrogen, the deviation does not exceed more than 5%; however, for $\mathcal{X}_{H_2}$= 0.116, the deviation exceeds more than 8% at 1.00 g cm^{-3}, coinciding with dissociation of the hydrogen molecule. We note that the deviation tends to be high in regions of interpolation between isochores and/or isotherms, indicating that the fluctuation of cubic splines significantly contributes to the error.

Alongside the model for thermal EOS, planetary interior modelers rely on mixing the EOS of pure materials linearly at constant pressure and temperature, i.e., LMA. Based on the work of W. C. Demarcus (1958) and P. J. E. Peebles (1964), we extract density and specific internal energy as given in the following equations:

$$\frac{1}{\rho_{\rm LM}(P, T)} = \sum_{j=1}^{N} \frac{\mathcal{X}_j}{\rho_j(P, T)}, \quad (8)$$

and, for the specific internal energy,

$$u_{\rm LM}(P, T) = \sum_{j=1}^{N} \mathcal{X}_j u_j(P, T), \quad (9)$$

where, ρ_j, u_j, and $\mathcal{X}_j$ are the density, specific internal energy, and mass fraction, respectively, of individual components j of the mixture comprised of N components. The deviations from real mixtures are calculated using the following equations:

$$\Delta\rho(P, T) = \frac{\rho_{\rm LM}(P, T)}{\rho_{\rm real}(P, T)} - 1, \quad (10)$$

$$\Delta u(P, T) = u_{\rm LM}(P, T) - u_{\rm real}(P, T). \quad (11)$$

In Figure 7 (see the Appendix), we present the deviation in density and specific internal energy between the real mixture (DFT–MD) and LMA for molecular mass fraction of $\mathcal{X}_{H_2}$= 0.059 and 0.2008. The maximum deviation in density and specific energy occurs at 3000 K, with the deviations decreasing as the pressure and temperature increase. A similar trend in the deviations is observed as the temperature increases for $\mathcal{X}_{H_2} = 0.2008$. However, no such trend can be established with the pressure increase, with the maximum deviation of 3.8 kJ g^{-1} occurring at 3000 K. The overall deviations in both quantities do not exceed 4%, holding the LMA good within the considered P–T space for the respective molecular mass fraction, $\mathcal{X}_{H_2}$.

3.2. Transport Properties

Figure 3 and Figure 8 (see the Appendix) depict the electrical properties of the pure and mixed systems along the isotherms of $T = 4000$ K. We see a systematic increase of the electrical conductivity with increasing pressure. The system changes from a molecular to an atomic phase with a typical metallic conductivity. For pure methane, the electrical

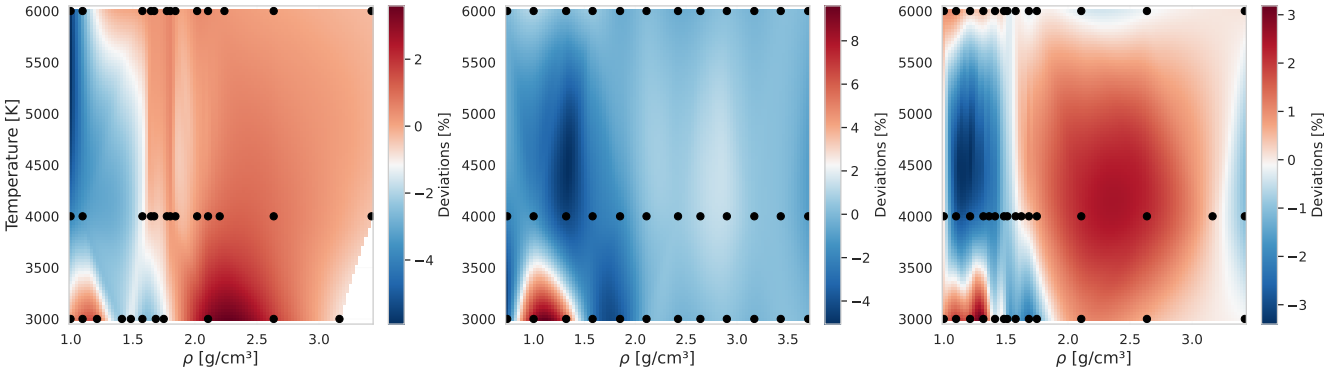


Figure 2. Deviations in pressure from the real CH_4–H_2 mixtures $\mathcal{X}_{H_2} = 0.059$ (left), $\mathcal{X}_{H_2} = 0.116$ (middle), $\mathcal{X}_{H_2} = 0.2008$ (right), and the predicted from analytical model Equation (6). Black dots denote the DFT–MD points. Between the isotherms and isochores, we interpolated the deviations cubically.

conductivity is substantially lower than for pure hydrogen, even at higher pressures. One would expect a similar conductivity since every methane molecule yields four hydrogen atoms upon dissociation. However, carbon has a large scattering cross section and the formation of clusters, i.e., polymers, which restricts the transport of the free electrons. Doubling the number of hydrogen molecules increases the overall electrical conductivity (star symbol in Figure 3) by a factor of about 1.5 with respect to pure methane; however, it remains about 2.5 times less than that of pure H_2. A similar trend is observed for thermal conductivity, where heat transfer becomes less efficient with the presence of methane molecules that provide thermal insulation. Such an effect has been previously reported by W. Lorenzen et al. (2011) and M. French et al. (2012), where the electrical and thermal conductivity decreased systematically with increasing helium concentration. In the methane–hydrogen mixtures, the slower rise of the steepness of the electrical and thermal conductivity curve could be attributed to two different mechanisms, metallization of hydrogen occurs due to the closing of the band gap, with a high degree of sensitivity to pressure increase, which is not observed for carbon atoms. This is due to the electronic structure of carbon, which is more resilient to changes in pressure due to the substantial overlap of orbitals among carbon atoms.

While mixing rules are well established and tested to obtain EOS data of mixtures from the EOS from pure species, few models were developed to depict optical properties. It is incredibly challenging to obtain such mixing rules based on data for pure components. Approximate methods such as those given by C. Starrett et al. (2012, 2020), W. Johnson et al. (2006), and M. Y. Kuchiev & W. R. Johnson (2008) include only information of the pure species and lack the input on cross-species correlations. The recent work of A. J. White et al. (2024) developed analytical models for mixing optical properties of CH mixtures, where the mixing rule describing low-frequency excitations does not match the high-frequency regime. Most of these studies are done in conditions relevant to inertial fusion confinement experiments and not necessarily for planetary conditions, where bonding and intermolecular interactions are important. We propose the following fit formulas for the electrical and thermal conductivity along the isotherms, where x is the pressure axis:

$$\lambda_{\rm fit},\ \sigma_{\rm fit}^{(4000-6000)\rm K} = Ax^m e^{-B/x^n} + Cx^d + E^k\ . \tag{12}$$

For the isotherm at $T = 3000$ K, we replace the power function in Equation (12) by a shifted sigmoid function as lower temperatures yield very low values for electrical conductivity, as shown in Equation (13). For thermal conductivity, Equation (12) provides a very good fit to the DFT data.

$$\sigma_{\rm fit}^{3000\rm K} = Ax^m e^{-B/x^n} + \frac{C}{1 + e^{-d(x-j)}} + E^k\ . \tag{13}$$

We use analytical fits to our data points to construct a model to describe the transport properties of mixtures, as shown in Figure 4 (e.g., we chose pure CH_4 and refer to Figure 9 in the Appendix for pure H_2) and the fitted parameters are provided in Table 3 and Table 4. Our fit reaches a minimal electrical and thermal conductivity value, with the first part of the fit equation being dominant, while the second part (power function or sigmoid function) dominates at higher pressure, with some deviations due to the analytical fit. The maximum deviation from the DFT points is observed to be about 9% and 12.5% in electrical and thermal conductivity, respectively. We observe that the maximum deviation for thermal conductivity occurs at around 75 GPa and 3000 K. For the electrical conductivity, it occurs at a lower pressure and temperature region, as well as at 25.15 GPa and 4000 K, as shown in Figures 4 and 9. Finding a trend of electronic properties along with temperature would require more isotherms, which we have not evaluated in this study. We provide σ and λ of pure species H_2 and CH_4 along isotherms, which were then used to model the transport properties of the mixtures.

Here we use two models, (i) a model proposed by A. Barysevich & S. Cherkas (2011), Equation (14), and (ii) the reciprocal model according to Equation (15):

$$\varphi_{\rm mix} = \varphi_{H_2}\left(1 + \frac{1 - \mathcal{X}_{H_2}}{\frac{\mathcal{X}_{H_2}}{n} - \frac{\varphi_{H_2}}{\varphi_{H_2} - \varphi_{CH_4}}}\right), \tag{14}$$

$$\frac{1}{\varphi_{\rm eff}} = \sum_i \frac{\mathcal{X}_i}{\varphi_i}\ , \tag{15}$$

where φ labels the electrical (σ) and thermal conductivity (λ). The numerical model (i) was introduced to model the electrical conductivity of copper obtained from wire

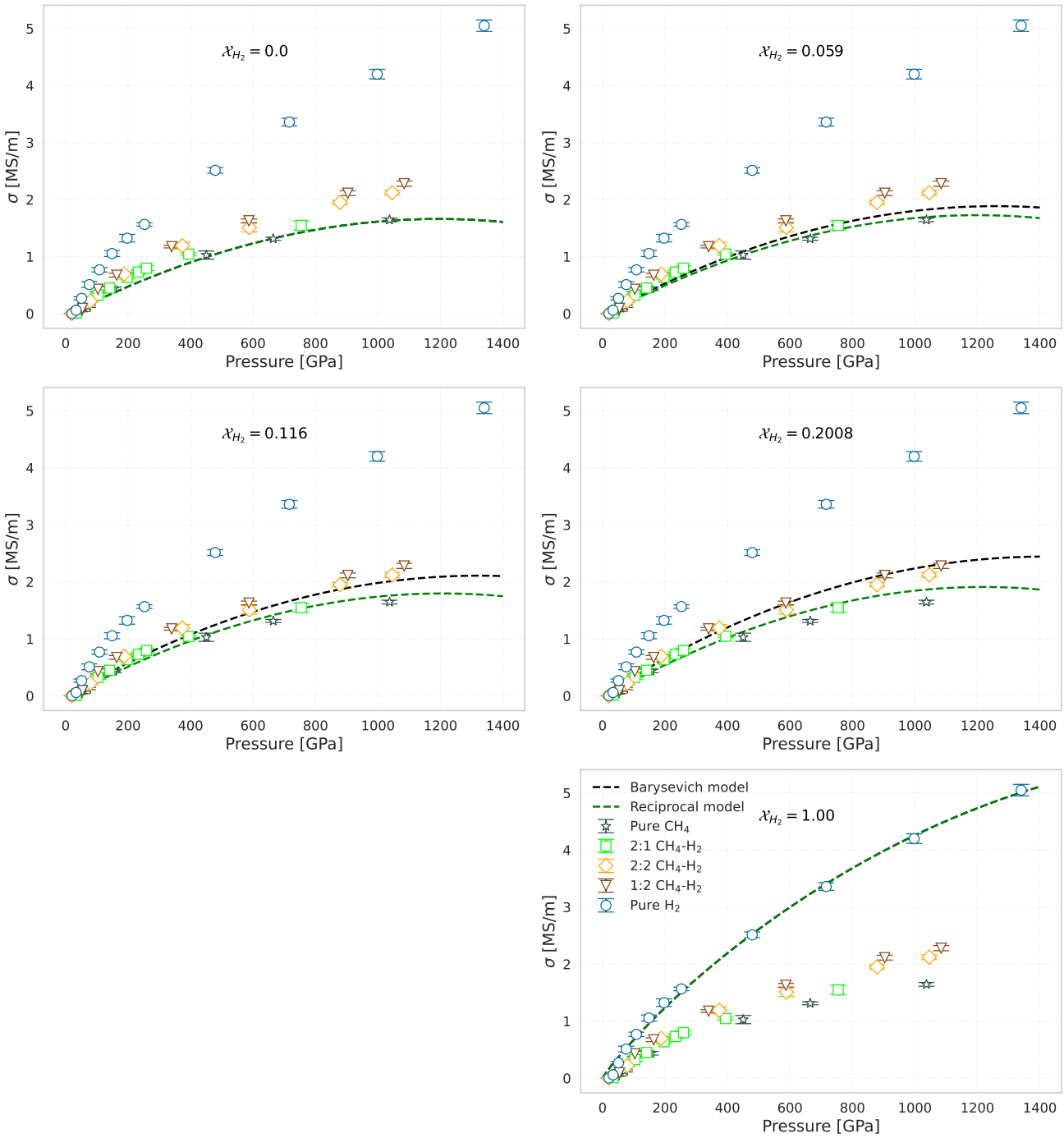
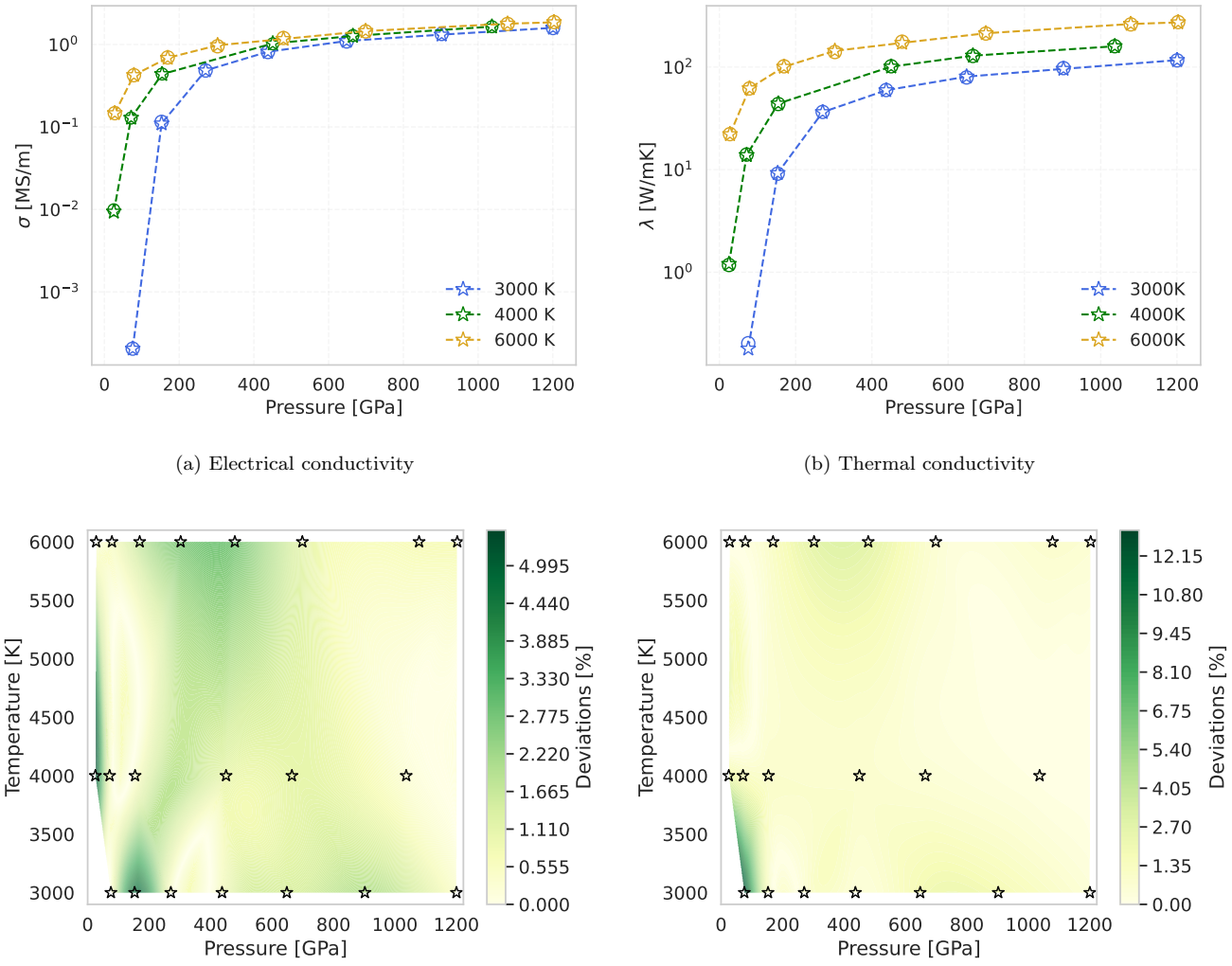


Figure 3. Electrical conductivity mixing models as function of pressure along an isotherm of 4000 K. Black broken line: (i) Barysevich model according to Equation (14) with $n = -2.8$. Green broken line: (ii) reciprocal mixing Equation (15). DFT–MD data are color-coded symbols; circles denote pure H_2, and stars denote pure CH_4. Diamond, triangles, and squares denote the various mixed systems.

explosions, including experimental and magnetohydrodynamic simulation data. The transport theory for heterogeneous systems allows modeling the conductivity also in the two-phase region, i.e., vapor and liquid (see Equation (14)). In our work, we used the same equation to model the electrical and thermal conductivity with the tuning parameter $n_\sigma = n_\lambda = -2.8$, for which our model predicts the trend better. Similarly, we also use the "resistance in series" model with the appropriate number fraction. Both models (i) and (ii) show a good agreement with the electrical and thermal conductivity data obtained from Equations (3) and (4) for pure methane and hydrogen (see Figure 3, Appendix Figure 8). Despite the origin of Equation (14) requiring a two-phase region, its predictions agree well with the trend of the simulation data, whereas the "resistance in series" model deviates substantially from DFT data as the pressure increases, predicting a decrease in the conductivity stronger than Equation (14).



(a) Electrical conductivity

(b) Thermal conductivity

(c) Deviations in electrical conductivity

(d) Deviations in thermal conductivity

Figure 4. (a), (b) Electrical and thermal conductivity of pure CH_4 as a function of pressure along the isotherms. The hollow circles represents the points obtained from the fit Equations (12) and (13), and hollow stars denote DFT simulation data using Equation (2). The deviations between the predicted values of the fits using Equations (12) and (13) and the DFT data for electrical and thermal conductivity are shown in (c) and (d), respectively. Between the isotherms and isochores, we interpolated the deviations cubically.

3.3. Lorenz Number

A well-known relation between the electrical and thermal conductivity is the Lorenz number L:

$$L = \frac{\lambda}{T\sigma}\left(\frac{e}{k_b}\right)^2. \tag{16}$$

For simple metals, i.e., for the degenerate electron gas, this relation yields a constant $L_0 = \pi^2/3$ (in units of $(e/k_b)^2$) known as the Wiedemann–Franz law. We calculate the Lorenz number to test the validity of this relation for the mixtures and conditions, as considered here. The results are shown in Figure 5. Pure hydrogen at high pressures shows no temperature dependence, typical for metallic systems, satisfying the Wiedemann–Franz law. However, below 100 GPa, we see deviations from the value L_0 in the molecular region with nonmetallic conductivity. For pure methane (star symbol), we also see deviations from L_0 at low pressure, irrespective of temperature. L_0 is only valid at higher pressures. At lower pressures, temperature has a greater effect on disrupting the bonds between carbon and hydrogen.

The temperature dependence is quite strong in the case of CH_4–H_2 mixtures. We see a significant deviation from the value of L_0 along the isotherm $T = 3000$ K. The calculated Lorenz number for $\mathcal{X}_{H_2} = 0.2008$ is lower than L_0 even at higher pressures. This effect could be tied to the stable clustering of carbon atoms, enhancing electron scattering with the mobile hydrogen atoms, which reduces the electronic thermal conductivity. With increasing temperature, this effect starts to disappear. At $T = 6000$ K, we find L_0 valid for all mixtures. Similarly, we encounter the same deviation for the $\mathcal{X}_{H_2} = 0.059$ and $\mathcal{X}_{H_2} = 0.116$, although not as strong as for the 1:2 mixture.

4. Discussion

For pure methane, we find the direct current (dc) value of electrical conductivity to be approximately 2.63 orders of magnitude larger than that of water at 4000 K and 2 g cm^{-3}

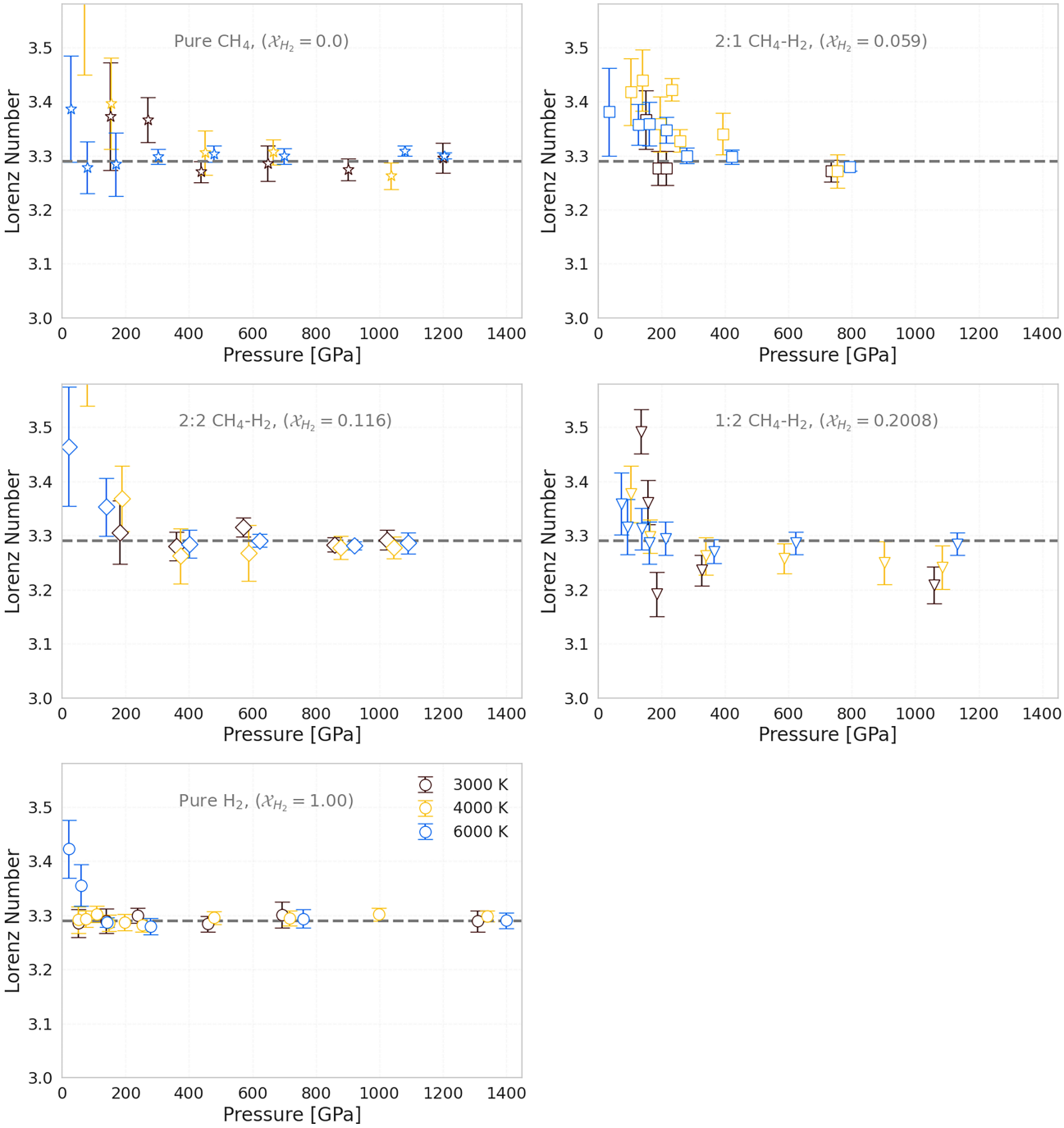


Figure 5. Lorenz number of pure components and methane–hydrogen mixtures as a function of pressure for different temperatures. Symbols ○, ▽, □, ◇, ⋆ denote pure hydrogen, mixtures of methane and hydrogen for different mass fraction $\mathcal{X}_{H_2}$, and pure methane, respectively. Brown, yellow, and blue color symbols denotes 3000, 4000, and 6000 K, respectively. The dashed gray line shows the limiting value of $L_0 = \pi^2/3$, known as the Wiedemann–Franz law.

(M. French et al. 2010); however, the difference in orders of magnitude drops to 1.4 at 6000 K for the same density. Adding hydrogen to pure methane affects the dc values of electrical properties, as hydrogen atoms upon dissociation act as charge carriers. Using Mott's criterion for the minimum metallic electrical conductivity (N. Mott 2004; W. Lorenzen et al. 2011) predicts the metallization in H–He mixtures to occur around 100 GPa at 4000 K for a hydrogen concentration of 66%. We find similar metallization pressures at the same temperature for a substantially lower hydrogen molecular mass fraction of 5% in a CH_4–H_2 mixture and a further drop in metallization pressure of about 20 GPa when the hydrogen concentration is increased to 20%. We also see a rise in the electrical and thermal conductivity values with increasing hydrogen concentration in the CH_4–H_2 mixtures; however, the dc conductivity values are significantly less than what we observe for pure hydrogen, despite the dominating number of hydrogen atoms. It can have a substantial effect on the modeling of planetary interiors as lower values of thermal conductivity may reduce the convective nature of heat

transport, which some models rely on. The situation becomes more complex when other high-pressure phases of carbon (such as diamond) and superionic phases of water and ammonia are taken into consideration. The nonmetallic nature of some of the phases can enhance phonon scattering, further reducing the thermal conductivity and the efficacy of convective heat transport. These key differences may mediate into variations in the age and radius of the planets, as changes in conductivity gradients may or may not allow for facilitating multipolar magnetic fields with shallower density stratification (L. D. Duarte et al. 2013; K. Soderlund & S. Stanley 2020) or allow more advanced interior models that incorporate the chemical properties of planetary matter.

5. Conclusion

We treated mixtures of methane and hydrogen for different molecular mass fractions of hydrogen and studied the effect on the EOS and transport properties. We focused on a temperature range of 3000–6000 K and hydrogen molecular mass fractions of 0, 0.059, 0.116, 0.2008, and 1.000. We present an analytical expression to model the thermal EOS obtained from DFT–MD simulations. Our model incorporates nonideal effect as a function of density and molecular mass fraction. We find our model to be applicable within the chosen temperature range. In Figure 2, we find a maximum deviation of 8.3% for the mixture with a molecular mass fraction of $\mathcal{X}_{H_2} = 0.116$. For the lowest and highest concentration of hydrogen in the mixtures, the deviations are below 5%. At higher density and temperature, the model produces pressure with a deviation of less than 2%, despite the transient nature of carbon bonds. Experiments reported the formation of diamonds above 2000 K, which we do not see in our simulation box and that could well be attributed to finite size effect. However, we can infer the diffusion coefficients (A. J. Roy et al. 2024) of carbon atoms. We suspect there may be demixing between carbon and hydrogen, driven by the metallic nature of hydrogen, and the two regions are separated from each other due to the large scattering cross section of carbon and polymeric bond formation of carbon. Calculations for the transport coefficients show a slight increment in electrical and thermal conductivity with an increase in the hydrogen molecular mass fraction. At higher pressure, the insulator–metal transition is driven by the delocalization of the wave function of hydrogen (D. Murayama et al. 2023) and the dissociation of methane. We use an analytical fit for all systems' electrical and thermal conductivity, and we find good agreement with the DFT–MD data, and we observe a maximum deviation at low pressure and temperature conditions for both the quantities. Our fit allows us to extrapolate to minimal pressure values, where DFT calculations become expensive.

Future DFT–MD simulations for relevant materials will advance the modeling of ice giants' interiors and dynamo models and aid experimental campaigns. Additionally, our findings will contribute to understanding planets like Uranus and Neptune and their properties, which will, in turn, highlight the ever-increasing number of Neptune-like and super-Earth planets.

Acknowledgments

We thank Nadine Nettelmann, Martin Preising, and Uwe Kleinschmidt for their helpful discussions. This work was supported by the North German Supercomputing Alliance (HRN), the ITMZ of the University of Rostock, and German Israel Foundation for Scientific Research and Development (GIF) within the Research grant No. I-1486-303.7/2019. We also thank Helmholtz–Zentrum Dresden–Rossendorf e.V. (HZDR) for support.

Appendix

In Figure 6 we plot the EOS of pure and the mixtures for isotherms $T=$ 3000 K and 6000 K. Figure 7 shows the deviation between DFT–MD EOS and LMA for molecular hydrogen concentration of 5.9% and 20%, respectively. In Figure 8 we show the dc values of thermal conductivity, the influence of hydrogen molecules and the models as given in Equations (14) and (15) and finally, Figure 9 shows the deviation of fitted equations according to Equations (12) and (13) from the simulation data, with Tables 3 and 4 holding the values of fitted parameters.

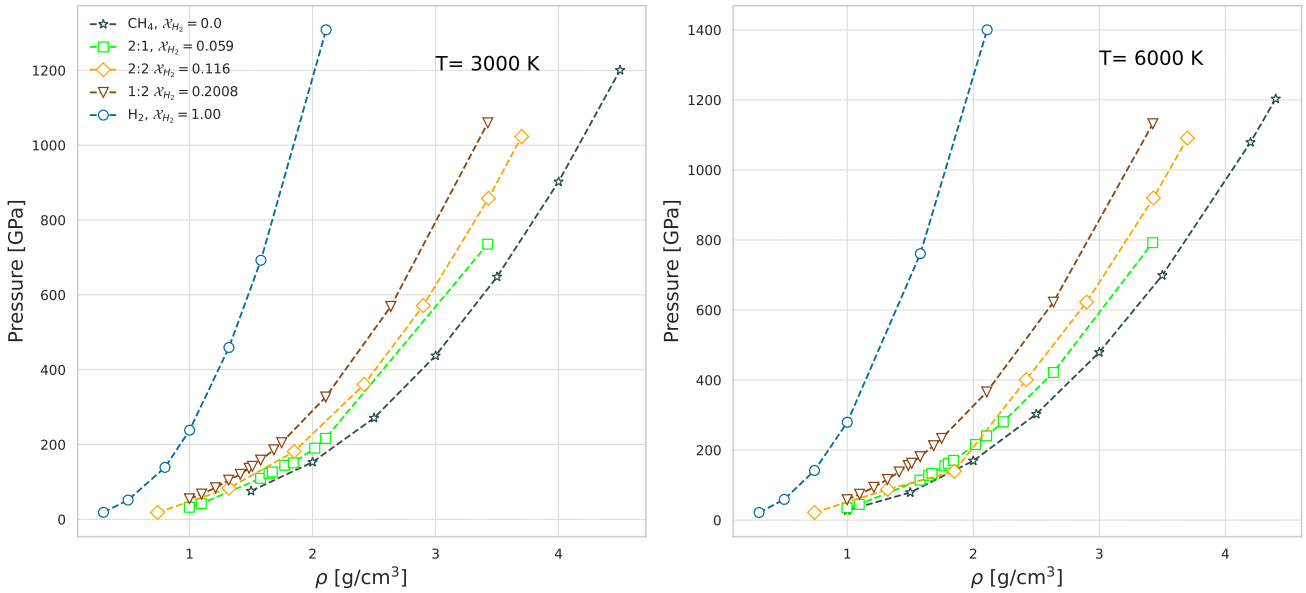


Figure 6. EOS isotherms of $T = 3000$ K and 6000 K as a function of density for all the concerned systems. Symbols ○, ▽, □, ◇, ⋆ denote pure hydrogen, mixtures of methane and hydrogen for different mass fraction $\mathcal{X}_{H_2}$, and pure methane, respectively.

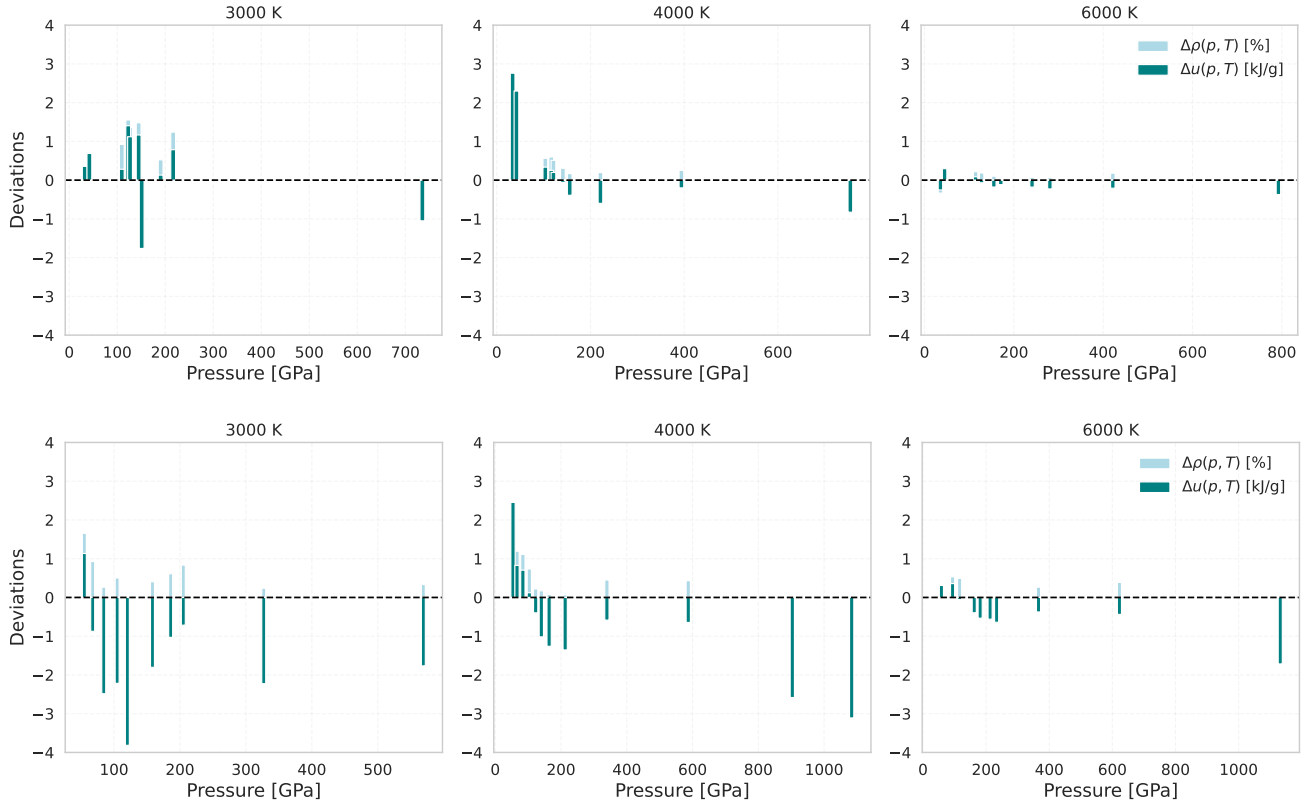


Figure 7. Deviation of densities (light blue; in percent) and specific internal energy (kJ g^{-1}; teal) from the real mixture having a molecular mass fraction of $\mathcal{X}_{H_2} = 0.059$ (top) and 0.2008 (bottom) according to Equations (10) and (11), respectively.

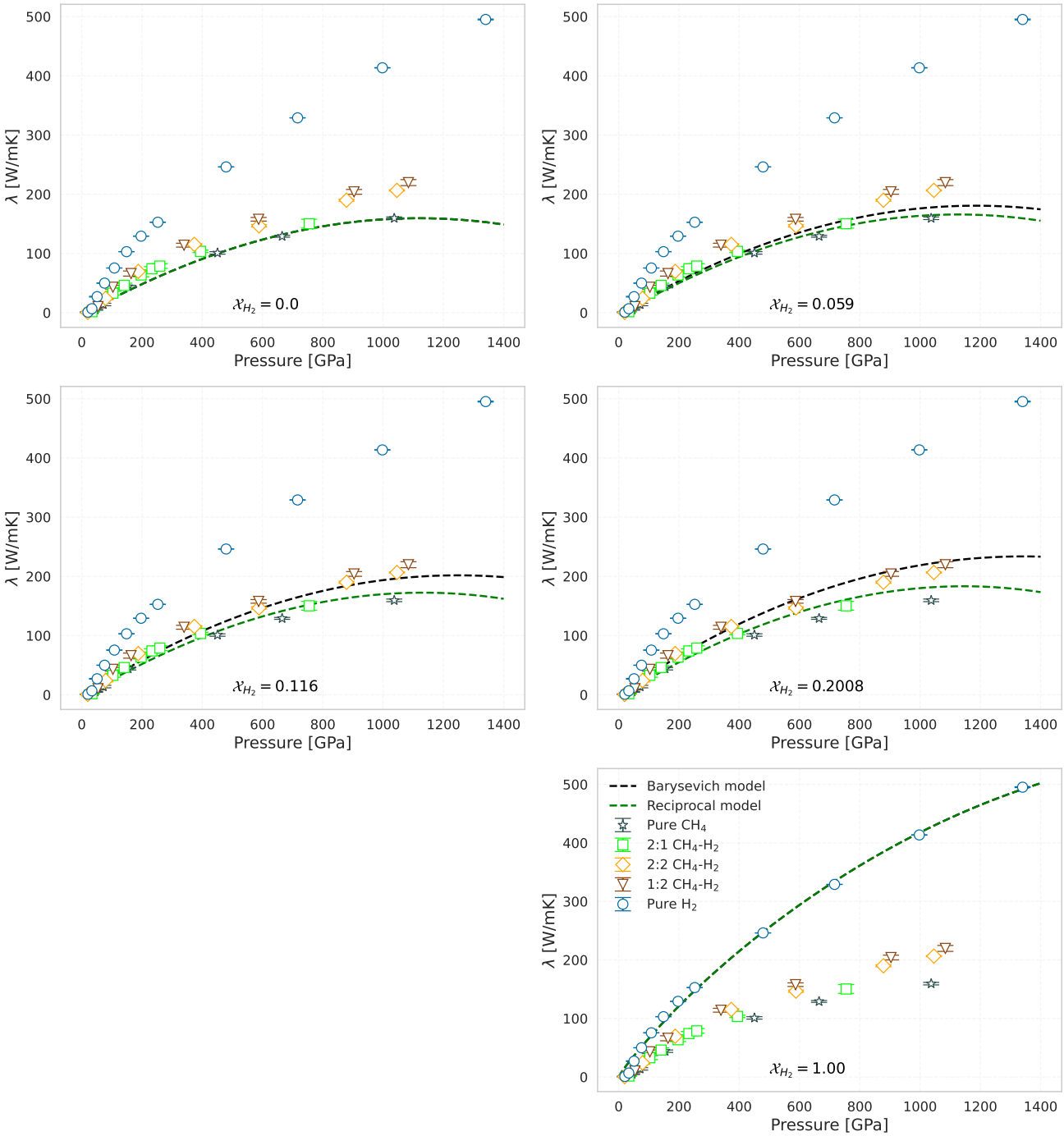
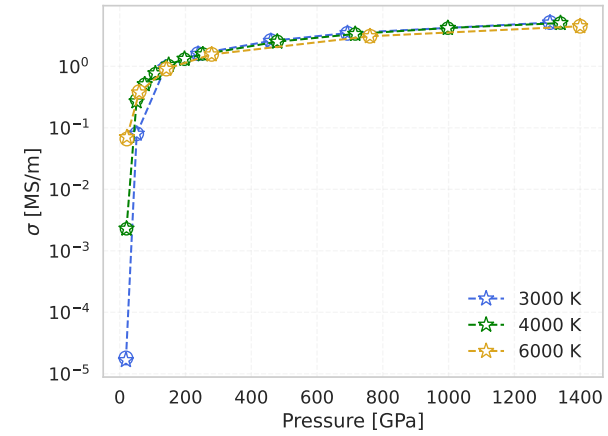
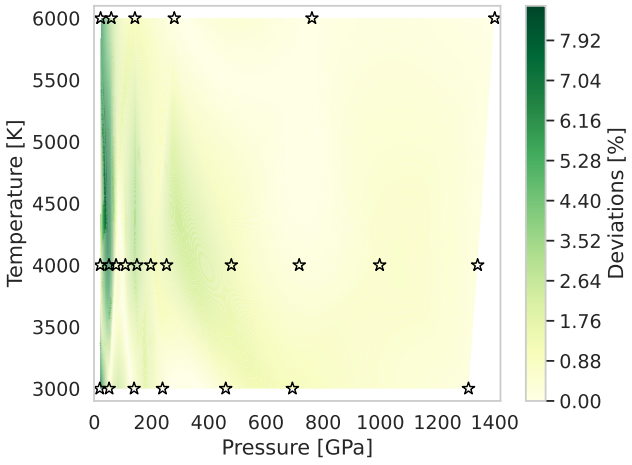


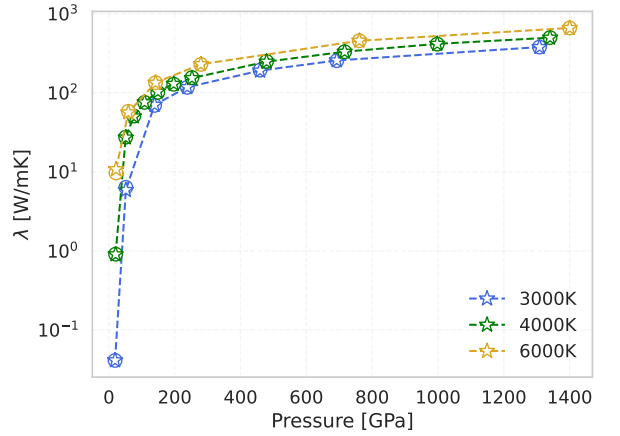
Figure 8. Thermal conductivity mixing models as function of pressure along an isotherm of 4000 K: Black broken lines: (i) Barysevich model Equation (14) ($n = -2.8$). Green broken lines: (ii) reciprocal mixing Equation (15). DFT–MD data are color-coded symbols, circles denote pure H_2, and stars denote CH_4. Diamonds, triangles, and squares denote the various mixed systems.



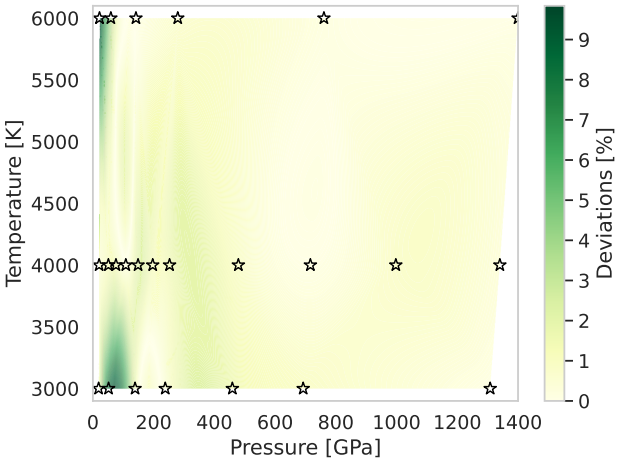
(a) Electrical conductivity



(b) Deviation in electrical conductivity



(c) Thermal conductivity



(d) Deviation in thermal conductivity

Figure 9. (a), (b) Electrical and thermal conductivity of pure H_2 as a function of pressure along the isotherms. The hollow circles represent the points obtained from the fit Equations (12) and (13), and hollow stars are DFT simulation data using Equation (2). The deviations between the predicted values of the fits using Equations (12) and (13) vs. DFT data for electrical and thermal conductivity are shown in (c) and (d), respectively. Between the isotherms and isochores, we interpolated the deviations cubically.

Table 3
Parameters Obtained from Fitting the Analytical Equation for Electrical Conductivity Equations (12) and (13)

	H_2			CH_4		
Parameters [Units]/ T [K]	3000	4000	6000	3000	4000	6000
$A\left[\frac{\mathrm{MS}}{\mathrm{m}\cdot(\mathrm{GPa})^m}\right]$	0.071980	4.8654×10^{-8}	−0.019929	0.2336	0.033782	0.03241
m	0.60	2.00	0.50	0.50	0.50	0.50
$B\,[(\mathrm{GPa})^n]$	2025.2	−3478.6	6.062×10^5	2.6302×10^4	3.3782×10^3	2.170×10^3
n	1.85	2.00	2.00	2.00	2.00	2.00
C	−0.167	0.102	0.0464	−0.128	0.0142	0.0307
d	0.47415	0.55615	0.6540	1.000	0.5482	0.4498
$E\left[\frac{\mathrm{MS}}{\mathrm{m}}\right]^{\frac{1}{k}}$	−0.13283	−0.90996	−0.6557	0.70779	−0.68997	-3.740×10^{-3}
k	5.00	5.00	3.00	8.00	7.00	7.00
j	50.00	⋯	⋯	80.00	⋯	⋯

Note. m, n, d, k are dimensionless quantities.

Table 4
Parameters Obtained from Fitting the Analytical Equation for Thermal Conductivity Equation (12)

	H_2			CH_4		
Parameters [Units]/ T [K]	3000	4000	6000	3000	4000	6000
$A\left[\frac{W}{m\cdot K\cdot(GPa)^m}\right]$	6.733×10^{-6}	2.1067	-2.324×10^{-5}	1.4559	−0.010493	−0.01819
m	2.00	0.90	2.00	0.900	1.80	1.20
B [(GPa)^n]	-3.4034×10^{3}	1.1612×10^{3}	8.773×10^{4}	1.3833×10^{4}	1.0211×10^{-4}	-2.051×10^{3}
n	2.00	2.00	2.00	2.00	−2.00	2.00
$C\left[\frac{W}{m\cdot K\cdot(GPa)^d}\right]$	20.5	−0.0487	8.27	−1.45	11.2	4.72
d	0.43756	1.0427	0.6217	0.89033	0.41380	0.6128
$E\left[\frac{W}{m\cdot K}\right]^{\frac{1}{k}}$	−2.5557	−1.7889	−2.155	1.6748	−38.199	0.01312
k	5.00	4.00	5.00	8.00	1.00	8.00

Note. m, n, d, k are dimensionless quantities.

ORCID iDs

Argha Jyoti Roy https://orcid.org/0009-0006-4798-650X
Mandy Bethkenhagen https://orcid.org/0000-0002-1838-2129
Armin Bergermann https://orcid.org/0000-0002-2849-1791
Ronald Redmer https://orcid.org/0000-0003-3440-863X

References

Baldereschi, A. 1973, PhRvB, 7, 5212
Barysevich, A., & Cherkas, S. 2011, PhPl, 18, 052703
Benedetti, L. R., Nguyen, J. H., Caldwell, W. A., et al. 1999, Sci, 286, 100
Bergermann, A., Kleindienst, L., & Redmer, R. 2024, JChPh, 161, 234303
Bethkenhagen, M., French, M., & Redmer, R. 2013, JChPh, 138, 234504
Bethkenhagen, M., Meyer, E. R., Hamel, S., et al. 2017, ApJ, 848, 67
Blöchl, P. E. 1994, PhRvB, 50, 17953
Bolton, S. J., Lunine, J., Stevenson, D., et al. 2017, SSRv, 213, 5
Cheng, B., Hamel, S., & Bethkenhagen, M. 2023, NatCo, 14, 1104
Danel, J.-F., & Kazandjian, L. 2015, PhRvE, 91, 013103
Demarcus, W. C. 1958, AJ, 63, 2
Dougherty, M., Esposito, L., & Krimigis, S. M. 2009, Saturn from Cassini-Huygens (Berlin: Springer)
Duarte, L. D., Gastine, T., & Wicht, J. 2013, PEPI, 222, 22
Fortney, J. J., Ikoma, M., Nettelmann, N., Guillot, T., & Marley, M. S. 2011, ApJ, 729, 32
French, M., Becker, A., Lorenzen, W., et al. 2012, ApJS, 202, 5
French, M., Mattsson, T. R., Nettelmann, N., & Redmer, R. 2009, PhRvB, 79, 054107
French, M., Mattsson, T. R., & Redmer, R. 2010, PhRvB, 82, 174108
French, M., Röpke, G., Schörner, M., et al. 2022, PhRvE, 105, 065204
Frost, M., McWilliams, R. S., Bykova, E., et al. 2024, NatAs, 8, 174
Greenwood, D. 1958, PPS, 71, 585
Guillot, T. 1999, Sci, 286, 72
Guillot, T., Gautier, D., & Schubert, G. 2015, Treatise on Geophysics (2nd ed.; Amsterdam: Elsevier)
Hafner, J. 2008, JCoCh, 29, 2044
He, Z., Rödel, M., Lütgert, J., et al. 2022, SciA, 8, eabo0617
Heyd, J., & Scuseria, G. E. 2004a, JChPh, 121, 1187
Heyd, J., & Scuseria, G. E. 2004b, JChPh, 120, 7274
Heyd, J., Scuseria, G. E., & Ernzerhof, M. 2003, JChPh, 118, 8207
Hohenberg, P., & Kohn, W. 1964, PhRv, 136, B864
Holst, B., French, M., & Redmer, R. 2011, PhRvB, 83, 235120
Holst, B., Redmer, R., & Desjarlais, M. P. 2008, PhRvB, 77, 184201
Hoover, W. G. 1985, PhRvA, 31, 1695
Hu, R., Li, Y., Wang, C., Hu, Y., et al. 2023, PhRvB, 107, 174108
Hubbard, W. 1978, Icar, 35, 177
Hubbard, W. B., & MacFarlane, J. J. 1980, JGRB, 85, 225
Irwin, P. G., Teanby, N. A., Fletcher, L. N., et al. 2022, JGRE, 127, e2022JE007189
Johnson, W., Guet, C., & Bertsch, G. 2006, JQSRT, 99, 327
Knyazev, D., & Levashov, P. 2013, ComMS, 79, 817
Kraus, D., Vorberger, J., Pak, A., et al. 2017, NatAs, 1, 606
Kresse, G. 1996, PhRvB, 54, 11169
Kresse, G., & Furthmüller, J. 1996, ComMS, 6, 15
Kresse, G., & Hafner, J. 1993, PhRvB, 47, 558
Kresse, G., & Hafner, J. 1994, PhRvB, 49, 14251
Kresse, G., & Joubert, D. 1999, PhRvB, 59, 1758
Kubo, R. 1957, JPSJ, 12, 570
Kuchiev, M. Y., & Johnson, W. R. 2008, PhRvE, 78, 026401
Linder, E. F., Mordasini, C., Mollière, P., et al. 2019, A&A, 623, A85
Lorenzen, W., Holst, B., & Redmer, R. 2010, PhRvB, 82, 195107
Lorenzen, W., Holst, B., & Redmer, R. 2011, PhRvB, 84, 235109
Mandt, K. E. 2023, Sci, 379, 640
Mermin, N. D. 1965, PhRv, 137, A1441
Mott, N. 2004, Metal-Insulator Transitions (2nd ed.; Boca Raton, FL: CRC Press)
Murayama, D., Ohmura, S., Kodama, R., & Ozaki, N. 2023, JAP, 134, 095902
National Academies of Sciences, Engineering, and Medicine 2022, Origins, Worlds, and Life: A Decadal Strategy for Planetary Science and Astrobiology 2023–2032 (Washington, DC: The National Academies Press)
Nettelmann, N., Helled, R., Fortney, J., & Redmer, R. 2013, P&SS, 77, 143
Peebles, P. J. E. 1964, ApJ, 140, 328
Perdew, J. P., Burke, K., & Ernzerhof, M. 1996, PhRvL, 77, 3865
Podolak, M., & Helled, R. 2012, ApJL, 759, L32
Ranieri, U., Conway, L. J., Donnelly, M.-E., et al. 2022, PhRvL, 128, 215702
Redlich, O., & Kister, A. T. 1948, Ind. Eng. Chem. Res., 40, 345
Redmer, R., Mattsson, T. R., Nettelmann, N., & French, M. 2011, Icar, 211, 798
Ross, M. 1981, Natur, 292, 435
Roy, A. J., Bergermann, A., Bethkenhagen, M., & Redmer, R. 2024, PCCP, 26, 14374
Scheibe, L., Nettelmann, N., & Redmer, R. 2019, A&A, 632, A70
Sherman, B. L., Wilson, H. F., Weeraratne, D., & Militzer, B. 2012, PhRvB, 86, 224113
Shuichi, N. 1991, PThPS, 103, 1
Soderlund, K., & Stanley, S. 2020, RSPTA, 378, 20190479
Soubiran, F., & Militzer, B. 2015, ApJ, 806, 228
Soubiran, F., & Militzer, B. 2016, ApJ, 829, 14
Stanley, S., & Bloxham, J. 2004, Natur, 428, 151
Stanley, S., & Bloxham, J. 2006, Icar, 184, 556
Starrett, C., Clérouin, J., Recoules, V., et al. 2012, PhPl, 19, 102709
Starrett, C., Shaffer, N., Saumon, D., et al. 2020, HEDP, 36, 100752
Stevenson, D. J., et al. 1982, AREPS, 10, 257
Tabak, G., Rygg, J., Millot, M., et al. 2024, PhRvB, 109, 064102
Tamblyn, I., & Bonev, S. A. 2010, PhRvL, 104, 065702
Weinert, M., & Davenport, J. 1992, PhRvB, 45, 13709
Wentzcovitch, R. M., Martins, J. L., & Allen, P. B. 1992, PhRvB, 45, 11372
White, A. J., Craven, G. T., Sharma, V., & Collins, L. A. 2024, PhPl, 31, 042706
Zaghoo, M., Salamat, A., & Silvera, I. F. 2016, PhRvB, 93, 155128

6.3 Stochastic density functional theory combined with Langevin dynamics for warm dense matter

- **R. E. Hadad:** Preparation of the manuscript, conducting DFT-MD simulation, data analysis and interpretation of the results.
- **A. J. Roy:** Preparation of the manuscript, interpretation of the results.
- **E. Rabani:** Preparation of the manuscript, interpretation of the results.
- **R. Redmer:** Supervision of the project, preparation of the manuscript, interpretation of the results
- **R. Baer:** Supervision of the project, preparation of the manuscript, interpretation of the results

Stochastic density functional theory combined with Langevin dynamics for warm dense matter

Rebecca Efrat Hadad
Fritz Haber Research Center for Molecular Dynamics, Institute of Chemistry, The Hebrew University of Jerusalem, Jerusalem 91904, Israel

Argha Roy
Institute of Physics, University of Rostock, 18051 Rostock, Germany

Eran Rabani
Department of Chemistry, University of California, Berkeley, California 94720, USA; Materials Sciences Division, Lawrence Berkeley National Laboratory, Berkeley, California 94720, USA; and The Raymond and Beverly Sackler Center of Computational Molecular and Materials Science, Tel Aviv University, Tel Aviv 69978, Israel

Ronald Redmer
Institute of Physics, University of Rostock, 18051 Rostock, Germany

Roi Baer
Fritz Haber Research Center for Molecular Dynamics, Institute of Chemistry, The Hebrew University of Jerusalem, Jerusalem 91904, Israel

(Received 24 January 2024; accepted 17 May 2024; published 11 June 2024)

This study overviews and extends a recently developed stochastic finite-temperature Kohn-Sham density functional theory to study warm dense matter using Langevin dynamics, specifically under periodic boundary conditions. The method's algorithmic complexity exhibits nearly linear scaling with system size and is inversely proportional to the temperature. Additionally, a linear-scaling stochastic approach is introduced to assess the Kubo-Greenwood conductivity, demonstrating exceptional stability for dc conductivity. Utilizing the developed tools, we investigate the equation of state, radial distribution, and electronic conductivity of hydrogen at a temperature of 30 000 K. As for the radial distribution functions, we reveal a transition of hydrogen from gaslike to liquidlike behavior as its density exceeds 4 g/cm^3. As for the electronic conductivity as a function of the density, we identified a remarkable isosbestic point at frequencies around 7 eV, which may be an additional signature of a gas-liquid transition in hydrogen at 30 000 K.

DOI: 10.1103/PhysRevE.109.065304

I. INTRODUCTION

Warm dense matter (WDM) exists in the interior of planets [1–10] and in brown dwarf [11–15] and white dwarf stars [16,17]. In inertial and fusion systems [18,19], WDM is generated by subjecting materials to high-energy lasers [20]. Despite its significance, exploring the diverse forms and compositions of WDM poses a formidable challenge due to experimental complexities associated with preparing and sustaining materials under extreme conditions [5,21,22]. Consequently, computational methods have become indispensable for determining the equations of state as well as the chemical and physical properties of different systems.

Among these methods are *ab initio* molecular-dynamics (AIMD) calculations [23–27], which rely on an "adiabatic" approximation. This approximation assumes that the quantum mechanical electrons reach thermal equilibrium under the applied temperature, electronic chemical potential, and Coulomb potentials corresponding to the instantaneous positions of the atomic nuclei. The latter then undergo classical motion under the conservative force derived from the electronic free energy, effectively acting as a potential of mean force (see, e.g., Ref. [28]). The observables can be determined by averaging over a long adiabatic molecular-dynamics (MD) trajectory.

The adiabatic and classical approximations behind AIMD have their limitations. There is evidence suggesting that a classical approximation may lack sufficient accuracy, particularly for temperatures below 1000 K and under high pressures [29,30]. Moreover, nonadiabatic effects, though often disregarded, as done here, have not been thoroughly explored in the context of AIMD in WDM. Previous studies concerning nonadiabatic dynamics on metal surfaces introduce two distinct types of electron-nucleus forces in addition to the adiabatic one [31–34]. The first type manifests as rapid fluctuations resembling a stochastic process, while the second type involves dissipation, simulated as a friction force with a friction constant determined by the electronic structure. Since the molecular dynamics treats atomic nuclei as classical, the Langevin dynamics approach [28,35] can be used to handle

 ©2024 American Physical Society

nonadiabatic effects, utilizing fluctuating-dissipating forces to impose the electronic temperature as the average value of the atomic nuclei kinetic energy in a canonical ensemble.

AIMD simulations for WDM need to consider both quantum fermionic degeneracy and strong Coulomb interactions [36]. The Kohn-Sham density functional theory (KS-DFT), which has proven highly successful as an *ab initio* theory for elucidating the structure of molecules and materials at zero temperature [25,37–45], fulfills these requirements and has been extended to finite temperatures, and it has become a widely employed method for theoretical studies of WDM [46–51]. However, applying KS-DFT to WDM requires calculating and storing an increasing number of Kohn-Sham eigenstates as the temperature rises. Consequently, for electronic temperatures exceeding 100 000 K, other approaches, such as the extended KS method [52,53] or "orbital-free DFT," which include finite-temperature orbital free functionals [54–59] and method development [60–66], are preferred. Another emerging approach involves utilizing machine learning to generate potential-energy surfaces and interatomic forces based on KS-DFT and variational quantum Monte Carlo data sets. These learned models can then be employed in molecular-dynamics calculations to predict material properties with reduced computational costs [67–71].

A linear scaling DFT procedure holds significant promise for investigating WDM, whether applied directly in AIMD or for generating training data sets for machine learning. This can be realized through stochastic DFT, as demonstrated by various authors in recent works [72–78]. In this paper, we elaborate on additional advancements in stochastic plane-wave Kohn-Sham density functional theory, integrating it with Langevin dynamics and introducing a novel approach for computing electronic conductivity. We thoroughly assess and benchmark the method, showcasing its practical application by conducting a detailed study of hydrogen at 30 000 K.

II. STOCHASTIC FINITE-TEMPERATURE KOHN-SHAM DFT

A. Finite-temperature Kohn-Sham scheme

The combination of finite-temperature density functional theory [46,79] and the Kohn-Sham procedure (FT-KS-DFT) [80] greatly simplifies the formidable problem of treating interacting electrons under the influence of a heat and electron bath. Under the FT-KS-DFT formalism, we need only study a system of noninteracting electrons in a one-body potential, which includes exchange-correlation contributions. As a result of the exchange-correlation potential, the noninteracting electron density is identical to that of the interacting system, and the grand potential of the interacting electron system can be expressed using the noninteracting grand potential together with exchange-correlation free-energy corrections. As the finite temperature diminishes towards zero, the FT-KS-DFT converges into the zero-temperature KS-DFT, with corresponding exchange-correlation contributions, and the free energy converges to zero-temperature ground-state energy [81].

To study infinite systems, it is beneficial to impose periodic boundary conditions within the simulation cell. The single electron wave functions of the noninteracting system are expressed as a linear combination of the plane-wave basis $e^{i\boldsymbol{G}\cdot\boldsymbol{r}}$:

$$\psi(\boldsymbol{r}) = \sum_{\boldsymbol{G}} \tilde{c}_{\boldsymbol{G}} \frac{e^{i\boldsymbol{G}\cdot\boldsymbol{r}}}{\sqrt{\Omega}}, \tag{1}$$

where $\boldsymbol{G} = \frac{2\pi}{L}(m_x, m_y, m_z)$ is the simulation cell-commensurate wave vector and m_i integers. The wave-vector parameter $G_{\rm cut}$ determines the size of the plane-wave basis by requiring that $\|\boldsymbol{G}\|_2 \leqslant G_{\rm cut}$. This cutoff identifies a subspace of dimension $D = [\frac{3\pi}{4}(\frac{L}{2\pi}G_{\rm cut})^3]$ of the simulation cell's periodic functions, which is mapped by Eq. (1) onto the complex vector space of D-tuples $\mathbb{C}^D = \{\tilde{c}_{\boldsymbol{G}}\}_{\|\boldsymbol{G}\|_2 \leqslant G_{\rm cut}}$. The basis truncation error can be systematically mitigated by increasing $G_{\rm cut}$, or, equivalently, the cutoff energy $E_{\rm cut} = \frac{\hbar^2 G_{\rm cut}^2}{2m_e}$. Variational treatment of the finite-temperature Kohn-Sham equations within the subspace leads to a set of algebraic eigenvalue equations,

$$\mathcal{H}\tilde{c}^{(j)} = \varepsilon_j \tilde{c}^{(j)}, \quad j = 1, 2, \ldots, D, \tag{2}$$

where $\mathcal{H}$ is the Kohn-Sham Hamiltonian (for more details on the representation and the operators, see, for example, Ref. [38]), and ε_j and $\tilde{c}^{(j)}$ are its (real) eigenvalues and (complex) eigenvectors.

The electrons are in a grand-canonical mixed state with temperature parameter $\beta = (k_B T)^{-1}$, where k_B is Boltzmann's constant, and chemical potential μ. The occupation of each single-particle energy level ε is given by the Fermi-Dirac function $p_{\beta\mu}(\varepsilon) \equiv (1 + e^{\beta(\varepsilon-\mu)})^{-1}$. Correspondingly, the electron density can be expressed as a sum of level densities,

$$n(\boldsymbol{r}) = 2 \times \sum_j p_{\beta\mu}(\varepsilon_j)|\varphi_j(\boldsymbol{r})|^2, \tag{3}$$

where

$$\varphi_j(\boldsymbol{r}) = \sum_{\boldsymbol{G}} \tilde{c}_{\boldsymbol{G}}^{(j)} \frac{e^{i\boldsymbol{G}\cdot\boldsymbol{r}}}{\sqrt{\Omega}} \tag{4}$$

are the [normalized, so that $\int_\Omega |\varphi_j(\boldsymbol{r})|^2 d\boldsymbol{r} = 1$] Kohn-Sham eigenstates in real space. The grand potential of the electrons is then given by [82]

$$\Phi_{\beta\mu}[n] \equiv E_{\rm orb} - E_H[n] + \Phi_{\beta\mu,{\rm xc}}[n] - \int v_{\beta\mu,{\rm xc}}(\boldsymbol{r}) n(\boldsymbol{r}) d\boldsymbol{r} - \beta^{-1} S_s[n] - \mu \int n(\boldsymbol{r}) d\boldsymbol{r}, \tag{5}$$

where

$$E_{\rm orb} \equiv 2 \times \sum_j p_{\beta\mu}^j \varepsilon_j \tag{6}$$

is the orbital energy, $p_{\beta\mu}^j = p_{\beta\mu}(\varepsilon_j)$, $E_H[n]$ is the Hartree energy, and $\Phi_{\beta\mu,{\rm xc}}[n]$ is the $\beta\mu$-dependent approximate exchange-correlation free-energy functional of the density, which includes entropy corrections, and $v_{\beta\mu,{\rm xc}}(\boldsymbol{r}) = \frac{\delta\Phi_{\beta\mu,{\rm xc}}}{\delta n(\boldsymbol{r})}$ is the corresponding exchange-correlation potential. Temperature-dependent exchange-correlation free-energy density functionals which have been developed recently [83–89] show that for the temperature ranges and densities

considered in this paper, one can safely use the approximation $\Phi_{\beta\mu,\mathrm{xc}}[n] \approx E_{\mathrm{xc}}^{\mathrm{LDA}}[n]$, where $E_{\mathrm{xc}}^{\mathrm{LDA}}[n]$ is the zero-temperature local-density approximation (LDA, [80]) for the exchange correlation energy, and correspondingly $v_{\beta\mu\mathrm{xc}}(\boldsymbol{r})$ is approximated as the zero-temperature LDA exchange-correlation potential $v_{\mathrm{xc}}^{\mathrm{LDA}}(\boldsymbol{r}) = \frac{\delta E_{\mathrm{xc}}^{\mathrm{LDA}}}{\delta n(\boldsymbol{r})}$. Finally, S_s in Eq. (5) is the entropy of noninteracting electrons at density $n(\boldsymbol{r})$ expressed as

$$S_s = -2 \times k_B \sum_j \left[p_{\beta\mu}^j \log p_{\beta\mu}^j + \bar{p}_{\beta\mu}^j \log \bar{p}_{\beta\mu}^j \right], \tag{7}$$

where, in short, $\bar{p}_{\beta\mu}^j \equiv 1 - p_{\beta\mu}^j$. In this Kohn-Sham procedure, we find the density $n(\boldsymbol{r})$ that minimizes the grand potential $\Phi_{\beta\mu}$. The number of electrons is $\tilde{N}_e(\mu) = (\frac{\partial \Phi_{\beta\mu}}{\partial \mu})_\beta = 2 \times \sum_j p_{\beta\mu}^j$.

The ξ-component ($\xi = 0, 1, 2$ indicates, respectively, x, y, z) of the force on an atomic nucleus $A (A = 0, \ldots, N_n - 1$, where N_n is the number of atomic nuclei in the simulation cell) is equal to the corresponding derivative of the grand potential, $F^i = -\frac{\partial \Phi_{\beta\mu}}{\partial R_i} + F_i^{\mathrm{NN}}$, where $i \equiv (3A + \xi)$ is the force index, and F_i^{NN} is the sum of forces exerted by all other atomic nuclei. This force is an average force over all ground and excited electronic states of all possible charge states of the system.

An alternative to working in the grand-canonical ensemble, where μ is given, is to impose a fixed average number of electrons N_e and then tune μ accordingly. Such an ensemble is more natural for small, finite simulation cells. In this ensemble, the chemical potential becomes a function of the imposed value of N_e, denoted $\tilde{\mu}(N_e)$, defined implicitly by solving the equation

$$N_e = 2 \times \sum_j p_{\beta\tilde{\mu}(N_e)}^j. \tag{8}$$

In this ensemble, we find the density $n(\boldsymbol{r})$ that minimizes the Helmholtz free energy $\mathcal{F}_{\beta N_e} = U - \beta^{-1} S_s$ and the force is its derivative, $F_i = -\frac{\partial \mathcal{F}_{\beta N_e}}{\partial R_i} + F_i^{\mathrm{NN}}$. Once again, this force is an average over all ground and excited electronic states of all possible charge states of the system.

Regardless of the ensemble used, the electronic force component i is obtained from the electron density and the corresponding derivative of the electron-nucleus force potential:

$$F_i = -\int n(\boldsymbol{r}) \frac{\partial}{\partial R_i} v_{\mathrm{eN}}(\boldsymbol{r}) d\boldsymbol{r} + F_i^{\mathrm{NN}},$$

and when nonlocal pseudopotentials are employed, i.e., $\hat{v}_{\mathrm{eN}} = v_{\mathrm{loc}}(\boldsymbol{r}) + \hat{v}_{\mathrm{nl}}$, the following generalization needs to be used (now in vector notation):

$$\boldsymbol{F} = -2 \times \sum_j p_{\beta\mu}^j \langle \varphi_j | \nabla \hat{v}_{\mathrm{eN}} | \varphi_j \rangle + \boldsymbol{F}^{\mathrm{NN}}. \tag{9}$$

B. The stochastic density functional approach

Stochastic density functional theory [72] is based on the concept of random wave functions,

$$\eta(\boldsymbol{r}) \equiv \sum_{\boldsymbol{G}} \tilde{\eta}^{\boldsymbol{G}} \frac{e^{i\boldsymbol{G}\cdot\boldsymbol{r}}}{\sqrt{\Omega}}, \tag{10}$$

in which the random coefficients $\tilde{\eta}^{\boldsymbol{G}}$ are given, in vector notation, by operating with the square-root Fermi-Dirac operator $\sqrt{p_{\beta\mu}(\mathcal{H})}$ on a random vector:

$$\tilde{\eta} \equiv \sqrt{p_{\beta\mu}(\mathcal{H})} \tilde{\chi}, \tag{11}$$

where $\tilde{\chi}$ is a random vector with components $\tilde{\chi}^{\boldsymbol{G}} \equiv e^{i\theta_{\boldsymbol{G}}}$, where $\theta_{\boldsymbol{G}}$ are independent random phases (between 0 and 2π). It is straightforward to check that

$$\mathrm{E}[\tilde{\chi}^{\boldsymbol{G}'} \tilde{\chi}^{\boldsymbol{G}*}] = \delta_{\boldsymbol{G}'\boldsymbol{G}}. \tag{12}$$

Here, the symbol $\mathrm{E}[r]$ is the expected value of a random variable r. The random variable $\tilde{\eta}^{\boldsymbol{G}'} \tilde{\eta}^{\boldsymbol{G}*}$ is an unbiased estimator of the KS density matrix in G-space, relying on the following exact identity: $[p_{\beta\mu}(\mathcal{H})]_{\boldsymbol{G}'\boldsymbol{G}} = \mathrm{E}[\tilde{\eta}^{\boldsymbol{G}'} \tilde{\eta}^{\boldsymbol{G}*}]$. This relation is proved by plugging Eq. (11) on the right-hand side and using Eq. (12). Similarly, sampling $\eta(\boldsymbol{r})\eta(\boldsymbol{r}')^*$, where $\eta(\boldsymbol{r})$ is defined in Eq. (10), provides an estimate for the KS density matrix $\rho(\boldsymbol{r}, \boldsymbol{r}') = 2 \times \sum_j p_{\beta\mu}(\varepsilon_j) \varphi_j(\boldsymbol{r}) \varphi_j(\boldsymbol{r}')^*$. From this, $|\eta(\boldsymbol{r})|^2$ is an unbiased estimator for the electron density $n(\boldsymbol{r})$, relying on the exact identity:

$$n(\boldsymbol{r}) = 2 \times \mathrm{E}[|\eta(\boldsymbol{r})|^2]. \tag{13}$$

This expression is the essence of stochastic KS-DFT: it replaces the *calculation* of the electron density $n(\boldsymbol{r})$ [Eq. (3)], which requires the KS-DFT eigenstates and eigenvalues [Eq. (2)] by a statistical sampling of the random variable $|\eta(\boldsymbol{r})|^2$.

The fact that the expected value of the absolute square of the random variable $\eta(\boldsymbol{r})$ gives the density means that we can now use sampling methods to obtain actual estimates of the density. If we produce a sample of I independent random vectors $\tilde{\chi}_i$ ($i = 1, \ldots, I$), and from them, using Eqs. (10) and (11), obtain samples of $\eta_i(\boldsymbol{r})$, then the density can be estimated as an average

$$n(\boldsymbol{r}) = 2 \times \frac{1}{I} \sum_{i=1}^{I} [|\eta_i(\boldsymbol{r})|^2].$$

This sampling procedure is straightforward to parallelize using a distributed memory model, for example, the message-passing-interface library. Observables such as the forces on atomic nuclei can be expressed as stochastic traces as well (see Sec. III A). From statistics, the fluctuations in the density or forces are proportional to the inverse square root of the sample size. For the calculations shown below, we used a sample of $I = 40$ stochastic orbitals (irrespective of the system size).

C. Chebyshev expansion methods

1. The essential Chebyshev expansion

We now describe a recipe for performing calculations of the type shown in Eq. (11), i.e., operating with a function of the Hamiltonian, namely $z(\mathcal{H})$ on some given a vector χ: $|\zeta\rangle = z(\mathcal{H})|\chi\rangle$. For this, we use the Chebyshev expansion [90] of length N_C, $\zeta^{\boldsymbol{G}} = \sum_{n=0}^{N_C-1} Z^{(n)} \chi_n^{\boldsymbol{G}}$, which we write in ket-form as

$$|\zeta\rangle = \sum_{n=0}^{N_C-1} Z^{(n)} |\chi_n\rangle. \tag{14}$$

The Chebyshev coefficients are defined by

$$Z^{(n)} = \frac{2}{N_C} e^{i\frac{\pi}{N_C}n} \tilde{z}^{(n)},$$

where the series $\{\tilde{z}^{(n)}\}_{n=0}^{N_C-1}$ is the discrete Fourier transform of $\{z[\bar{E} + \Delta E \times \cos(\frac{l+\frac{1}{2}}{N_C}\pi)]\}_{l=0}^{N_C-1}$. In the last expression, $\bar{E} = (E_{\max} + E_{\min})/2$, $\Delta E = (E_{\max} - E_{\min})/2$, and $E_{\min}$ ($E_{\max}$) is a lower (upper) bound estimate to the smallest (largest) eigenvalue of $\mathcal{H}$.

The expansion length N_C is chosen to be sufficiently large so that the $|Z^{(n)}|$ are all smaller than a threshold value 10^{-d} (typically $d = 7$ or 8) for $n > N_C$. An estimate for the Chebyshev length is the following expression:

$$N_C \approx \frac{3d}{4} \times \beta \times \Delta E. \tag{15}$$

The Chebyshev vectors $|\chi_n\rangle$ in Eq. (14) are defined as $|\chi_n\rangle \equiv T_n(\mathcal{H}_s)|\chi\rangle$, where $T_n(x)$ is the nth Chebyshev polynomial [91] and $\mathcal{H}_s \equiv \frac{\mathcal{H}-\bar{E}}{\Delta E}$ is the shifted-scaled Hamiltonian, having all eigenvalues in the interval $[-1, 1]$. Based on a recurrence formula between any three consecutive Chebyshev polynomials [91], the Chebyshev vectors χ_n can be computed iteratively (hence only three of them are needed at a given time):

$$|\chi_n\rangle = 2\mathcal{H}_s|\chi_{n-1}\rangle - |\chi_{n-2}\rangle, \quad n \geqslant 2.$$

The first two vectors are given by

$$|\chi_0\rangle = |\chi\rangle, \qquad |\chi_1\rangle = \mathcal{H}_s|\chi_0\rangle.$$

2. *Operating with several functions of $\mathcal{H}$ on a given state $|\chi\rangle$*

Each term in the Chebyshev expansion of Eq. (14) is a product of a Chebyshev coefficient Z^n and a Chebyshev vector $|\chi_n\rangle$. The former depends on the function $z(\mathcal{H})$, while the latter does not. Suppose we want to operate with several different functions $z_m(\mathcal{H})$ $(m = 1, 2, \ldots, M)$ on the *same* vector χ:

$$|\zeta_m\rangle = z_m(\mathcal{H})|\chi\rangle.$$

Chebyshev expansions can calculate these vectors,

$$|\zeta_m\rangle = \sum_{n=0}^{N_C-1} Z_m^{(n)}|\chi_n\rangle, \tag{16}$$

where $Z_m^{(1)}, Z_m^{(2)}, \ldots$ are the coefficients corresponding to the function $z_m(\varepsilon)$. Most of the numerical effort goes into computing the vectors $|\chi_n\rangle$, and these are shared by all the different evaluations in Eq. (16). Therefore, there is only a minute overhead in the effort to calculate M $|\zeta_m\rangle$'s relative to just one $|\zeta\rangle$.

3. *Energy windows*

An example of using this approach is the *Energy Windows* method [92]. Here, we define N_w chemical potentials,

$$\mu_{N_w} \equiv \mu \geqslant \mu_{N_w-1} \geqslant \cdots \geqslant \mu_1,$$

and corresponding energy window projections,

$$z_m(\mathcal{H}) = \sqrt{p_{\beta\mu_m} - p_{\beta\mu_{m-1}}}, \qquad m = 2, \ldots, N_w,$$
$$z_1(\mathcal{H}) = \sqrt{p_{\beta\mu_1}}.$$

Each of these functions projects a different energy range between the chemical potentials. The sum of the square of these functions yields the Fermi-Dirac projector

$$p_{\beta\mu}(\mathcal{H}) = z_{N_w}(\mathcal{H})^2 + z_{N_w-1}(\mathcal{H})^2 + \cdots + z_1(\mathcal{H})^2.$$

Therefore, for any one-body operator $\mathcal{A}$, the KS expectation value $\langle\mathcal{A}\rangle \equiv \mathrm{Tr}[p_{\beta\mu}(\mathcal{H})A]$ can be written as a sum of contributions from differing energy windows:

$$\langle\mathcal{A}\rangle = \sum_{m=1}^{N_w} \mathrm{Tr}[z_m(\mathcal{H})Az_m(\mathcal{H})].$$

The equivalent stochastic expression is

$$\langle\mathcal{A}\rangle = \sum_{m=1}^{N_w} \mathrm{E}[\langle\zeta_m|\mathcal{A}|\zeta_m\rangle].$$

Depending on the observable $\mathcal{A}$, this procedure helps reduce the fluctuations in estimating $\langle\mathcal{A}\rangle$ since ζ_m and $\zeta_{m'}$ span largely nonoverlapping energy windows.

In the left panel of Fig. 1, we show the standard deviation of the electronic force on the atomic nuclei (per degree of freedom) as a function of the number of windows for selected temperatures. It is seen that for low temperatures this standard deviation is reduced by as much as a factor of 2 as N_W reaches 16 or 32. However, for the high temperature considered, the windows are less efficient, reducing the standard deviation by, at most, a factor of 1.4.

4. *Chebyshev moments*

A Chebyshev moment M_n is the *trace* of a Chebyshev polynomial $T_n(\mathcal{H}_s)$. The overlap $\langle\chi|\chi_n\rangle$ is an unbiased estimator of M_n, based on the identity $\mathrm{Tr}[T_n(\mathcal{H}_s)] = \mathrm{E}[\langle\chi|T_n(\mathcal{H}_s)|\chi\rangle]$, or

$$M_n = \mathrm{E}[\langle\chi|\chi_n\rangle].$$

Knowledge of the moments allows us to compute the trace of any function $z(\mathcal{H})$ of the KS Hamiltonian $\mathcal{H}$ through the formula

$$\mathrm{Tr}[z(\mathcal{H})] = \sum_{n=0}^{N_C-1} Z^{(n)}M_n,$$

where $Z^{(n)}$ are the coefficients for the Chebyshev expansion of the function $z(\varepsilon)$.

The following examples show where moments are useful:

(i) When working in the canonical ensemble mentioned above, with a fixed number of electrons N_e, the chemical potential μ is a function of N_e defined implicitly by Eq. (8), depending on the KS eigenvalues ε_j. However, in sDFT, we do not have access to ε_j. Hence, we use the Chebyshev moments to develop an alternative implicit equation for μ:

$$N_e = 2 \times \sum_{n=0}^{N_C-1} P_{\beta\mu(N_e)}^{(n)} M_n, \tag{17}$$

where the $P_{\beta\mu}^{(n)}$'s are the Chebyshev coefficients corresponding to $p_{\beta\mu}(\varepsilon)$. The actual determination of μ uses a numerical root-searching algorithm (e.g., the bisection method) applied to Eq. (17). The search for μ is a speedy step since the Chebyshev moments are independent of μ, so they are calculated

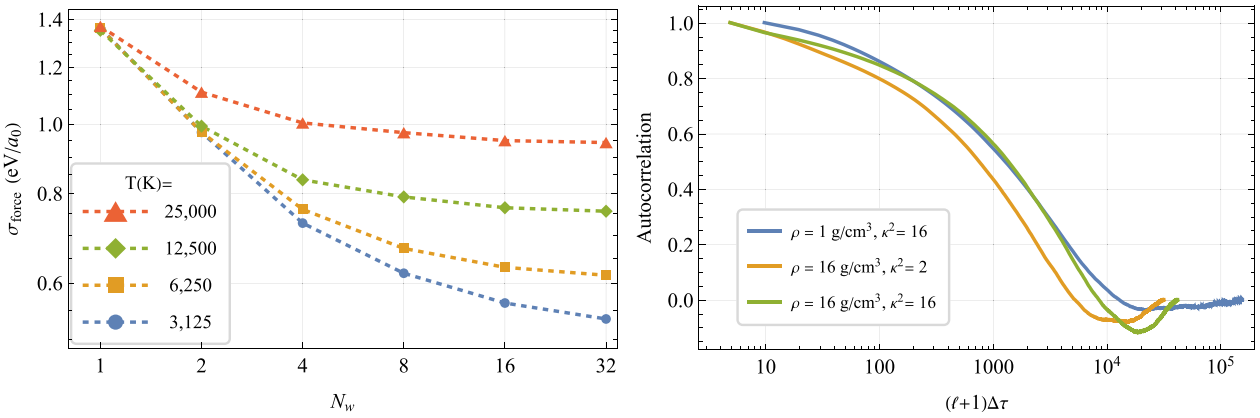


FIG. 1. Left panel: The sDFT force standard deviation $\sigma_f \equiv \sqrt{\frac{1}{3N_H}\mathrm{Tr}\Sigma_\phi^2}$ (per degree of freedom) for selected electronic temperatures as a function of the number of windows N_w in H_{128} at $\rho = 1$ g/cm^3. Right panel: The instantaneous position autocorrelation $C_R(\ell)$ [see Eq. (24), averaged over all atoms] during a $T = 30\,000$ K Langevin trajectory of H_{256} in two densities with additional white noise force [given in terms of κ, see Eq. (22)] and a time step of $\Delta t = 5\,\hbar E_h^{-1}$ for $\rho = 16$ g/cm^3 and $\Delta t = 10\,\hbar E_h^{-1}$ for $\rho = 1$ g/cm^3.

only once and then stored, while calculating the Chebyshev coefficients $P_{\beta\mu}$ for any value of μ only involves a single fast Fourier transform.

(ii) The noninteracting electron entropy of Eq. (7) is estimated as

$$S_s = 2 \times \sum_{n=0}^{N_C-1} S_{\beta\mu}^{(n)} M_n, \tag{18}$$

where $S_{\beta\mu}^{(n)}$ are the Chebyshev coefficients corresponding to the function $s_{\beta\mu}(\varepsilon) = -[p_{\beta\mu}(\varepsilon)\log p_{\beta\mu}(\varepsilon) + \bar{p}_{\beta\mu}(\varepsilon)\log \bar{p}_{\beta\mu}(\varepsilon)]$.

(iii) The orbital energy $E_{\rm orb}$ of Eq. (6) is estimated as

$$E_{\rm orb} = 2 \times \sum_{n=0}^{N_C-1} E_{\beta\mu}^{(n)} M_n,$$

where the $E_{\beta\mu}^{(n)}$ are the Chebyshev coefficients corresponding to $e_{\beta\mu}(\varepsilon) = p_{\beta\mu}(\varepsilon)\varepsilon$.

D. Performance of the sDFT calculation

Figure 2 shows the wall time self-consistent calculations (averaged over many sDFT Langevin dynamics steps) as a function of the number of electrons N_e in the simulation cell for hydrogen at specified densities and temperatures. The computation time of a single cycle of an SCF calculation scales linearly in $x = N_e \log N_e$. Since the number of SCF cycles required to converge to a given criterion grows mildly with system size, the overall scaling is $x^{1.3}$. Calculations with higher temperatures and the same number of electrons N_e are faster since the Chebyshev expansions shorten in inverse proportion to temperature [see Eq. (15)]. Higher density calculations with the same number of atoms N_e also require less computation time because of the smaller simulation cell sizes.

Let us discuss the wall times and their dependence on scale for the cutoff energy $E_{\rm cut}$. The plane-wave basis size is determined by the volume in G-space of the highest momentum vector $G_{\rm max} = \sqrt{\frac{2m_e}{\hbar^2}E_{\rm cut}}$ (where m_e is the electron mass and $\hbar$ is Planck's constant) and is therefore proportional to $E_{\rm cut}^{3/2}$. In addition, the length of the Chebyshev expansion is proportional to $E_{\rm cut}$ [see Eq. (15)]. Hence, overall, the wall time scales steeply as $E_{\rm cut}^{5/2}$, i.e., wall time increases by a factor 32 every time the cutoff energy increases by a factor 4.

We have not yet developed the capability to expedite the calculation speed for each stochastic orbital. We can achieve high factors if we use a GPU on each node for this purpose.

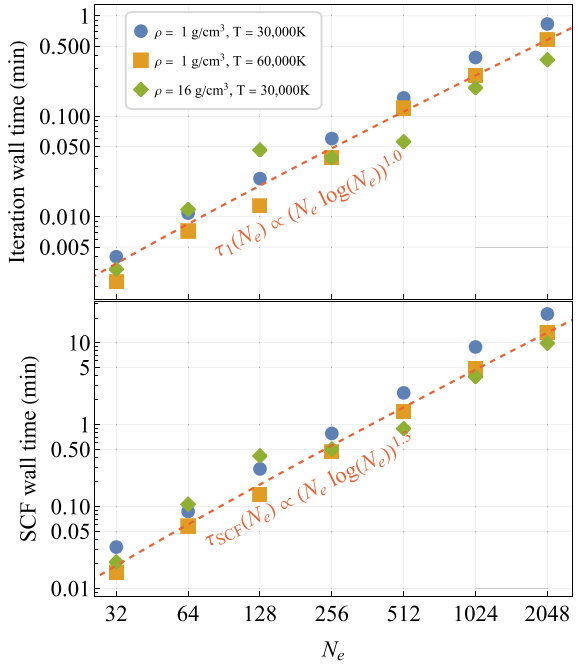


FIG. 2. The self-consistent-field (SCF) wall times as a function of the number of electrons N_e for hydrogen at the specified densities and temperatures. Top panel: a single SCF iteration; bottom panel: the entire SCF calculation (stopped when the changes in energy per electron are below 10^{-5}E$_h$). The calculations used the cutoff energy of $E_{\rm cut} = 9$ E$_h$, 40 stochastic orbitals, and a *single core per stochastic orbital* on our Core-i7 cluster.

III. STOCHASTIC FORCES AND LANGEVIN DYNAMICS

In the previous section, we discussed the WDM's electronic structure at inverse temperature β. In this section, we concentrate more on the behavior of the atomic nuclei in WDM. At thermal equilibrium their state is canonically distributed with a temperature identical to that of the electrons. Here we discuss how we use the method of Langevin dynamics to estimate the expected value of various observables concerning atomic nuclei within the canonical ensemble.

A. Regularization of the stochastic forces

In sDFT, the force on each atomic nucleus is a vector of a random variable components [72]:

$$\boldsymbol{f} = -2 \times \langle \eta | \nabla \hat{v}_{\mathrm{eN}} | \eta \rangle + \boldsymbol{F}^{\mathrm{NN}}, \tag{19}$$

where $\eta(\boldsymbol{r})$ is defined in Eq. (10), and $\boldsymbol{F}^{\mathrm{NN}}$ is the force due to the other bare atomic nuclei. Using the stochastic trace formula, the force $\boldsymbol{F}$ of Eq. (9) is the expected value of the random force:

$$\boldsymbol{F} = \mathrm{E}[\boldsymbol{f}].$$

The $3N_n \times 3N_n$ symmetric positive-definite force covariance matrix is $(\Sigma_f^2)_{ii'} = \mathrm{E}[f_i f_{i'}] - F_i F_{i'}$, or, in matrix notation,

$$\Sigma_f^2 \equiv \mathrm{E}[\boldsymbol{f}\boldsymbol{f}^T] - \boldsymbol{F}\boldsymbol{F}^T. \tag{20}$$

To ease the handling of stochastic forces, we add independent white noise $\boldsymbol{\zeta}$ ($\mathrm{E}[\boldsymbol{\zeta}] = 0$):

$$\boldsymbol{\varphi} = \boldsymbol{f} + \boldsymbol{\zeta}. \tag{21}$$

The covariance matrix $\mathrm{E}[\boldsymbol{\zeta}\boldsymbol{\zeta}^T]$ of this additional white noise is specially constructed to allow the covariance $\Sigma_{\boldsymbol{\varphi}}^2$ of the total force to be uniform, i.e., a *multiple of the unit matrix*:

$$\Sigma_{\boldsymbol{\varphi}}^2 \equiv \mathrm{E}[\boldsymbol{\varphi}\boldsymbol{\varphi}^T] - \boldsymbol{F}\boldsymbol{F}^T = \sigma^2 \mathrm{I} = \kappa^2 \sigma_f^2 \mathrm{I}, \tag{22}$$

where σ^2 is larger ($\kappa \geqslant 1$) than the largest eigenvalue σ_f^2 of Σ_f^2. The white noise force ζ is thus sampled, using the Metropolis-Hastings algorithm, to have a Gaussian distribution with the positive-definite covariance matrix $\Sigma_\zeta^2 \equiv \sigma^2 I - \Sigma_f^2$. The procedure obviously requires an estimate of the sDFT force covariance Σ_f^2 and we use a sample of N_s force vectors to estimate it (with $N_s = 50$, seemingly quite sufficient). The covariance estimate is done once every N_j MD step (we took $N_j = 150$). A force having such a uniform covariance matrix enables using the same friction coefficient for all degrees of freedom, and therefore simplifies the temperature control in the Langevin dynamics calculation.

B. Stochastic Langevin equations of motion

The stochastic force $\boldsymbol{\varphi}(\boldsymbol{R})$ for a given atomic nuclei configuration is now used to perform Langevin molecular dynamics from which we obtain configuration and momentum samples that are canonically distributed. From these samples we can compute the thermodynamic properties of the system. The dynamics involves solving the Langevin equation of motion

$$\dot{\boldsymbol{P}}(t) = \boldsymbol{\varphi}(\boldsymbol{R}(t)) - \gamma \boldsymbol{P}(t),$$
$$\dot{\boldsymbol{R}}(t) = M^{-1}\boldsymbol{P}(t),$$

where M^{-1} is a diagonal matrix of the inverse nuclei mass, and γ is the diagonal matrix of friction coefficients. We use a time-discretized solver [93] for the stochastic differential equation, from which we obtain a discretized trajectory of N_T atomic configurations $\boldsymbol{R}^{(n)} = \boldsymbol{R}(n\Delta\tau)$ $(n = 1, \ldots, N_T)$ and their momenta $\boldsymbol{P}^{(n)} = \boldsymbol{P}[(n - \frac{1}{2})\Delta\tau]$, where $\Delta\tau$ is the time step. The phase-space trajectory is built from the following evolution steps:

$$\boldsymbol{P}^{(n+1)} = e^{-\gamma\Delta\tau}\boldsymbol{P}^{(n)} + \left(\frac{1 - e^{-\gamma\Delta\tau}}{\gamma}\right)\boldsymbol{\varphi}(\boldsymbol{R}^{(n)}),$$
$$\boldsymbol{R}^{(n+1)} = \boldsymbol{R}^{(n)} + M^{-1}\boldsymbol{P}^{(n+1)}\Delta\tau,$$

and in the limit $\Delta\tau \to 0$ a Langevin trajectory is obtained. Here, the (diagonal) friction matrix γ is determined from the fluctuation-dissipation relation, which is given by

$$\sigma^2 = \frac{\gamma\Delta\tau/2}{\tanh(\gamma\Delta\tau/2)} \times \frac{2\gamma M}{\beta}. \tag{23}$$

C. Statistical sampling

For sufficiently small $\Delta\tau$, each of the trajectory configurations $\boldsymbol{R}^{(n)}$ is equivalent to a sample taken from the Boltzmann distribution $p_\beta^B(\boldsymbol{R}) \propto e^{-\beta V_{\mathrm{BO}}(\boldsymbol{R})}$, where $V_{\mathrm{BO}} \equiv \Phi_{\beta\mu} + E_{\mathrm{NN}}$ ($V_{\mathrm{BO}} = \mathcal{F}_{\beta N_e} + E_{\mathrm{NN}}$) is the *electronic* grand-canonical (canonical) potential [see Eq. (5)]. The momentum $\boldsymbol{P}^{(n)}$ is equivalent to a sample from the Maxwell-Boltzmann probability distribution function $p_{R\beta}^{\mathrm{MB}}(\boldsymbol{P}) \propto e^{-\beta\sum_{i=1}^{N_N}\frac{P_i^2}{2M_i}}$.

The estimate for the thermal average $\langle O \rangle_\beta \equiv \iint O(\boldsymbol{R},\boldsymbol{P}) p_\beta^B(\boldsymbol{R}) d\boldsymbol{R} p_\beta^{MB}(\boldsymbol{P}) d\boldsymbol{P}$ of a given observable $O(\boldsymbol{R},\boldsymbol{P})$ is simply the sample mean $\bar{O} \equiv \frac{1}{N_T}\sum_{n=1}^{N_T} O^{(n)}$ over the sequence $O^{(n)} \equiv O(\boldsymbol{R}^{(n)}, \boldsymbol{P}^{(n)})$. The sample variance $\overline{\Delta O^2} = \frac{1}{N_T}\sum_{n=1}^{N_T}\Delta O^{(n)}$, where $\Delta O^{(n)} = O^{(n)} - \bar{O}$, allows us to determine a confidence interval for the thermal average. For example, the 70% confidence interval is $[\bar{O} - \delta O, \bar{O} + \delta O]$, where $\delta O \equiv \sqrt{\frac{1}{N_{\mathrm{ind}}}\overline{\Delta O^2}}$ and N_{ind} is the number of statistically independent samples in the sequence $O^{(n)}$. If the values $O^{(1)}, O^{(2)}, \ldots$ were uncorrelated, then N_{ind} would be just the sample size N_T. However, because the configurations $\boldsymbol{R}^{(n)}$ are part of a *molecular-dynamics trajectory*, $O^{(n+1)}$ is *correlated* with $O^{(n)}$, and $O^{(n+2)}$ is correlated with $O^{(n+1)}$, etc., and therefore $N_{\mathrm{ind}} < N_T$. It is common to quantify the strength of this correlation using *the autocorrelation function* for O, defined by $C_O(\ell\Delta\tau) \equiv \frac{\langle \Delta O^{(n)} \Delta O^{(n+\ell)} \rangle}{\langle \Delta O^{(n)2} \rangle}$ (the expression on the right-hand side is independent of n). In a given sample trajectory, the autocorrelation function is estimated by

$$C_O(\ell\Delta\tau) \approx \frac{\sum_n \Delta O^{(n)} \Delta O^{(n+\ell)}}{\sum_n \Delta O^{(n)2}}. \tag{24}$$

It starts with the value $C_O(0) = 1$ (full correlation) and then decays steadily as step separation ℓ grows until hitting a regime of small random fluctuations. The decay is characterized by a correlation time τ_O, for which $C_O(\tau_O) = e^{-1}$.

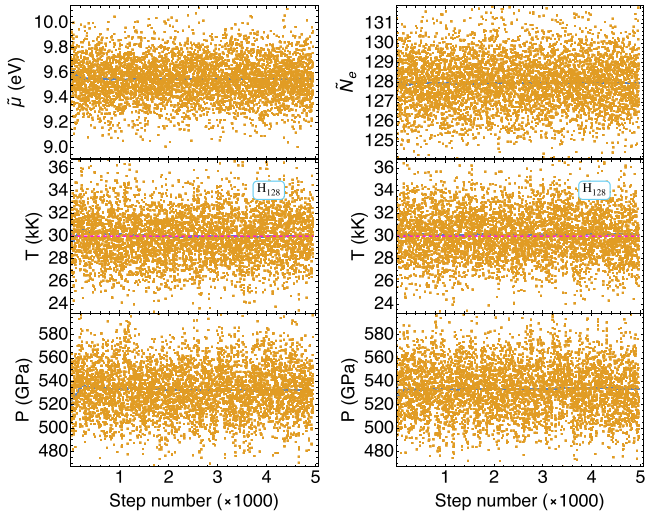


FIG. 3. The instantaneous values (brown) and running averages (blue) of observables in two Langevin molecular-dynamics trajectories of H_{128} (at a mass density of $\rho = 1\,\mathrm{g/cm^{-3}}$ and a target temperature of 30 000 K). Left panel: the NVT-like trajectory, where the number of electrons is fixed ($N_e = 128$) by tuning the chemical potential $\tilde{\mu}^{(n)}$ at each time step [see Eq. (8)]. Right panel: the μVT trajectory, where the chemical potential is fixed ($\mu = 9.56$ eV) while the number of electrons $N_e^{(n)}$ fluctuates. Details of the Langevin dynamics: the white noise fluctuation is $\sigma = 4\sigma_f$, i.e., $\kappa = 4$ [see Eq. (22)], the time step is $\Delta\tau = 10$ atu, and the sDFT force covariance [see Eq. (20)] is calculated using 50 independent samples once every 150 dynamical time steps.

We also define the *correlation length* $\ell_O = \frac{\tau_O}{\Delta\tau}$. We view ℓ_O consecutive samples as "correlated" while later samples are considered *uncorrelated*. The number of *effectively independent* samples is thus estimated as $N_{\mathrm{ind}} \approx N_T/\ell_O$. In the right panel of Fig. 1 we show the Langevin dynamics position autocorrelation function $C_R(\ell\Delta\tau)$ of hydrogen at $T = 30\,000$ K, for two densities ρ and two white noise parameters κ^2 [see Eq. (22)]. The correlation times τ_R are weakly dependent on the density but grow significantly with κ. Hence, we strive for small values of $\kappa^2 > 1$.

D. Computational demonstration of μVT-N_eVT ensemble equivalence

Figure 3 displays time-dependent values of selected observables in two Langevin dynamics trajectories of hydrogen at mass density $\rho = 1\,\mathrm{g/cm^{-3}}$ at $T = 30\,000$ K. The two trajectories are calculated in different electronic ensembles: the left panel of the plot shows the results of an N_eVT-like ensemble, where we impose a constant electron number $N_e = 128$ at each time step by tuning the electronic chemical potential $\tilde{\mu}(N_e; \boldsymbol{R}^{(n)})$ in the Fermi-Dirac function at each time step [see Eq. (8)]. This chemical potential fluctuates in time, as do the positions and momenta of the atomic nuclei. The right panel shows the results of an μVT ensemble, where the electronic chemical potential is set to a constant value of $\mu = 9.56$ eV. Now the number of electrons fluctuates, but *on average* it is 128. The observables are the kinetic energy per atomic degree of freedom $T^{(n)}$ (divided by k_B and given in 10^3 Kelvin), the pressure $P^{(n)}$, the chemical potential $\tilde{\mu}^{(n)}$, and the Helmholtz energy $\tilde{\mathcal{F}}^{(n)}_{\beta N_e}$ in the left panel, and the electron number $\tilde{N}_e^{(n)}$ and the grand potential $\tilde{\Phi}^{(n)}_{\beta\mu}$ in the right panel. Upon studying the numerical results in Fig. 3, it is obvious that the average over the fluctuating chemical potential in the left panel $\langle\tilde{\mu}\rangle_{N_eVT} = \frac{1}{N_T}\sum_{n=1}^{N_T}\tilde{\mu}(N_e; \boldsymbol{R}^{(n)})$ is very similar to the constant chemical potential μ imposed in the μVT ensemble in the right panel. Similarly, the average over the fluctuating number of electrons in the right panel $\langle\tilde{N}_e\rangle_{\mu VT} = \frac{1}{N_T}\sum_{n=1}^{N_T}\tilde{N}_e(\mu; \boldsymbol{R}^{(n)})$ is very close to the imposed number of electrons N_e used in the N_eVT ensemble in the left panel. These results can be summarized in the following relation:

$$\mu = \langle\tilde{\mu}\rangle_{N_eVT} \Leftrightarrow N_e = \langle\tilde{N}_e\rangle_{\mu VT},$$

showing that in our finite-sized system, the two ensembles μVT and N_eVT are already equivalent, which is characteristic of the thermodynamic limit. All calculations shown in the next section were performed in the N_eVT ensemble.

IV. KUBO-GREENWOOD CONDUCTIVITY

In this section, we consider the stochastic calculation of the Kubo-Greenwood conductivity [94,95]. In the context of WDM, these calculations were addressed in Refs. [96,97] but they become demanding as the system size and temperature increase. Hence, a stochastic calculation may be preferable for such systems as discussed in Ref. [74]. Here, we provide an improved approach including the dc conductivity with considerably lower statistical errors. We also provide a detailed description of the theory, the derivation, and how the calculations were made.

Kubo's analysis [94] starts with expressing the complex conductivity,

$$\sigma_{\xi\xi'}(\omega) = \int_0^\infty \phi_{\xi\xi'}(t)e^{-i\omega t}dt, \tag{25}$$

as the Fourier transform of the dipole-current-density response function:

$$\phi_{\xi\xi'}(t) = \frac{1}{i\hbar}\mathrm{tr}\left(\rho\left[\sum_n e\mathcal{R}_{n\xi}, \sum_{n'}\frac{e\mathcal{V}_{n'\xi'}(t)}{\Omega}\right]\right),$$

where e is the electron charge, tr is a many-body trace, ρ is the equilibrium (many-body) density matrix, $\mathcal{R}_{n\xi}$ is the position in Cartesian direction ξ ($\xi = x, y, z$) of electron n, and $\mathcal{V}_{n\xi} \equiv \frac{\hbar}{m_e}(\frac{1}{i}\frac{\partial}{\partial\mathcal{R}_{n\xi}} - k_\xi)$ is the corresponding velocity (where $k_\xi = \frac{\pi}{2L_\xi}$ is the Baldereschi k-point). For noninteracting electrons, the response function reduces to a single electron expression (see Appendix A):

$$\phi_{\xi\xi'}(t) = \frac{4e^2}{\hbar\Omega}\mathrm{Im}\,\mathrm{Tr}(p_{\mu\beta}(\mathcal{H})\mathcal{R}_\xi\mathcal{V}_{\xi'}(t)), \tag{26}$$

where Tr is a single-particle operator trace, $\mathcal{R}_\xi$ and $\mathcal{V}_{\xi'}$ are single electron position and velocity operators, respectively, $p_{\mu\beta}(\mathcal{H})$ is the Fermi-Dirac distribution, and $\mathcal{H}$ is the single-particle Hamiltonian (at the Baldereschi k-point), which we take from KS-DFT. We have also included a factor 2 due to spin-degeneracy. The use of such a static KS Hamiltonian, as opposed to the TDDFT description, is the central approximation of the Kubo-Greenwood theory.

For $\omega \neq 0$, we multiply and divide by $-i\omega$ the integral of Eq. (25), use the identity $-i\omega e^{-i\omega t} = \frac{d}{dt}e^{-i\omega t}$, and then integrate by parts, obtaining

$$\sigma_{\xi\xi'}(\omega) = \frac{1}{i\omega}\left(-\phi_{\xi\xi'}(0) + \int_0^\infty \dot{\phi}_{\xi\xi'}(t)e^{-i\omega t}dt\right), \tag{27}$$

which involves the velocity-velocity response function:

$$\dot{\phi}_{\xi\xi'}(t) = -\frac{4e^2}{\hbar\Omega}\mathrm{Im}\,\mathrm{Tr}(p_{\mu\beta}(H)\mathcal{V}_\xi\mathcal{V}_{\xi'}(t)).$$

For evaluating the trace, we use the stochastic trace formula:

$$\mathrm{Tr}(p\mathcal{V}_\xi\mathcal{V}_{\xi'}(t)) = \mathbb{E}[\langle\zeta_{\xi t}|\mathcal{V}_{\xi'}|\eta_t\rangle], \tag{28}$$

where, for brevity, $p = p_{\beta\mu}(\mathcal{H})$ and

$$|\eta_t\rangle \equiv e^{-i\mathcal{H}t/\hbar}\sqrt{p}|\chi\rangle, \quad |\zeta_{\xi t}\rangle \equiv e^{-i\mathcal{H}t/\hbar}\mathcal{V}_\xi|\eta\rangle,$$

and $|\chi\rangle$ is a stochastic state. To use Eq. (28) we generate a sample of N_s stochastic vectors χ, and for each, we obtain a specific value of $\langle\zeta_{\xi t}|\mathcal{V}_{\xi'}|\eta_t\rangle$. Averaging these values gives an estimate of the trace in the response function with a statistical error proportional to $1/\sqrt{N_s}$.

The trace operations provide correlation functions, which we denote $\dot{\phi}(t)$ [whether $\dot{\phi}_{\xi\xi'}(t)$ described above or $\dot{\psi}_{\xi\xi'}(t)$ described below]. To use it for obtaining the conductivity as a function of ω, we first select a desired spectral energy resolution $\hbar\nu$, which defines a frequency grid $\omega_g = g \times \nu$, where $g = 0, 1, \ldots, N_\omega$, and then we perform the Fourier integral of Eq. (27) for these frequencies. Given the resolution, the integral of the correlation function $\dot{\phi}(t)$ is augmented by a Gaussian window, discretized, and summed utilizing the fast-Fourier algorithm

$$\begin{aligned}\int_0^\infty \dot{\phi}(t)e^{-i\omega_g t}dt &\to \int_0^\infty e^{-\frac{\nu^2t^2}{2}}\dot{\phi}(t)e^{-i\omega_g t}dt \\ &\to \frac{\tau_f}{N_\omega}\sum_{g'=0}^{N_\omega} w_{g'}e^{-\frac{\nu^2\tau_{g'}^2}{2}}\dot{\phi}(\tau_{g'})e^{-i\omega_g\tau_{g'}}\end{aligned} \tag{29}$$

on an equally spaced time-grid $\tau_g = g \times \frac{\tau_f}{N_\omega}$, extending from zero to $\tau_f = 7/\nu$. The number of time and frequency grid points is taken as $N_\omega = q_{\mathrm{fac}} \times \frac{E_{\mathrm{cut}}}{\hbar\nu}$, where the quality factor $q_{\mathrm{fac}} > 1$ determines the precision of the time integration. We also inserted integration weights, the simplest of which is the trapeze rule: $w_k = (1 - \delta_{k0}/2)$. These weights are essential as the integral is a half-Fourier transform, which means that the integrand does not decay smoothly to zero at the time-grid boundaries. We experimented with various choices of ν and q_{fac}, finding that a resolution of $\hbar\nu = 0.025$ $\mathrm{E_h}$ and a quality factor in the range of 3–5 yield meaningful and stable results. Dividing these values by $i\omega_g$ $(g > 0)$, we obtain the ac conductivity $\sigma_{\xi\xi'}(\omega_g)$.

Since evaluating the conductivity in Eq. (27) requires division of the Fourier integral by ω, the statistical fluctuations are amplified as $\omega \to 0$. The procedure is undefined for $\omega = 0$, the dc limit. In this case, we could use the analytical limit of Eq. (27),

$$\mathrm{Re}\sigma_{\xi\xi'}(0) = \int_0^\infty \dot{\phi}_{\xi\xi'}(t)t\,dt, \tag{30}$$

which does not divide by zero. We can use the same integration procedure outlined above for the integral. But experience shows that the stochastic error in Eq. (30), although finite, is not small and requires extensive sampling. For the important case of $\xi = \xi'$, it is possible to show (see Appendix B) that

$$\mathrm{Re}\sigma_{\xi\xi}(0) = \int_0^\infty \dot{\psi}_{\xi\xi}(t)dt, \tag{31}$$

where [see Eq. (B4)]

$$\dot{\psi}_{\xi\xi}(t) = -\frac{2e^2}{\Omega}\,\mathrm{Re}\,\mathrm{Tr}(p'_{\mu\beta}(H)\mathcal{V}_\xi\mathcal{V}_\xi(t)),$$

and $p'_{\mu\beta}(\varepsilon) = -\beta p_{\mu\beta}(\varepsilon)[1 - p_{\mu\beta}(\varepsilon)]$ is the derivative of the Fermi-Dirac function. The stochastic evaluation of the correlation function $\mathrm{Tr}(p'_{\mu\beta}(H)\mathcal{V}_\xi\mathcal{V}_\xi(t))$ follows the same procedure as $\mathrm{Tr}(p_{\mu\beta}(H)\mathcal{V}_\xi\mathcal{V}_\xi(t))$ except that this time we take $p = p'_{\beta\mu}(\mathcal{H})$. Then, the same time-integration scheme outlined above for the Fourier integral of $\dot{\phi}_{\xi\xi}$ can be used to evaluate the integral of Eq. (31).

The problem of high fluctuations in the low-frequency part of the ac conductivity is exacerbated due to the need to take smaller ν for converging the ac results to the dc limit: the smaller ν is, the larger are the fluctuations. Thus, we developed an interpolation procedure for the low-frequency spectrum relying on the steadiness of the dc conductivity. This procedure is described in Appendix C.

For calculating the direction-averaged conductivity, $\bar{\sigma} = \frac{1}{3}(\sigma_{xx} + \sigma_{yy} + \sigma_{zz})$, we replace the ξ component of the velocity $(\mathcal{V}_\xi)$ in the above equations by a random-direction component $\mathcal{V}_d = \boldsymbol{\eta}^T\boldsymbol{V}$, where $\boldsymbol{\eta} = (\eta_x, \eta_y, \eta_z)$, taken as a *random point* on the 3D unit sphere, since $\mathbb{E}[\boldsymbol{\eta}\boldsymbol{\eta}^T] = \frac{1}{3}\mathcal{I}$, where $\mathcal{I}$ is the 3×3 unit matrix. Averaging over $\mathcal{V}_d$ automatically computes $\bar{\sigma}$.

V. TEST CASE: HYDROGEN AT 30 000 K

In this section, we use as a test case hydrogen at 30 000 K. We first consider system-size effects on the estimation of pressure and conductivity. Then, we give its equation of state, electric conductivity, and radial distributions, comparing, where possible, with VASP [98–102].

All sDFT calculations in this section used 40 stochastic orbitals (for all system sizes), the LDA exchange-correlation energy functional, and norm-conserving pseudopotentials [103]. Unless specifically mentioned otherwise, we use 9 $\mathrm{E_h}$ cutoff energy and the Baldereschi k-point [104].

A. System-size-dependent pressure and conductivity

In Fig. 4 we present the pressure (left panel) and the conductivity (right panel) estimates for hydrogen at 30 000 K and density $\rho = 1$ g/cm^3, as a function of the system size. The pressure estimates at the Baldereschi k-point are rather steady and change only mildly with system size. Those done at the Γ point show a stronger sensitivity to system size, peaking at H_{256} and then decreasing towards the steadier k-point values. The sDFT pressure estimates increase by about 5% when going from cutoff energy of 9 to 25 $\mathrm{E_h}$. The dDFT results, based on the VASP code, are less sensitive to the cutoff energy and change by only 2.5%. This reflects the superiority of the PAWs

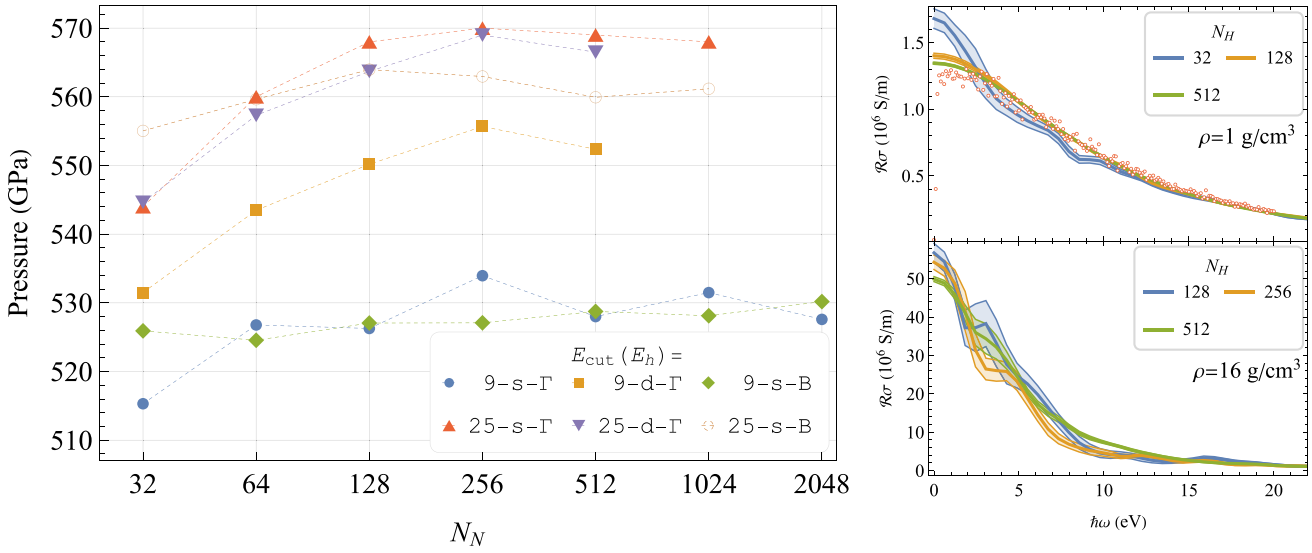


FIG. 4. Pressure and conductivity averaged over a Langevin trajectory. Left panel: Size dependence of pressure at density 1 g/cm^3. Each point on the graph is an average over the pressure estimates along the xDFT (x="s" or "d") trajectory, performed using 9 or 25 E_h cutoff energy at the Γ or B (Baldereschi) k-point, as indicated in the legend. The sDFT calculations for each point on the Langevin trajectory used 40 stochastic orbitals at the LDA/NCPPs level. The dDFT calculations were performed by the VASP program [98–102], at the LDA/PAW level. The trajectory time step was $\Delta\tau = 5$ atu, and white noise parameter $\kappa^2 = 2$. Right panels: Size dependence of the conductivity where the top (bottom) panel shows results for $\rho = 1(16)$ g/cm^3. Each conductivity curve is an average over the conductivity curves calculated for $N_s = 20$ configurations of the atomic nuclei (snapshots) taken every 1000 atu along the sDFT/Langevin trajectory. The error bars are $\pm s/\sqrt{N_s}$, where s is the standard deviation. One conductivity calculation produces an entire conductivity curve $[\sigma(\omega)]$ based on 120 stochastic orbitals, performed at the Baldereschi k-point, with a 15 E_h cutoff energy. Dark empty circles appearing in the top-right panel are conductivity calculations for H_{128} on the identical configurations using the deterministic conductivity method of Ref. [96] using VASP.

used by VASP over the norm-conserving pseudopotentials used in the sDFT calculation when converging to the infinite energy cutoff limit. The sDFT and the VASP pressure estimates are similar at the higher cutoff energy.

The size dependence of hydrogen conductivity at 30 000 K, calculated at the Baldereschi k-point, is shown for two density values in the right panel of Fig. 4. For 1 g/cm^3, the conductivity curves of H_{128} and H_{512} are already quite close (a difference of 3%). Note that the larger the system, the smaller the fluctuations. We also show results from a deterministic calculation on H_{128}, which tend to be too small as ω decreases but fit our results well for all other frequencies.

Finally, the conductivity for the high-density systems is much more noisy than at low density, and the system size effects are more noticeable, since the simulation cell size is small for these systems.

B. Density-dependent properties of hydrogen at 30 000 K

The estimated pressure of hydrogen at $T = 30\,000$ K as a function of density is depicted for sDFT and dDFT (using VASP) in the left panel of Fig. 5. The two curves are generally close. The more significant difference in the lower-pressure estimates stems primarily from the smaller cutoff energy used in our calculation. The equation of state can be fitted by a van der Waals form, $P = P_{\text{ideal}}(1 + \frac{\rho}{\rho_0})$ with $\rho_0 = 0.87$ g/cm^3.

The right panel of Fig. 5 illustrates the radial distribution for hydrogen at $T = 30\,000$ K, with varying densities from 0.25 to 16 g/cm^3. At the lowest density, it reveals a relatively large excluded volume with some corrugated pattern. As the density increases to 1 g/cm^3, the radial distribution curve steepens as the proton-proton repulsion range shortens, and the corrugated pattern largely dies out, leaving a shallow signature of a correlation shell at r = 1.5 Å. This feature is enhanced and contracts to a shorter distance of 0.75 Å at the density of 4 g/cm^3. In this regime, the radial distribution signifies a combined short-range repulsion and longer-range attraction between pairs, typical of a gas. Finally, at the highest density considered, 16 g/cm^3, the correlation shell contracts further to 0.5 Å while a second correlation shell seems to form 0.9 Å, hence a radial distribution typical of a liquid emerges at these high densities.

We now turn to studying hydrogen conductivity using Drude's theory of metals [105] as a reference point. Drude's theory gives the real part of the normalized conductivity at frequency ω as

$$\frac{\text{Re}\sigma(\omega)}{n} = \frac{e^2}{m_e}\frac{\tau_c}{1+\omega^2\tau_c^2}, \tag{32}$$

where $n = \frac{N_e}{\Omega}$ is the average electron density, and τ_c, the collision time, is the only material parameter. τ_c is assumed to be independent of n. In Fig. 6 (left panel) we plot our stochastic estimates of the *ab initio* normalized conductivity for hydrogen in various densities at 30 000 K. While the normalized conductivity in Drude's theory [Eq. (32)] does not depend on n, the *ab initio* dc normalized conductivity does depend on it: it changes fourfold as n changes 64-fold. Yet, as seen in Fig. 6, at $\hbar\omega = 7.2$ eV, all four *ab initio* curves cross at approximately the same point, the *isosbestic*

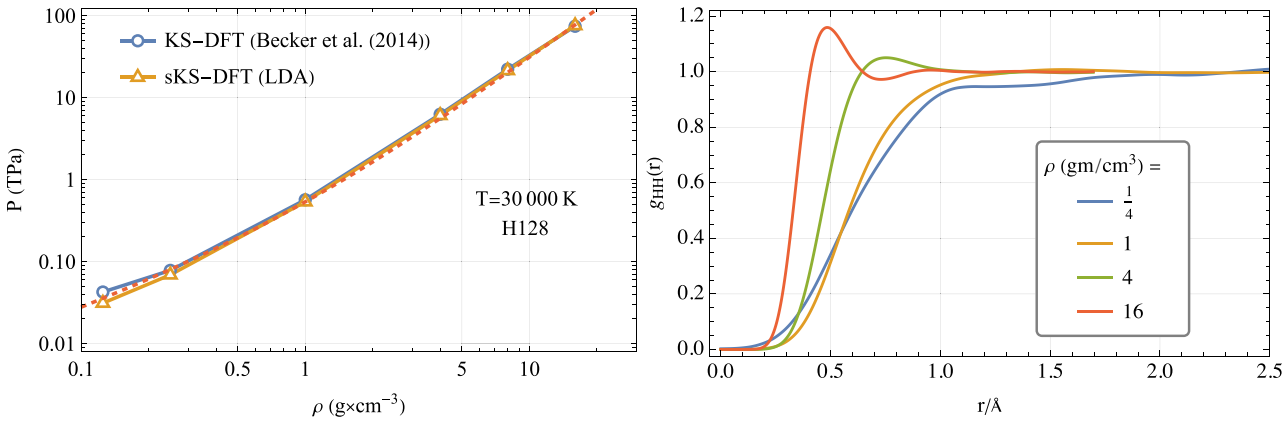


FIG. 5. Left panel: the estimated pressure as a function of density for hydrogen at $T = 30,000$ K. The results of the sDFT calculations are shown together with the calculations taken from Ref. [13] and a dotted van der Waals trend of $P(\rho) = \frac{\rho}{m_p} k_B T (1 + \frac{\rho}{\rho_0})$, where $\rho_0 = 0.87$ g/cm^3 is obtained by fitting. Right panel: the H-H radial distribution for different densities.

point, where they assume *the same* normalized conductivity value of 0.6×10^{-3} Sa$_0^2$. The existence of the isosbestic point, especially in the rather large density range seen here, is sometimes indicative of a system composed of two phases or two states [106–108]. The value of τ_c at the isosbestic point is equal to $(0.084 \pm 0.035i)$ fs, with the real part small relative to typical values of τ_c for room-temperature metals (between 1 and 10 fs [105]). This result is consistent with the dense metal (with r_s between 0.28 and 0.7) we have, and the high temperatures should speed up relaxation times and shorten mean free paths in the material. Equation (32) also shows that Reσ is proportional to ω^{-2} for high frequencies, $\omega\tau_c \gg 1$ (in our case, $\hbar\omega > 30$ eV). As seen in the inset of the figure, the *ab initio* conductivity decreases faster than the Drude second power law in the frequency.

The relative statistical errors in the conductivity evaluation (before stabilization according to the method of Appendix C) are shown in the right panel of the figure. In general, they grow with the density of the gas. Remarkably, the dc conductivity, calculated through Eq. (31), has a much smaller statistical error than the ac conductivity.

VI. SUMMARY

We developed a linear-scaling stochastic DFT implementation in periodic boundary conditions combined with Langevin dynamics, which we applied to hydrogen at 30 000 K. Our pressure estimates at various hydrogen densities between 0.125 and 16 g/cm^3 matched well with results based on deterministic DFT for a high cutoff energy (near convergence). The sensitivity to the cutoff energy reduced as the density increased.

The pair correlation functions showed that hydrogen exhibits gaslike behavior at densities below 4 g/cm^3 and liquidlike behavior above it. We also developed a stochastic method to estimate the Kubo-Greenwood conductivity with minimal statistical noise at $\omega \to 0$. All the calculations were done in the Baldereschi k-point, and then the overall size effects in the hydrogen systems were not large once H_{512} was used, except for the high density, which required a large number of atoms.

Future work will focus on adapting stochastic time-dependent DFT [109–111] and Green's function

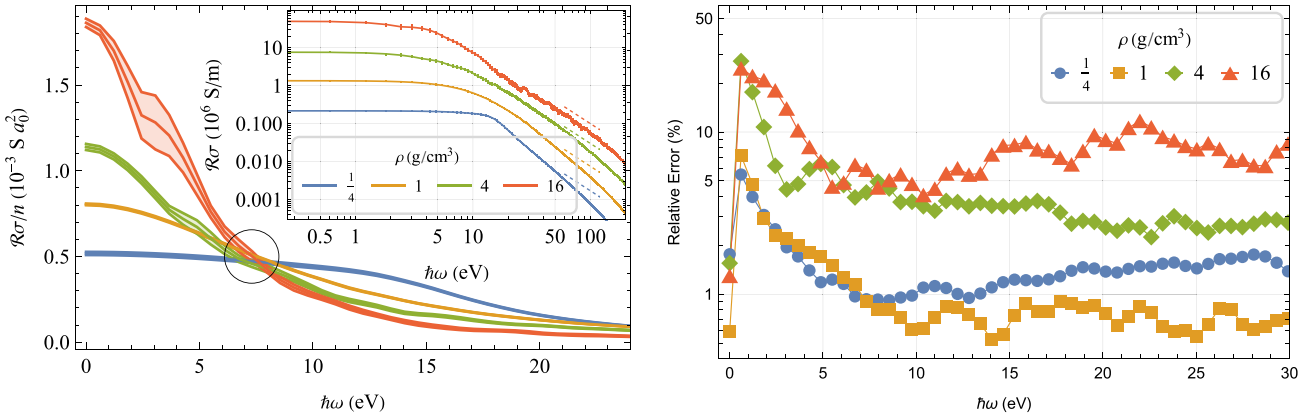


FIG. 6. Left panel: The real part of the Kubo-Greenwood conductivity normalized by the electron density at $T = 30\,000$ K. The black circle indicates an *isosbestic point*, which appears at 7.2 eV, where all systems have the same normalized conductivity of $\sim 0.5 \times 10^{-3}$ Sa$_0^2$. The inset shows the conductivity in log-log scale, with dashed lines indicating slopes of ω^{-2}. Right panel: The relative error bars for the conductivity calculations, as described in the caption of Fig. 4.

methodologies [112–114] for WDM applications, building on the foundation of our current work.

ACKNOWLEDGMENTS

R.B., R.E.H., A.R., and R.R. thank the German Israel Foundation for funding this project. E.R. acknowledges support from the Center for Computational Study of Excited-State Phenomena in Energy Materials (C2SEPEM) at the Lawrence Berkeley National Laboratory, funded by the U.S. Department of Energy, Office of Science, Basic Energy Sciences, Materials Sciences and Engineering Division, under Contract No. DE-AC02-05CH11231, as part of the Computational Materials Sciences Program.

APPENDIX A: PROOF OF EQ. (26)

For noninteracting electrons, the Hamiltonian and the grand-canonical distribution are

$$H=\sum_i \varepsilon_i n_i, \quad n_i \equiv a_i^\dagger a_i, \quad N=\sum_i n_i, \quad \rho=\frac{e^{-\beta(H-N\mu)}}{\mathrm{tr}[e^{-\beta(H-N\mu)}]},$$

where a_i ($a_i^\dagger$) are electron annihilation (creation) operators into eigenstates of the Hamiltonian, with the standard anti-commutation relations $\{a_i, a_j\} = \{a_i^\dagger, a_j^\dagger\} = 0$, $\{a_i a_j^\dagger\} = \delta_{ij}$.

From these relations alone, we find the following:

$$[a_i^\dagger a_j, a_k^\dagger a_l] = \delta_{jk} a_i^\dagger a_l - \delta_{il} a_k^\dagger a_j, \tag{A1}$$

$$\mathrm{tr}[\rho a_i^\dagger a_l] = \delta_{il}\mathrm{tr}[\rho n_i] \equiv \delta_{il} p_{\mu\beta}(\varepsilon_i), \tag{A2}$$

and

$$e^{iHt} a_k^\dagger a_l e^{-iHt} = e^{-i(\varepsilon_l-\varepsilon_k)t} a_k^\dagger a_l. \tag{A3}$$

From Eqs. (A1) and (A2),

$$\mathrm{tr}[\rho[a_i^\dagger a_j, a_k^\dagger a_l]] = \left(p^i_{\mu\beta} - p^j_{\mu\beta}\right)\delta_{jk}\delta_{il} \tag{A4}$$

and

$$\mathrm{tr}[\rho[a_i^\dagger a_j, a_k^\dagger(t) a_l(t)]] = e^{i(\varepsilon_i-\varepsilon_j)t/\hbar}\left(p^i_{\mu\beta} - p^j_{\mu\beta}\right)\delta_{jk}\delta_{il}. \tag{A5}$$

Therefore, first quantization (single-particle) observables $\mathcal{A}$ and $\mathcal{B}$, summed over all electrons $\mathcal{A} = \sum_n \mathcal{A}_n$ and $\mathcal{B} = \sum_n \mathcal{B}_n$, correspond in second quantization to $\hat{A} = a_i^\dagger a_j A^{ij}$ and $\hat{B} = a_i^\dagger a_j B^{ij}$ ($A^{ij} = \langle i|\mathcal{A}|j\rangle$ and $B^{ij} = \langle i|\mathcal{B}|j\rangle$). We find from Eq. (A4)

$$\mathrm{tr}[\rho[\hat{A}, \hat{B}]] = \mathrm{Tr}[p_{\mu\beta}(\mathcal{H})[\mathcal{A}, \mathcal{B}]],$$

and from these,

$$\mathrm{Im}\,\mathrm{tr}[\rho\hat{A}\hat{B}] = \mathrm{Im}\,\mathrm{Tr}[p_{\mu\beta}(\mathcal{H})\mathcal{A}\mathcal{B}]. \tag{A6}$$

Using Eq. (A3) we obtain the generalization of Eq. (A6),

$$\mathrm{Im}\,\mathrm{tr}[\rho\hat{A}\hat{B}(t)] = \mathrm{Im}\,\mathrm{Tr}[p_{\mu\beta}(\mathcal{H})\mathcal{A}\mathcal{B}(t)]. \tag{A7}$$

This latter equation, used with $\hat{A} \to \sum_n \mathcal{R}_{n\xi}$ and $\hat{B} \to \sum_n \mathcal{V}_{n\xi'}$, gives Eq. (26).

APPENDIX B: PROOF OF EQ. (31)

The Fourier-transform of Eq. (A5) gives

$$\int_{-\infty}^{\infty} e^{-i\omega t}\mathrm{tr}[\rho[a_i^\dagger a_j, e^{iHt} a_k^\dagger a_l e^{-iHt}]]dt = 2\pi\delta\left(\frac{\varepsilon_i-\varepsilon_j}{\hbar}+\omega\right)[p_{\mu\beta}(\varepsilon_j-\hbar\omega) - p_{\mu\beta}(\varepsilon_j)]\delta_{jk}\delta_{il},$$

where we used the spectral representation of Dirac delta functions, $2\pi\delta(\omega) = \int_{-\infty}^{\infty} e^{-i\omega t}dt$, and the identity $\delta(x-y)f(x) = \delta(x-y)f(y)$. Dividing the above expression by $i\omega$ and taking the limit $\omega \to 0$, we find

$$\lim_{\omega\to 0}\frac{1}{i\omega}\int_{-\infty}^{\infty} e^{-i\omega t}\mathrm{tr}[\rho[a_i^\dagger a_j, e^{iHt} a_k^\dagger a_l e^{-iHt}]]dt = 2\pi\hbar i\delta\left(\frac{\varepsilon_i-\varepsilon_j}{\hbar}\right)p'_{\mu\beta}(\varepsilon_j)\delta_{jk}\delta_{il}.$$

Using the spectral representation in the reverse direction, we find

$$\lim_{\omega\to 0}\frac{1}{i\omega}\int_{-\infty}^{\infty} e^{-i\omega t}\mathrm{tr}[\rho[a_i^\dagger a_j, e^{iHt} a_k^\dagger a_l e^{-iHt}]]dt = i\hbar\int_{-\infty}^{\infty} e^{-i(\varepsilon_i-\varepsilon_j)t}p'_{\mu\beta}(\varepsilon_j)dt\,\delta_{jk}\delta_{il}.$$

From these, it is now straightforward to show the two one-body observables

$$\lim_{\omega\to 0}\frac{1}{i\omega}\int_{-\infty}^{\infty} e^{-i\omega t}\mathrm{tr}[\rho[\hat{A}, \hat{B}(t)]]dt = i\hbar\int_{-\infty}^{\infty}\mathrm{Tr}[p'_{\mu\beta}(\mathcal{H})\mathcal{B}(t)\mathcal{A}]dt. \tag{B1}$$

For the case $A = B$, the left-hand side can be developed to give an integral over positive times,

$$\lim_{\omega\to 0}\frac{1}{i\omega}\int_{-\infty}^{\infty} e^{-i\omega t}\mathrm{tr}[\rho[\hat{A}, \hat{A}(t)]]dt = 4i\,\mathrm{Re}\left[\lim_{\omega\to 0}\frac{1}{i\omega}\int_0^{\infty} e^{-i\omega t}\mathrm{Im}\,\mathrm{tr}[\rho\hat{A}\hat{A}(t)]dt\right]. \tag{B2}$$

The right-hand side of Eq. (B1) can also be developed in a similar fashion:

$$i\hbar\int_{-\infty}^{\infty}\mathrm{Tr}[p'_{\mu\beta}(\mathcal{H})\mathcal{A}(t)\mathcal{A}]dt = 2i\hbar\,\mathrm{Re}\int_0^{\infty}\mathrm{Tr}[p'_{\mu\beta}(\mathcal{H})\mathcal{A}\mathcal{A}(t)]dt. \tag{B3}$$

Equating both right sides,

$$\mathrm{Re}\left[\lim_{\omega\to 0}\frac{1}{i\omega}\int_0^\infty e^{-i\omega t}\,\mathrm{Im\,tr}[\rho\hat{A}\hat{A}(t)]dt\right]=\frac{\hbar}{2}\mathrm{Re}\int_0^\infty \mathrm{Tr}[p'_{\mu\beta}(\mathcal{H})\mathcal{A}\mathcal{A}(t)]dt.$$

Finally, using Eq. (A7), we obtain

$$\mathrm{Re}\left[\lim_{\omega\to 0}\frac{1}{i\omega}\int_0^\infty e^{-i\omega t}dt\,\mathrm{Im\,tr}[p_{\mu\beta}(\mathcal{H})\mathcal{A}\mathcal{A}(t)]\right]=\frac{\hbar}{2}\int_0^\infty \mathrm{Re\,Tr}[p'_{\mu\beta}(\mathcal{H})\mathcal{A}\mathcal{A}(t)]dt, \tag{B4}$$

from which Eq. (31) can be directly deduced.

APPENDIX C: STABILIZING THE LOW-FREQUENCY CONDUCTIVITY SPECTRUM

One of the practical problems in calculating the conductivity at low frequencies arises in connection with introducing a finite resolution parameter ν in Eq. (29). The finite resolution distorts and usually underestimates the conductivity. This is seen in the red empty dots of Fig. 4, which shows reduced conductivity as $\omega\to 0$.

A second problem involves the fact that our conductivity calculations use a stochastic approach, which has fluctuation errors. For low frequency, these fluctuations grow considerably as $\omega\to 0$ (see the right panel of Fig. 6) due to the division by ω in Eq. (27).

The two problems described above combine: the high fluctuations in the low-frequency part of the ac conductivity are exacerbated when we take smaller ν, needed for converging the ac results to the dc limit.

Here, we introduce an approximation that helps converge the low-frequency ac conductivity, which relies on the fact that the dc conductivity ($\omega=0$), calculated by a different expression, Eq. (31), has finite and small fluctuations (seen in the right panel of Fig. 6). Our stabilization procedure mixes the low-frequency conductivity with that of an optimized model:

$$\sigma_k\leftarrow(1-w_k)\sigma_k+w_k\sigma_{\mathrm{model}}(\omega_k),$$

where σ_k is the conductivity corresponding to the frequency $\omega_k=k\nu$, $k=0,1,2,\ldots$. Here, w_k are mixing weights

$$w_k=\frac{1}{1+\left(\frac{\omega_k}{\omega_c}\right)^6},$$

emphasizing the low-energy spectrum. Since our system exhibits a metallic behavior, we choose ω_c as the highest frequency in the spectrum for which $\sigma_c>0.7\sigma_0$, and we use the Drude model $\sigma_{\mathrm{model}}(\omega)=\frac{\sigma_0}{1+\omega^2\tau_c^2}$, depending on the single parameter τ_c, i.e., the collision time. Given the calculated spectrum, we set this parameter as follows:

$$\tau_c^2=\frac{\sum_k w_k\omega_k^2\sigma_k(\sigma_0-\sigma_k)}{\sum_k w_k\omega_k^4\sigma_k^2}.$$

With this choice of parameter, the calculated conductivity values σ_k are as close as possible, in the root-mean-square sense, to those of the model conductivity $\sigma_{\mathrm{model}}(\omega_k)$ because we minimize the Lagrangian $L(\tau_c^2)=\sum_k w_k[(1+\omega_k^2\tau_c^2)\sigma_k-\sigma_0]^2$.

[1] T. Guillot, Interiors of giant planets inside and outside the solar system, Science **286**, 72 (1999).

[2] J. H. Nguyen and N. C. Holmes, Melting of iron at the physical conditions of the Earth's core, Nature (London) **427**, 339 (2004).

[3] R. Redmer, T. R. Mattsson, N. Nettelmann, and M. French, The phase diagram of water and the magnetic fields of Uranus and Neptune, Icarus **211**, 798 (2011).

[4] M. Pozzo, C. Davies, D. Gubbins, and D. Alfè, Thermal and electrical conductivity of iron at Earth's core conditions, Nature (London) **485**, 355 (2012).

[5] A. Benuzzi-Mounaix, S. Mazevet, A. Ravasio, T. Vinci, A. Denoeud, M. Koenig, N. Amadou, E. Brambrink, F. Festa, A. Levy, M. Harmand, S. Brygoo, G. Huser, V. Recoules, J. Bouchet, G. Morard, F. Guyot, T. De Resseguier, K. Myanishi, N. Ozaki, F. Dorchies, J. Gaudin, P. M. Leguay, O. Peyrusse, O. Henry, D. Raffestin, S. L. Pape, R. Smith, and R. Musella, Progress in warm dense matter study with applications to planetology, Phys. Scr. **T161**, 014060 (2014).

[6] M. French and N. Nettelmann, Viscosity and prandtl number of warm dense water as in ice giant planets, Astrophys. J. **881**, 81 (2019).

[7] D. Ehrenreich, C. Lovis, R. Allart, M. R. Z. Osorio, F. Pepe, S. Cristiani, R. Rebolo, N. C. Santos, F. Borsa, O. Demangeon, X. Dumusque, J. I. G. Hernández, N. Casasayas-Barris, D. Ségransan, S. Sousa, M. Abreu, V. Adibekyan, M. Affolter, C. A. Prieto, Y. Alibert, M. Aliverti, D. Alves, M. Amate, G. Avila, V. Baldini, T. Bandy, W. Benz, A. Bianco, E. Bolmont *et al.*, Nightside condensation of iron in an ultrahot giant exoplanet, Nature (London) **580**, 597 (2020).

[8] J. J. Fortney and N. Nettelmann, The interior structure, composition, and evolution of giant planets, Space Sci. Rev. **152**, 423 (2010).

[9] M. Bethkenhagen, E. R. Meyer, S. Hamel, N. Nettelmann, M. French, L. Scheibe, C. Ticknor, L. A. Collins, J. D. Kress, J. J. Fortney, and R. Redmer, Planetary ices and the linear mixing approximation, Astrophys. J. **848**, 67 (2017).

[10] M. French, A. Becker, W. Lorenzen, N. Nettelmann, M. Bethkenhagen, J. Wicht, and R. Redmer, *Ab initio* simulations for the material properties along jupiter's adiabat, Astrophys. J. Suppl. Series **202**, 5 (2012).

[11] D. Saumon, W. B. Hubbard, G. Chabrier, and H. M. van Horn, The role of the molecular-metallic transition of hydrogen in the evolution of jupiter, saturn, and brown dwarfs, Astrophys. J. **391**, 827 (1992).

[12] S. R. Kulkarni, Brown dwarfs: A possible missing link between stars and planets, Science **276**, 1350 (1997).

[13] A. Becker, W. Lorenzen, J. J. Fortney, N. Nettelmann, M. Schöittler, and R. Redmer, *Ab initio* equations of state for hydrogen (H-REOS.3) and helium (He-REOS.3) and their

implications for the interior of brown dwarfs, Astrophys. J. Suppl. Series **215**, 21 (2014).
[14] N. Booth, A. P. L. Robinson, P. Hakel, R. J. Clarke, R. J. Dance, D. Doria, L. A. Gizzi, G. Gregori, P. Koester, L. Labate, T. Levato, B. Li, M. Makita, R. C. Mancini, J. Pasley, P. P. Rajeev, D. Riley, E. Wagenaars, J. N. Waugh, and N. C. Woolsey, Laboratory measurements of resistivity in warm dense plasmas relevant to the microphysics of brown dwarfs, Nat. Commun. **6**, 8742 (2015).
[15] A. Becker, M. Bethkenhagen, C. Kellermann, J. Wicht, and R. Redmer, Material properties for the interiors of massive giant planets and brown dwarfs, Astrophys. J. **156**, 149 (2018).
[16] G. Chabrier, Quantum effects in dense coulombic matter: Application to the cooling of white dwarfs, Astrophys. J. **414**, 695 (1993).
[17] D. Saumon, S. Blouin, and P.-E. Tremblay, Current challenges in the physics of white dwarf stars, Phys. Rep. **988**, 1 (2022).
[18] D. E. Hinkel, Scientific and technological advancements in inertial fusion energy, Nucl. Fusion **53**, 104027 (2013).
[19] J. Lindl, Development of the indirect-drive approach to inertial confinement fusion and the target physics basis for ignition and gain, Phys. Plasmas **2**, 3933 (1995).
[20] E. M. Campbell, V. N. Goncharov, T. C. Sangster, S. P. Regan, P. B. Radha, R. Betti, J. F. Myatt, D. H. Froula, M. J. Rosenberg, I. V. Igumenshchev, W. Seka, A. A. Solodov, A. V. Maximov, J. A. Marozas, T. J. B. Collins, D. Turnbull, F. J. Marshall, A. Shvydky, J. P. Knauer, R. L. McCrory, A. B. Sefkow, M. Hohenberger, P. A. Michel, T. Chapman, L. Masse, C. Goyon, S. Ross, J. W. Bates, M. Karasik, J. Oh, J. Weaver, A. J. Schmitt, K. Obenschain, S. P. Obenschain, S. Reyes, and B. Van Wonterghem, Laser-direct-drive program: Promise, challenge, and path forward, Matter Radiat. Extremes **2**, 37 (2017).
[21] B. A. Remington, R. M. Cavallo, M. J. Edwards, D. D.-M. Ho, B. F. Lasinski, K. T. Lorenz, H. E. Lorenzana, J. M. McNaney, S. M. Pollaine, and R. F. Smith, Accessing high pressure states relevant to core conditions in the giant planets, Astrophys. Space Sci. **298**, 235 (2005).
[22] K. Falk, Experimental methods for warm dense matter research, High Pow. Laser Sci. Eng. **6**, e59 (2018).
[23] B. Militzer, D. M. Ceperley, J. D. Kress, J. D. Johnson, L. A. Collins, and S. Mazevet, Calculation of a deuterium double shock hugoniot from *ab initio* simulations, Phys. Rev. Lett. **87**, 275502 (2001).
[24] B. Holst, R. Redmer, and M. P. Desjarlais, Thermophysical properties of warm dense hydrogen using quantum molecular dynamics simulations, Phys. Rev. B **77**, 184201 (2008).
[25] M. A. Morales, C. Pierleoni, and D. M. Ceperley, Equation of state of metallic hydrogen from coupled electron-ion Monte Carlo simulations, Phys. Rev. E **81**, 021202 (2010).
[26] E. Brown, M. A. Morales, C. Pierleoni, and D. Ceperley, Quantum Monte Carlo techniques and applications for warm dense matter, in *Frontiers and Challenges in Warm Dense Matter*, edited by F. Graziani, M. P. Desjarlais, R. Redmer, and S. B. Trickey (Springer International, Cham, 2014), pp. 123–149.
[27] M. Bethkenhagen, B. B. L. Witte, M. Schörner, G. Röpke, T. Döppner, D. Kraus, S. H. Glenzer, P. A. Sterne, and R. Redmer, Carbon ionization at gigabar pressures: An *ab initio* perspective on astrophysical high-density plasmas, Phys. Rev. Res. **2**, 023260 (2020).
[28] M. Tuckerman, *Statistical Mechanics: Theory and Molecular Simulation* (Oxford University Press, Oxford, 2010).
[29] H. Niu, Y. Yang, S. Jensen, M. Holzmann, C. Pierleoni, and D. M. Ceperley, Stable solid molecular hydrogen above 900 K from a machine-learned potential trained with diffusion quantum Monte Carlo, Phys. Rev. Lett. **130**, 076102 (2023).
[30] C. J. Pickard and R. J. Needs, Structure of phase III of solid hydrogen, Nat. Phys. **3**, 473 (2007).
[31] K.-P. Bohnen, M. Kiwi, and H. Suhl, Friction coefficient of an adsorbed h atom on a metal surface, Phys. Rev. Lett. **34**, 1512 (1975).
[32] M. P. Grumbach, D. Hohl, R. M. Martin, and R. Car, Ab initio molecular dynamics with a finite-temperature density functional, J. Phys.: Condens. Matter **6**, 1999 (1994).
[33] B. Hellsing and M. Persson, Electronic damping of atomic and molecular vibrations at metal surfaces, Phys. Scr. **29**, 360 (1984).
[34] R. Baer and N. Siam, Real-time study of the adiabatic energy loss in an atomic collision with a metal cluster, J. Chem. Phys. **121**, 6341 (2004).
[35] F. Becca and S. Sorella, *Quantum Monte Carlo Approaches for Correlated Systems*, 1st ed. (Cambridge University Press, 2017).
[36] V. V. Karasiev, T. Sjostrom, D. Chakraborty, J. Dufty, K. Runge, F. E. Harris, and S. B. Trickey, Innovations in finite-temperature density functionals, in *Frontiers and Challenges in Warm Dense Matter*, *Vol. 96 of Lecture Notes in Computational Science and Engineering* (Springer Science & Business, 2014).
[37] P. Geerlings, F. De Proft, and W. Langenaeker, Conceptual density functional theory, Chem. Rev. **103**, 1793 (2003).
[38] R. M. Martin, *Electronic Structure: Basic Theory and Practical Methods* (Cambridge University Press, Cambridge, UK, 2004).
[39] J. Hutter, Car-Parrinello molecular dynamics, WIREs Comput. Mol. Sci. **2**, 604 (2012).
[40] A. Pribram-Jones, D. A. Gross, and K. Burke, DFT: A theory full of holes? Annu. Rev. Phys. Chem. **66**, 283 (2015).
[41] R. M. Martin, L. Reining, and D. M. Ceperley, *Interacting Electrons* (Cambridge University Press, 2016).
[42] F. Jensen, *Introduction to Computational Chemistry*, 3rd ed. (Wiley, Chichester, UK, 2017).
[43] O. A. von Lilienfeld, K.-R. Müller, and A. Tkatchenko, Exploring chemical compound space with quantum-based machine learning, Nat. Rev. Chem. **4**, 347 (2020).
[44] J. P. Perdew and M. Levy, Physical content of the exact kohn-sham orbital energies: Band gaps and derivative discontinuities, Phys. Rev. Lett. **51**, 1884 (1983).
[45] L. Kronik, T. Stein, S. Refaely-Abramson, and R. Baer, Excitation gaps of finite-sized systems from optimally tuned range-separated hybrid functionals, J. Chem. Theor.y Comput. **8**, 1515 (2012).
[46] N. D. Mermin, Thermal properties of the inhomogeneous electron gas, Phys. Rev. **137**, A1441 (1965).
[47] S. Pittalis, C. R. Proetto, A. Floris, A. Sanna, C. Bersier, K. Burke, and E. K. U. Gross, Exact conditions in finite-temperature density-functional theory, Phys. Rev. Lett. **107**, 163001 (2011).

[48] A. Pribram-Jones, S. Pilatis, E. K. U. Gross, and K. Burke, Thermal density functional theory in context, in *Frontiers and Challenges in Warm Dense Matter*, Vol. 96 of *Lecture Notes in Computational Science and Engineering* (Springer Science & Business, Cham, 2014).

[49] S. Groth, T. Dornheim, T. Sjostrom, F. D. Malone, W. M. C. Foulkes, and M. Bonitz, Ab initio exchange-correlation free energy of the uniform electron gas at warm dense matter conditions, Phys. Rev. Lett. **119**, 135001 (2017).

[50] M. Bonitz, T. Dornheim, Z. A. Moldabekov, S. Zhang, P. Hamann, H. Kählert, A. Filinov, K. Ramakrishna, and J. Vorberger, *Ab initio* simulation of warm dense matter, Phys. Plasmas **27**, 042710 (2020).

[51] Z. Moldabekov, T. Dornheim, J. Vorberger, and A. Cangi, Benchmarking exchange-correlation functionals in the spin-polarized inhomogeneous electron gas under warm dense conditions, Phys. Rev. B **105**, 035134 (2022).

[52] S. Zhang, H. Wang, W. Kang, P. Zhang, and X. T. He, Extended application of Kohn-Sham first-principles molecular dynamics method with plane wave approximation at high energy—From cold materials to hot dense plasmas, Phys. Plasmas **23**, 042707 (2016).

[53] A. Blanchet, J. Clérouin, M. Torrent, and F. Soubiran, Extended first-principles molecular dynamics model for high temperature simulations in the Abinit code: Application to warm dense aluminum, Comput. Phys. Commun. **271**, 108215 (2022).

[54] R. P. Feynman, N. Metropolis, and E. Teller, Equations of state of elements based on the generalized Fermi-Thomas theory, Phys. Rev. **75**, 1561 (1949).

[55] F. Perrot, Gradient correction to the statistical electronic free energy at nonzero temperatures: Application to equation-of-state calculations, Phys. Rev. A **20**, 586 (1979).

[56] V. V. Karasiev, T. Sjostrom, and S. B. Trickey, Generalized-gradient-approximation noninteracting free-energy functionals for orbital-free density functional calculations, Phys. Rev. B **86**, 115101 (2012).

[57] T. Sjostrom and J. Daligault, Fast and accurate quantum molecular dynamics of dense plasmas across temperature regimes, Phys. Rev. Lett. **113**, 155006 (2014).

[58] V. V. Karasiev, D. Chakraborty, O. A. Shukruto, and S. B. Trickey, Nonempirical generalized gradient approximation free-energy functional for orbital-free simulations, Phys. Rev. B **88**, 161108(R) (2013).

[59] K. Luo, V. V. Karasiev, and S. B. Trickey, Towards accurate orbital-free simulations: A generalized gradient approximation for the noninteracting free energy density functional, Phys. Rev. B **101**, 075116 (2020).

[60] V. L. Ligneres and E. A. Carter, An introduction to orbital-free density functional theory, in *Handbook of Materials Modeling*, edited by S. Yip (Springer, Dordrecht, Berlin, 2005), pp. 137–148.

[61] F. Lambert, J. Clérouin, and G. Zérah, Very-high-temperature molecular dynamics, Phys. Rev. E **73**, 016403 (2006).

[62] C. Ticknor, J. D. Kress, L. A. Collins, J. Clérouin, P. Arnault, and A. Decoster, Transport properties of an asymmetric mixture in the dense plasma regime, Phys. Rev. E **93**, 063208 (2016).

[63] S. X. Hu, R. Gao, Y. Ding, L. A. Collins, and J. D. Kress, First-principles equation-of-state table of silicon and its effects on high-energy-density plasma simulations, Phys. Rev. E **95**, 043210 (2017).

[64] A. J. White, O. Certik, Y. H. Ding, S. X. Hu, and L. A. Collins, Time-dependent orbital-free density functional theory for electronic stopping power: Comparison to the Mermin-Kohn-Sham theory at high temperatures, Phys. Rev. B **98**, 144302 (2018).

[65] A. J. White, C. Ticknor, E. R. Meyer, J. D. Kress, and L. A. Collins, Multicomponent mutual diffusion in the warm, dense matter regime, Phys. Rev. E **100**, 033213 (2019).

[66] W. Mi, K. Luo, S. B. Trickey, and M. Pavanello, Orbital-free density functional theory: An attractive electronic structure method for large-scale first-principles simulations, Chem. Rev. **123**, 12039 (2023).

[67] B. Cheng, G. Mazzola, C. J. Pickard, and M. Ceriotti, Evidence for supercritical behaviour of high-pressure liquid hydrogen, Nature (London) **585**, 217 (2020).

[68] O. A. von Lilienfeld and K. Burke, Retrospective on a decade of machine learning for chemical discovery, Nat. Commun. **11**, 4895 (2020).

[69] V. V. Karasiev, J. Hinz, S. X. Hu, and S. B. Trickey, On the liquid–liquid phase transition of dense hydrogen, Nature (London) **600**, E12 (2021).

[70] J. A. Ellis, L. Fiedler, G. A. Popoola, N. A. Modine, J. A. Stephens, A. P. Thompson, A. Cangi, and S. Rajamanickam, Accelerating finite-temperature Kohn-Sham density functional theory with deep neural networks, Phys. Rev. B **104**, 035120 (2021).

[71] B. Cheng, S. Hamel, and M. Bethkenhagen, Thermodynamics of diamond formation from hydrocarbon mixtures in planets, Nat. Commun. **14**, 1104 (2023).

[72] R. Baer, D. Neuhauser, and E. Rabani, Self-averaging stochastic kohn-sham density-functional theory, Phys. Rev. Lett. **111**, 106402 (2013).

[73] Y. Cytter, E. Rabani, D. Neuhauser, and R. Baer, Stochastic density functional theory at finite temperatures, Phys. Rev. B **97**, 115207 (2018).

[74] Y. Cytter, E. Rabani, D. Neuhauser, M. Preising, R. Redmer, and R. Baer, Transition to metallization in warm dense helium-hydrogen mixtures using stochastic density functional theory within the Kubo-Greenwood formalism, Phys. Rev. B **100**, 195101 (2019).

[75] A. J. White and L. A. Collins, Fast and universal kohn-sham density functional theory algorithm for warm dense matter to hot dense plasma, Phys. Rev. Lett. **125**, 055002 (2020).

[76] M. Chen, R. Baer, D. Neuhauser, and E. Rabani, Stochastic density functional theory: Real- and energy-space fragmentation for noise reduction, J. Chem. Phys. **154**, 204108 (2021).

[77] R. Baer, D. Neuhauser, and E. Rabani, Stochastic vector techniques in ground-state electronic structure, Annu. Rev. Phys. Chem. **73**, 255 (2022).

[78] T. Chen, Q. Liu, Y. Liu, L. Sun, and M. Chen, Combining stochastic density functional theory with deep potential molecular dynamics to study warm dense matter, Matter Radiat. Extremes **9**, 015604 (2024).

[79] P. Hohenberg and W. Kohn, Inhomogeneous electron gas, Phys. Rev. **136**, B864 (1964).

[80] W. Kohn and L. J. Sham, Self-consistent equations including exchange and correlation effects, Phys. Rev. **140**, A1133 (1965).

[81] N. Argaman and G. Makov, Thermodynamics as an alternative foundation for zero-temperature density-functional theory and spin-density-functional theory, Phys. Rev. B **66**, 052413 (2002).
[82] M. Weinert and J. W. Davenport, Fractional occupations and density-functional energies and forces, Phys. Rev. B **45**, 13709 (1992).
[83] V. V. Karasiev, T. Sjostrom, J. Dufty, and S. B. Trickey, Accurate homogeneous electron gas exchange-correlation free energy for local spin-density calculations, Phys. Rev. Lett. **112**, 076403 (2014).
[84] V. V. Karasiev, L. Calderín, and S. B. Trickey, Importance of finite-temperature exchange correlation for warm dense matter calculations, Phys. Rev. E **93**, 063207 (2016).
[85] V. V. Karasiev, J. W. Dufty, and S. B. Trickey, Nonempirical semilocal free-energy density functional for matter under extreme conditions, Phys. Rev. Lett. **120**, 076401 (2018).
[86] K. Ramakrishna, T. Dornheim, and J. Vorberger, Influence of finite temperature exchange-correlation effects in hydrogen, Phys. Rev. B **101**, 195129 (2020).
[87] J. Hinz, V. V. Karasiev, S. X. Hu, M. Zaghoo, D. Mejía-Rodríguez, S. B. Trickey, and L. Calderín, Fully consistent density functional theory determination of the insulator-metal transition boundary in warm dense hydrogen, Phys. Rev. Res. **2**, 032065(R) (2020).
[88] V. V. Karasiev, D. I. Mihaylov, and S. X. Hu, Meta-GGA exchange-correlation free energy density functional to increase the accuracy of warm dense matter simulations, Phys. Rev. B **105**, L081109 (2022).
[89] D. I. Mihaylov, V. V. Karasiev, and S. X. Hu, Thermal hybrid exchange-correlation density functional for improving the description of warm dense matter, Phys. Rev. B **101**, 245141 (2020).
[90] R. Kosloff, Time-dependent quantum-mechanical methods for molecular-dynamics, J. Phys. Chem. **92**, 2087 (1988).
[91] T. J. Rivlin, *Chebyshev Polynomials: From Approximation Theory to Algebra and Numbers Theory* (Wiley, New York, 1990).
[92] M. Chen, R. Baer, D. Neuhauser, and E. Rabani, Energy window stochastic density functional theory, J. Chem. Phys. **151**, 114116 (2019).
[93] Y. Luo, A. Zen, and S. Sorella, Ab initio molecular dynamics with noisy forces: Validating the quantum Monte Carlo approach with benchmark calculations of molecular vibrational properties, J. Chem. Phys. **141**, 194112 (2014).
[94] R. Kubo, Statistical-mechanical theory of irreversible processes. I. General theory and simple applications to magnetic and conduction problems, J. Phys. Soc. Jpn. **12**, 570 (1957).
[95] D. A. Greenwood, The Boltzmann equation in the theory of electrical conduction in metals, Proc. Phys. Soc. **71**, 585 (1958).
[96] B. Holst, M. French, and R. Redmer, Electronic transport coefficients from *ab initio* simulations and application to dense liquid hydrogen, Phys. Rev. B **83**, 235120 (2011).
[97] L. Calderín, V. V. Karasiev, and S. B. Trickey, Kubo-Greenwood electrical conductivity formulation and implementation for projector augmented wave datasets, Comput. Phys. Commun. **221**, 118 (2017).
[98] G. Kresse and J. Hafner, *Ab initio* molecular dynamics for liquid metals, Phys. Rev. B **47**, 558 (1993).
[99] G. Kresse and J. Hafner, *Ab initio* molecular-dynamics simulation of the liquid-metal–amorphous-semiconductor transition in germanium, Phys. Rev. B **49**, 14251 (1994).
[100] G. Kresse and J. Furthmüller, Efficient iterative schemes for *ab initio* total-energy calculations using a plane-wave basis set, Phys. Rev. B **54**, 11169 (1996).
[101] G. Kresse and J. Furthmüller, Efficiency of ab-initio total energy calculations for metals and semiconductors using a plane-wave basis set, Comput. Mater. Sci. **6**, 15 (1996).
[102] G. Kresse and D. Joubert, From ultrasoft pseudopotentials to the projector augmented-wave method, Phys. Rev. B **59**, 1758 (1999).
[103] N. Troullier and J. L. Martins, Efficient pseudopotentials for plane-wave calculations, Phys. Rev. B **43**, 1993 (1991).
[104] A. Baldereschi, Mean-value point in the brillouin zone, Phys. Rev. B **7**, 5212 (1973).
[105] N. W. Ashcroft and N. David Mermin, *Solid State Physics* (Harcort, Orlando, 1976).
[106] G. W. Robinson, C. H. Cho, and J. Urquidi, Isosbestic points in liquid water: Further strong evidence for the two-state mixture model, J. Chem. Phys. **111**, 698 (1999).
[107] M. Eckstein, M. Kollar, and D. Vollhardt, Isosbestic points in the spectral function of correlated electrons, J. Low Temp. Phys. **147**, 279 (2007).
[108] P. Renati, Z. Kovacs, A. De Ninno, and R. Tsenkova, Temperature dependence analysis of the NIR spectra of liquid water confirms the existence of two phases, one of which is in a coherent state, J. Mol. Liq. **292**, 111449 (2019).
[109] Y. Gao, D. Neuhauser, R. Baer, and E. Rabani, Sublinear scaling for time-dependent stochastic density functional theory, J. Chem. Phys. **142**, 034106 (2015).
[110] V. Vlček, R. Baer, and D. Neuhauser, Stochastic time-dependent DFT with optimally tuned range-separated hybrids: Application to excitonic effects in large phosphorene sheets, J. Chem. Phys. **150**, 184118 (2019).
[111] X. Zhang, G. Lu, R. Baer, E. Rabani, and D. Neuhauser, Linear-response time-dependent density functional theory with stochastic range-separated hybrids, J. Chem. Theor. Comput. **16**, 1064 (2020).
[112] D. Neuhauser, Y. Gao, C. Arntsen, C. Karshenas, E. Rabani, and R. Baer, Breaking the theoretical scaling limit for predicting quasiparticle energies: The stochastic *GW* approach, Phys. Rev. Lett. **113**, 076402 (2014).
[113] E. Rabani, R. Baer, and D. Neuhauser, Time-dependent stochastic Bethe-Salpeter approach, Phys. Rev. B **91**, 235302 (2015).
[114] D. Neuhauser, R. Baer, and D. Zgid, Stochastic self-consistent second-order Green's function method for correlation energies of large electronic systems, J. Chem. Theor. Comput. **13**, 5396 (2017).

A. Appendix

A.1 EOS: Mixtures

The equation of state for the fluid methane−hydrogen mixture for a hydrogen molecular mass fraction of $\mathcal{X}_{H_2} = 0.116$. As carbon has a propensity to form bonds with pretty much any other element, in our case we start each simulation with the same arrangement of the molecules to restrict the formation of polymers and introducing biases. Fig. A.1 shows the

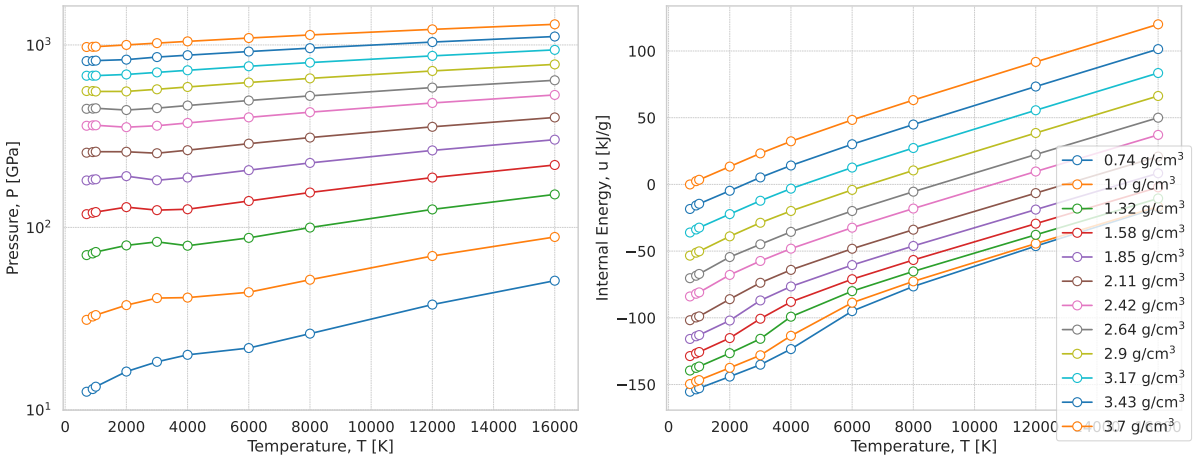


Figure A.1.: Thermal (left) and caloric (right) EOS of the CH_4-H_2 mixture for $\mathcal{X}_{H_2} = 0.116$ along the isochores.

EOS along various isochores. We find a small plateau at $T = 3000$ K for $\rho = 1.32$ g/cm^3 at about 83 GPa indicating the onset of dissociation. This behaviour indicates the onset of a phase transition from a molecular to polymeric fluid.

A.2 Convergence of DFT-MD and electronic properties simulations

DFT-MD simulations allows us to explore the behavior of the mixture of methane and hydrogen for various hydrogen molecule fraction, however rigorous convergence tests are an absolute necessity. The output of the simulations are used to form the EOS, however the pressure and the specific internal energy are of main interest. For pressures, a well-defined absolute quantity, we evaluate the relative deviation $\frac{\Delta P}{P} = (P_{\text{current}} - P)/P$ between the current pressure P_{current} and the pressure at the optimal settings. We consider a value better than 1% for our desired convergence. On the other hand, the absolute

values of specific internal energy have less significance. Hence, we analyze the absolute deviation $\Delta u = u_{\text{current}} - u$. A convergence target of better than a few kJ/g is aimed for the calculations.

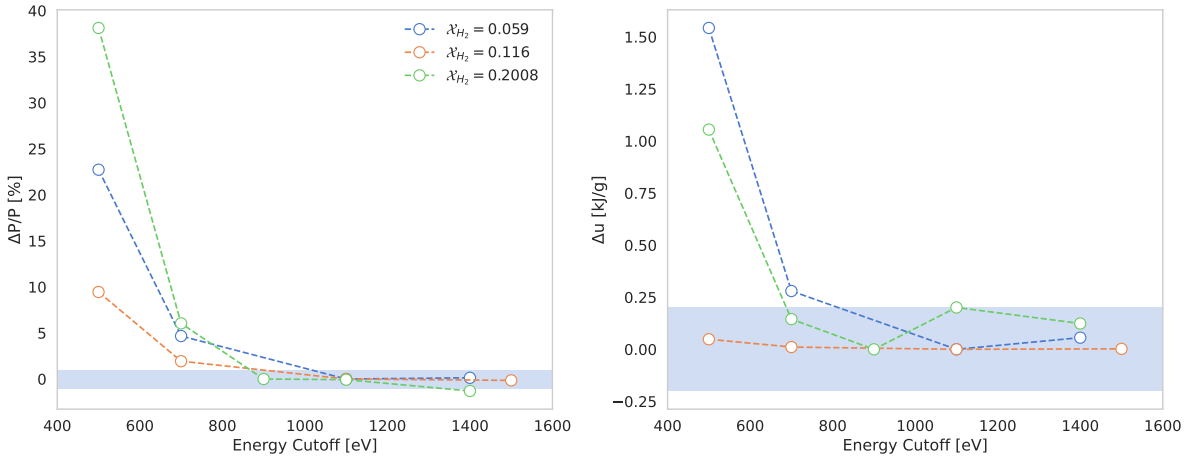


Figure A.2.: Convergence of pressure (left) and specific internal energy (right) concerning the plane wave cutoff is assessed at temperature of 3000 K and $\rho = 1.00$ g/cm^3. The shaded blue region signifies achieved convergence better than 1% and 0.2 kJ/g, respectively.

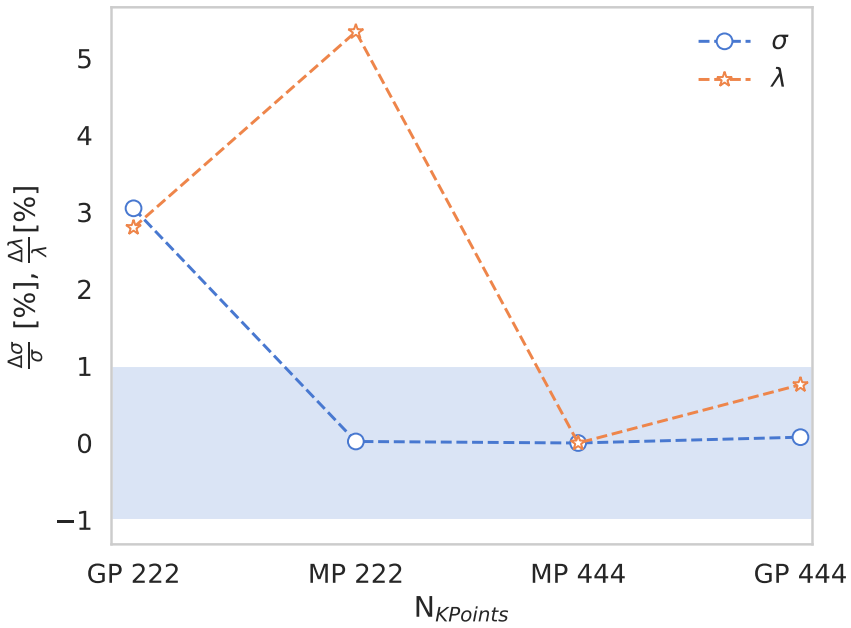


Figure A.3.: Convergence of electrical and thermal conductivity with respect to the $\mathbf{k}-$point sampling at 3000 K. The blue dots represent the deviation in electrical conductivity, the orange stars denotes the deviation in thermal conductivity. The blue shaded area indicates convergence better than 1 %.

For all the mixtures investigated here, we conducted a convergence test with respect to the plane wave cutoff energy. We present the results of the tests at 1.00 g/cm^3 and

3000 K in Fig. A.2 using BMVP [143] to sample the Brillouin zone. We computed the convergence of pressure and specific internal energy ranging from 500 eV to 1400 eV, and we find that a cutoff of 1100 eV is sufficient for accurate results.

The convergence patterns of the conductivity with respect to **k**-points The relative deviation of the static electronic properties i.e. electronic and thermal conductivities, at the current setting is compared to the best result using the relation $\frac{\Delta\phi}{\phi} = (\phi_{\text{current}} - \phi)/\phi$ where, ϕ denotes the electrical σ and thermal λ conductivity. In Fig. A.3, the result for 3000 K and density of 2.34 g/cm^3 is shown in blue and orange. The best value or the reference value is calculated with 318 particles and MP $4 \times 4 \times 4$. For electrical conductivity, the convergence can be achieved with MP $2\times$ 2 $\times$2, however the electronic thermal conductivity is more sensitive to **k**-point sampling and hence MP $4 \times 4 \times 4$ is chosen for the sampling.

Bibliography

[1] Ataru Sakuraba and Paul H Roberts, *Nature Geoscience* 2, 11 (2009).

[2] Joseph G O'Rourke and David J Stevenson, *Nature* 529, 7586 (2016).

[3] Maylis Landeau et al., *Nature Reviews Earth & Environment* 3, 4 (2022).

[4] Jonathan E Mound and Christopher J Davies, *Nature Geoscience* 16, 4 (2023).

[5] Hao Cao et al., *Geophysical Research Letters* 41, 12 (2014).

[6] Wieland Dietrich and Johannes Wicht, *Physics of the Earth and Planetary Interiors* 217 (2013).

[7] CA Jones, *Icarus* 241 (2014).

[8] S Stanley, *Geophysical Research Letters* 37, 5 (2010).

[9] Winfried Lorenzen, Bastian Holst, and Ronald Redmer, *Physical Review B* 82, 19 (2010).

[10] Winfried Lorenzen, Bastian Holst, and Ronald Redmer, *Physical Review B* 84, 23 (2011).

[11] Marcus D Knudson et al., *Science* 348, 6242 (2015).

[12] Saburo Howard, Simon Müller, and Ravit Helled, *Astronomy & Astrophysics* 689 (2024).

[13] Albert Pergjokaj, Ravit Helled, and Simon Müller. University of Zurich, 2023.

[14] Marvin Ross, *Nature* 292, 5822 (1981).

[15] Dominik Kraus et al., *Nature Astronomy* 1, 9 (2017).

[16] Naeem Ahmad Tahir et al., *Scientific Reports* 13, 1 (2023).

[17] Mungo Frost et al., *Nature Astronomy* 8, 2 (2024).

[18] Hirokazu Kadobayashi et al., *Scientific Reports* 11, 1 (2021).

[19] Bingqing Cheng, Sebastien Hamel, and Mandy Bethkenhagen, *Nature Communications* 14, 1 (2023).

[20] Michel Mayor and Didier Queloz, *Nature* 378, 6555 (1995).

[21] Carlos Jaschek and Mercedes Jaschek. *The Classification of Stars*. Cambridge University Press, 1990.

[22] Rebekah I Dawson and John Asher Johnson, *Annual Review of Astronomy and Astrophysics* 56, 1 (2018).

[23] B-O Demory et al., *Astronomy & Astrophysics* 475, 3 (2007).

[24] GÁ Bakos et al., *The Astrophysical Journal* 710, 2 (2010).

[25] David J Stevenson, *In: Annual review of earth and planetary sciences. Volume 10.(A82-35776 17-88) Palo Alto, CA, Annual Reviews, Inc., 1982, p. 257-295.* 10 (1982).

[26] T Guillot, D Gautier, and G Schubert. *Treatise on Geophysics*. 2015.

[27] OA Hurricane et al., *Nature* 506, 7488 (2014).

[28] Samuel E Wurzel and Scott C Hsu, *Physics of Plasmas* 29, 6 (2022).

[29] TR Boehly et al., *Optics communications* 133, 1-6 (1997).

[30] Thomas Tschentscher et al., *Applied Sciences* 7, 6 (2017).

[31] Paul Emma et al., *Nature Photonics* 4, 9 (2010).

[32] SH Glenzer et al., *Journal of Physics B: Atomic, Molecular and Optical Physics* 49, 9 (2016).

[33] Makina Yabashi, Hitoshi Tanaka, and Tetsuya Ishikawa, *Synchrotron Radiation* 22, 3 (2015).

[34] Xiaojing Lai et al., *Geophysical Research Letters* 52, 17 (2025).

[35] Yuqian Huang et al., *National Science Review* (2025).

[36] J Aleksi Soininen, AL Ankudinov, and JJ Rehr, *Physical Review B* 72, 4 (2005).

[37] Edwin E Salpeter and Hans Albrecht Bethe, *Physical Review* 84, 6 (1951).

[38] HY Sun et al., *Matter And Radiation At Extremes* 2, 6 (2017).

[39] Valentin V Karasiev, Travis Sjostrom, and Samuel B Trickey, *Computer Physics Communications* 185, 12 (2014).

[40] Phanish Suryanarayana, *Chemical Physics Letters* 584 (2013).

[41] Eberhard KU Gross and Neepa T Maitra. In: *Fundamentals of Time-Dependent Density Functional Theory*. Springer, 2012, pp. 53–99.

[42] Attila Szabo and Neil S Ostlund. *Modern Quantum Chemistry: Introduction to Advanced Electronic Structure Theory*. Courier Corporation, 1996.

[43] B Militzer and DM Ceperley, *Physical Review Letters* 85 (1890).

[44] Fei Lin et al., *Physical Review Letters* 103, 25 (2009).

[45] Carlo Pierleoni et al., *Proceedings of the National Academy of Sciences* 113, 18 (2016).

[46] Ronald Redmer, *Physics Reports* 282, 2-3 (1997).

[47] Tobias Dornheim et al., *Physics of Plasmas* 30, 3 (2023).

[48] M Bonitz et al., *Physics of Plasmas* 27, 4 (2020).

[49] Ryan Cooke, *arXiv preprint arXiv:2409.06015* (2024).

[50] Ralph A Alpher, Hans Bethe, and George Gamow, *Physical Review* 73, 7 (1948).

[51] Richard H Cyburt et al., *Reviews of Modern Physics* 88, 1 (2016).

[52] Sara Seager, Dimitar D Sasselov, and Douglas Scott, *The Astrophysical Journal* 523, 1 (1999).

[53] J Chluba and RM Thomas, *Monthly Notices of the Royal Astronomical Society* 412, 2 (2011).

[54] Wayne Hu, *arXiv preprint arXiv:0802.3688* (2008).

[55] A Kashlinsky and MJ Rees, *Monthly Notices of the Royal Astronomical Society* 205, 4 (1983).

[56] BJ Carr, JR Bond, and WD Arnett, *Astrophysical Journal* 277 (1984).

[57] Ralf S Klessen and Simon CO Glover, *Annual Review of Astronomy and Astrophysics* 61, 1 (2023).

[58] Maurizio Salaris and Santi Cassisi. *Evolution of stars and stellar populations*. John Wiley & Sons, 2005.

[59] E. E. Salpeter, *Phys. Rev.* 88 (1952).

[60] E. E Salpeter, *Astrophysical Journal, vol. 116, p. 649-650* 116 (1952).

[61] E. G. Adelberger et al., *Reviews of Modern Physics* 83 (2011).

[62] L Iess et al., *Science* 364, 6445 (2019).

[63] Durante Durante et al., *Geophysical Research Letters* 47, 4 (2020).

[64] Armin Bergermann, Lucas Kleindienst, and Ronald Redmer, *The Journal of Chemical Physics* 161, 23 (2024).

[65] Miguel A Morales et al., *Proceedings of the National Academy of Sciences* 106, 5 (2009).

[66] Winfried Lorenzen, Bastian Holst, and Ronald Redmer, *Physical Review Letters* 102, 11 (2009).

[67] Manuel Schöttler and Ronald Redmer, *Physical Review Letters* 120, 11 (2018).

[68] Burkhard Militzer et al., *The Planetary Science Journal* 3, 8 (2022).

[69] Saburo Howard et al., *arXiv preprint arXiv:2507.06288* (2025).

[70] Armin Bergermann, Martin French, and Ronald Redmer, *Physical Review B* 109, 17 (2024).

[71] H Abu-Shawareb et al., *Physical Review Letters* 129, 7 (2022).

[72] A. L. Kritcher et al., *Physical Review E* 109 (2024).

[73] H. Abu-Shawareb et al., *Physical Review Letters* 132 (2024).

[74] Paul Loubeyre, René Letoullec, and Jean-Pierre Pinceaux, *Physical Review Letters* 72, 9 (1994).

[75] Timothy A Strobel et al., *Physical Review Letters* 107, 25 (2011).

[76] Robin Turnbull et al., *Physical Review Letters* 121, 19 (2018).

[77] Dylan K Spaulding et al., *Nature Communications* 5, 1 (2014).

[78] P Hestermans and David White, *The Journal of Physical Chemistry* 65, 2 (1961).

[79] Feng Wang, *Journal of Molecular Structure: THEOCHEM* 678, 1-3 (2004).

[80] JOS Lelieveld, Paul J Crutzen, and Frank J Dentener, *Tellus B* 50, 2 (1998).

[81] Donald J Wuebbles and Katharine Hayhoe, *Earth-Science Reviews* 57, 3-4 (2002).

[82] J Houghton, *Physics* 68, 6 (2005).

[83] Lyobomir I Dimitrov, *Geo-Marine Letters* 23, 3 (2003).

[84] Thomas M McCollom, *Proceedings of the National Academy of Sciences* 113, 49 (2016).

[85] Giuseppe Etiope, *Procedia Earth and Planetary Science* 17 (2017).

[86] F. W. Taylor et al. In: *Jupiter. The Planet, Satellites and Magnetosphere*. Ed. by Fran Bagenal, Timothy E. Dowling, and William B. McKinnon. Vol. 1. 2004, pp. 59–78.

[87] R Hanel et al., *Science* 204, 4396 (1979).

[88] D Gautier et al., *Astrophysical Journal* 257 (1982).

[89] Michael H Wong et al., *Icarus* 171, 1 (2004).

[90] R. Hanel et al., *Science* 206, 4421 (1979).

[91] LN Fletcher et al., *Icarus* 199, 2 (2009).

[92] Kevin H Baines et al., *Icarus* 114, 2 (1995).

[93] Glenn S Orton et al., *Icarus* 70, 1 (1987).

[94] Bruno Bézard et al., *Journal of Geophysical Research: Space Physics* 96, S01 (1991).

[95] Patrick GJ Irwin et al., *Journal of Geophysical Research: Planets* 127, 6 (2022).

[96] M Allen et al. In: *Exploration of Halley's Comet*. Springer, 1987, pp. 502–512.

[97] S Drapatz, Harold P Larson, and D Scott Davis. In: *Exploration of Halley's Comet*. Springer, 1987, pp. 497–501.

[98] Michael J Mumma et al., *Science* 272, 5266 (1996).

[99] D. Bockelée-Morvan et al., *Astronomy and Astrophysics* 353 (2000).

[100] E.L. Gibb et al., *Icarus* 165, 2 (2003).

[101] Michael J Mumma and Steven B Charnley, *Annual Review of Astronomy and Astrophysics* 49, 1 (2011).

[102] Nikku Madhusudhan et al., *The Astrophysical Journal Letters* 983, 2 (2025).

[103] Nicholas F. Wogan et al., *The Astrophysical Journal Letters* 963, 1 (2024).

[104] Kevin B. Stevenson et al. *K2-18b Does Not Meet The Standards of Evidence For Life*. 2025. arXiv: 2508.05961 [astro-ph.EP].

[105] R. Luque et al. *Insufficient evidence for DMS and DMDS in the atmosphere of K2-18 b. From a joint analysis of JWST NIRISS, NIRSpec, and MIRI observations*. 2025. arXiv: 2505.13407 [astro-ph.EP].

[106] M. S. Somayazulu et al., *Science* 271, 5254 (1996).

[107] Lewis J. Conway and Andreas Hermann, *Geosciences* 9, 5 (2019).

[108] Umbertoluca Ranieri et al., *Physical Review Letters* 128, 21 (2022).

[109] Tristan Guillot, *Science* 286 (1999).

[110] Wendell C Demarcus, *Astronomical Journal* 63 (1958).

[111] PJE Peebles, *Astrophysical Journal* 140 (1964).

[112] François Soubiran and Burkhard Militzer, *The Astrophysical Journal* 806, 2 (2015).

[113] François Soubiran and Burkhard Militzer, *The Astrophysical Journal* 829, 1 (2016).

[114] J.-F. Danel and L. Kazandjian, *Physical Review E* 91 (2015).

[115] E. Schrödinger, *Physical Review Journals* 28 (1926).

[116] George Cain and Gunter H Meyer. *Separation of Variables for Partial Differential Equations: An Eigenfunction Approach*. Chapman and Hall/CRC, 2005.

[117] David J Griffiths and Darrell F Schroeter. *Introduction to Quantum Mechanics*. Cambridge University Press, 2018.

[118] Jun John Sakurai and Jim Napolitano. *Modern Quantum Mechanics*. Cambridge University Press, 2020.

[119] Claude Cohen-Tannoudji, Bernard Diu, and Franck Laloë. *Quantum Mechanics, Volume 3: Fermions, Bosons, Photons, Correlations, and Entanglement*. John Wiley & Sons, 2019.

[120] David Tong. *Quantum Mechanics: Lectures on Theoretical Physics*. Cambridge University Press, 2025.

[121] Max Born and W Heisenberg, *Original Scientific Papers Wissenschaftliche Originalarbeiten* (1985).

[122] N. Young. *An Introduction to Hilbert Space*. Cambridge University Press, 1988.

[123] R. Car and M. Parrinello, *Physical Review Letters* 55 (1985).

[124] Jorge Kohanoff. *Electronic Structure Calculations for Solids and Molecules: Theory and Computational Methods*. Cambridge University Press, 2006.

[125] John C Slater, *Physical Review* 81, 3 (1951).

[126] L. H. Thomas, *Mathematical Proceedings of the Cambridge Philosophical Society* 23, 5 (1927).

[127] Enrico Fermi, *Rendiconti Academia Dei Lincei* 6, 602-607 (1927).

[128] Paul AM Dirac. In: *Mathematical Proceedings of the Cambridge Philosophical Society*. Vol. 26. 3. Cambridge University Press. 1930, pp. 361–375.

[129] P. Hohenberg and W. Kohn, *Physical Review Journal* 136 (1964).

[130] W. Kohn and L. J. Sham, *Physical Review Journals* 140 (1965).

[131] R G Parr, *Annual Review of Physical Chemistry* 34, Volume 34 (1983).

[132] Ann E Mattsson et al., *Modelling and Simulation in Materials Science and Engineering* 13, 1 (2004).

[133] Axel D. Becke, *The Journal of Chemical Physics* 140, 18 (2014).

[134] Eugene S. Kryachko and Eduardo V. Ludeña, *Physics Reports* 544, 2 (2014).

[135] R. O. Jones, *Reviews of Modern Physics* 87 (2015).

[136] Daan Frenkel and Berend Smit. In: *Understanding Molecular Simulation (Second Edition)*. Ed. by Daan Frenkel and Berend Smit. Second Edition. San Diego: Academic Press, 2002, pp. 1–6. ISBN: 978-0-12-267351-1.

[137] Wolfram Koch and Max C Holthausen. *A Chemist's Guide to Density Functional Theory*. John Wiley & Sons, 2015.

[138] Richard M Martin. *Electronic Structure: Basic Theory and Practical Methods*. Cambridge University Press, 2020.

[139] Eberhard Engel. *Density Functional Theory*. Springer, 2011.

[140] N. David Mermin, *Physical Review* 137 (1965).

[141] Felix Bloch, *Zeitschrift für Physik* 52, 7 (1929).

[142] RA Evarestov and VP Smirnov, *Physica Status Solidi (b)* 119, 1 (1983).

[143] A. Baldereschi, *Physical Review B* 7 (1973).

[144] Hendrik J. Monkhorst and James D. Pack, *Physical Review B* 13 (1976).

[145] N. W. Ashcroft and N. D. Mermin. *Solid State Physics*. Holt-Saunders, 1976.

[146] P. E. Blöchl, *Physical Review B* 50 (1994).

[147] G. Kresse and D. Joubert, *Physical Review B* 59 (1999).

[148] David Vanderbilt, *Physical Review B* 41 (1990).

[149] O. Krogh Andersen, *Physical Review B* 12 (1975).

[150] Eli Kraisler, *Israel Journal of Chemistry* 60, 8-9 (2020).

[151] S. H. Vosko, L. Wilk, and M. Nusair, *Canadian Journal of Physics* 58, 8 (1980).

[152] John P. Perdew and Yue Wang, *Physical Review B* 45 (1992).

[153] David C. Langreth and John P. Perdew, *Physical Review B* 21 (1980).

[154] M. Shishkin and G. Kresse, *Physical Review B* 75 (2007).

[155] M. Shishkin, M. Marsman, and G. Kresse, *Physical Review Letters.* 99 (2007).

[156] John P. Perdew, Kieron Burke, and Matthias Ernzerhof, *Physical Review Letters.* 77 (1996).

[157] Viraht Sahni, K-P Bohnen, and Manoj K Harbola, *Physical Review A* 37, 6 (1988).

[158] Jochen Heyd, Gustavo E Scuseria, and Matthias Ernzerhof, *The Journal of Chemical Physics* 118, 18 (2003).

[159] Jochen Heyd and Gustavo E Scuseria, *The Journal of Chemical Physics* 120, 16 (2004).

[160] Jochen Heyd and Gustavo E Scuseria, *The Journal of Chemical Physics* 121, 3 (2004).

[161] H Hellmann, *Zeitschrift für Physik* 85, 3 (1933).

[162] R. P. Feynman, *Physical Review* 56 (1939).

[163] Shuichi Nosé, *The Journal of Chemical Physics* 81, 1 (1984).

[164] William G Hoover, *Physical Review A* 31, 3 (1985).

[165] Dennis C Rapaport. *The Art of Molecular Dynamics Simulation*. Cambridge University Press, 2004.

[166] Mark E Tuckerman. *Statistical Mechanics: Theory and Molecular simulation*. Oxford University Press, 2023.

[167] G. Kresse and J. Hafner, *Physical Review B* 47 (1993).

[168] G. Kresse and J. Hafner, *Physical Review B* 49 (1994).

[169] G. Kresse and J. Furthmüller, *Physical Review B* 54 (1996).

[170] G. Kresse and J. Furthmüller, *Computational Materials Science* 6, 1 (1996).

[171] Winfried Lorenzen. *Phase transitions in hydrogen-helium mixtures*. English. 2012.

[172] Pranawa C Deshmukh. *Foundations of Classical Mechanics*. Cambridge University Press, 2019.

[173] Michael P Allen and Dominic J Tildesley. *Computer Simulation of Liquids*. Oxford University Press, 2017.

[174] M D Segall et al., *Journal of Physics: Condensed Matter* 14, 11 (2002).

[175] José M Soler et al., *Journal of Physics: Condensed Matter* 14, 11 (2002).

[176] X. Gonze et al., *Computational Materials Science* 25, 3 (2002).

[177] Volker Blum et al., *Computer Physics Communications* 180, 11 (2009).

[178] Paolo Giannozzi et al., *Journal of Physics: Condensed Matter* 21, 39 (2009).

[179] Martin Preising. *Toward the nonmetal-to-metal phase transition of helium*. English. Rostock: Universität Rostock, 2021.

[180] Armin Bergermann, Ronald Redmer, and Roi Baer. *Molecules in the deep interior of giant planets*. English. Rostock: Universität Rostock, 2024.

[181] OH Nielsen and Richard M Martin, *Physical Review Letters* 50, 9 (1983).

[182] OH Nielsen and Richard M Martin, *Physical Review B* 32, 6 (1985).

[183] Mandy Bethkenhagen et al., *The Journal of Physical Chemistry A* 119, 42 (2015).

[184] Mandy Bethkenhagen, Martin French, and Ronald Redmer, *The Journal of Chemical Physics* 138, 23 (2013).

[185] John P. Perdew et al., *Proceedings of the National Academy of Sciences* 114, 11 (2017).

[186] John P. Perdew, *International Journal of Quantum Chemistry* 28, S19 (1985).

[187] John P. Perdew and Mel Levy, *Physical Review Letters* 51 (1983).

[188] Martin Preising and Ronald Redmer, *Physical Review B* 102, 22 (2020).

[189] Lars Stixrude and Raymond Jeanloz, *Proceedings of the National Academy of Sciences* 105, 32 (2008).

[190] Thomas M. Henderson, Joachim Paier, and Gustavo E. Scuseria, *Physica Status Solidi (b)* 248, 4 (2011).

[191] Yitao Si et al., *The Journal of Chemical Physics* 152, 2 (2020).

[192] Armin Bergermann, Lucas Kleindienst, and Ronald Redmer, *The Journal of Chemical Physics* 161, 23 (2024).

[193] Lars Hedin, *Physical Review Journals* 139 (1965).

[194] F Aryasetiawan and O Gunnarsson, *Reports on Progress in Physics* 61, 3 (1998).

[195] Wilfried G Aulbur, Martin Städele, and Andreas Görling, *Physical Review B* 62, 11 (2000).

[196] Vojtěch Vlček et al., *The Journal of Chemical Physics* 149, 17 (2018).

[197] C. Eckhardt, K. Hummer, and G. Kresse, *Physical Review B* 89 (2014).

[198] Tianyi Wang et al., *Energy & Environmental Science* 10, 2 (2017).

[199] Xihong Peng, Qun Wei, and Andrew Copple, *Physical Review B* 90, 8 (2014).

[200] Junbo Gong et al., *Advanced Science* 9, 29 (2022).

[201] D. B. McWhan and J. P. Remeika, *Physical Review B* 2 (1970).

[202] Ivan I. Naumov and Russell J. Hemley, *Phys. Rev. Lett.* 114 (2015).

[203] Isaac Silvera, *Proceedings of the National Academy of Sciences* 107, 29 (2010).

[204] Argha Jyoti Roy et al., *Physical Chemistry Chemical Physics* 26, 19 (2024).

[205] Georg KH Madsen and David J Singh, *Computer Physics Communications* 175, 1 (2006).

[206] Bastian Holst, Martin French, and Ronald Redmer, *Physical Review B* 83 (2011).

[207] P.B. Allen. In: *Conceptual Foundations of Materials*. Ed. by Steven G. Louie and Marvin L. Cohen. Vol. 2. Contemporary Concepts of Condensed Matter Science. Elsevier, 2006, pp. 165–218.

[208] R Franz and G Wiedemann, *Annalen der Physik* 165, 8 (1853).

[209] Mandy Bethkenhagen et al., *Physical Review E* 107, 1 (2023).

[210] Yael Cytter et al., *Physical Review B* 97 (2018).

[211] Roi Baer, Daniel Neuhauser, and Eran Rabani, *Physical Review Letters* 111 (2013).

[212] Roi Baer, Daniel Neuhauser, and Eran Rabani, *Annual Review of Physical Chemistry* 73 (2022).

[213] Michael F Hutchinson, *Communications in Statistics-Simulation and Computation* 18, 3 (1989).

[214] Rebecca Efrat Hadad et al., *Physical Review E* 109 (2024).

[215] Ronnie Kosloff, *The Journal of Physical Chemistry* 92, 8 (1988).

[216] Theodore Rivlin. *Chebyshev Polynomials: From Approximation Theory to Algebra and Number Theory*. Pure and Applied Mathematics, 1990.

[217] Ming Chen et al., *The Journal of Chemical Physics* 151, 11 (2019).

[218] Ye Luo, Andrea Zen, and Sandro Sorella, *The Journal of Chemical Physics* 141, 19 (2014).

[219] Daniel Neuhauser, Roi Baer, and Eran Rabani, *The Journal of Chemical Physics* 141, 4 (2014).

[220] Ben Shpiro et al., *Journal of Chemical Theory and Computation* 18, 3 (2022).

[221] Qianrui Liu and Mohan Chen, *Physical Review B* 106 (2022).

[222] Argha Jyoti Roy et al., *The Astrophysical Journal* 990, 2 (2025).

[223] Hiroshi Akima, *Journal of the ACM* 17, 4 (1970).

[224] M. Bethkenhagen et al., *The Astrophysical Journal* 848, 1 (2017).

[225] Leonardo Spanu et al., *Proceedings of the National Academy of Sciences* 108, 17 (2011).

[226] G. Tabak et al., *Physical Review B* 109 (2024).

[227] Benjamin L. Sherman et al., *Physical Review B* 86 (2012).

[228] D Ranjan et al., *Physics of Plasmas* 30, 5 (2023).

[229] Zhiyu He et al., *Science Advances* 8, 35 (2022).

[230] Otto Redlich and AT Kister, *Industrial & Engineering Chemistry* 40, 2 (1948).

[231] Ronghao Hu et al., *Physical Review B* 107 (2023).

[232] Martin French, Thomas R. Mattsson, and Ronald Redmer, *Physical Review B* 82 (2010).

[233] A. E. Barysevich and S. L. Cherkas, *Physics of Plasmas* 18, 5 (2011).

[234] Winfried Lorenzen, Bastian Holst, and Ronald Redmer, *Physical Review B* 84 (2011).

[235] Martin French et al., *The Astrophysical Journal Supplement Series* 202, 1 (2012).

[236] Alexander J. White et al., *Physics of Plasmas* 31, 4 (2024).

[237] C. E. Starrett et al., *Physics of Plasmas* 19, 10 (2012).

[238] C.E. Starrett et al., *High Energy Density Physics* 36 (2020).

[239] M. Yu. Kuchiev and W. R. Johnson, *Physical Review E* 78 (2008).

[240] W.R. Johnson, C. Guet, and G.F. Bertsch, *Journal of Quantitative Spectroscopy and Radiative Transfer* 99, 1 (2006).

[241] Nevill Mott. *Metal-insulator transitions*. CRC Press, 2004.

[242] AF Ioffe and AR Regel. In: *Progress in semiconductors*. 1960, pp. 237–291.

[243] N Nettelmann et al., *Planetary and Space Science* 77 (2013).

[244] Ravit Helled, Morris Podolak, and Eran Vos, *The Astrophysical Journal Letters* 805, 2 (2015).

[245] William J Borucki et al., *The Astrophysical Journal* 745, 2 (2012).

[246] Abderahmane Soubkiou et al., *Monthly Notices of the Royal Astronomical Society* 541, 4 (2025).

[247] Fergal Mullally et al., *The Astronomical Journal* 155, 5 (2018).

[248] Armin Bergermann et al., *Physical Review E* 103 (2021).

[249] Scott Habershon and David E. Manolopoulos, *The Journal of Chemical Physics* 135, 22 (2011).

[250] F. Ercolessi and J. B. Adams, *Europhysics Letters* 26, 8 (1994).

[251] Sergei Izvekov et al., *The Journal of Chemical Physics* 120, 23 (2004).

[252] Michael P. Desjarlais, *Physical Review E* 88 (2013).

B. Curriculum vitae

Education

- 09/2021 — present: **Ph.D.,** University of Rostock, Germany
  Supervisor: Prof. Dr. Ronald Redmer
- 06/2018 – 05/2020: **M.Sc. (Physics),** Indian Institute of Technology Hyderabad, India
  Thesis: *First Principle Study of* A_2MoS_4 *(A = K, Rb, Cs) and* Cs_2MoSe_4
  Supervisor: Prof. Venkatakrishanan Kanchana
- 2015 – 2018: **B.Sc. (Physics),** University of North Bengal, India
- 2004 – 2015: **High School,** Kendriya Vidyalaya Sevoke Road, India

Research Experience

- 09/2021– present: University of Rostock, Germany
  researcher assistant at AG Statistische Physik
- 02/2023 – 03/2023: Hebrew University of Jerusalem, Israel
  visiting researcher at Roi Baer's group
- 06/2019 – 12/2020: Indian Institute of Technology Hyderabad, India
  student researcher at Materials design and Simulation lab

Teaching

- Winter semester 2023 – 2024: Seminar on Physics of Dense Plasma
- Summer semester 2023 – 2024: Advanced lab course for masters student

List of Publication

1. Argha Jyoti Roy, Mandy Bethkenhagen, Armin Bergermann and Ronald Redmer
   Understanding the transport properties of methane-hydrogen mixtures under the interior conditions of ice giants.
   The Astrophysical Journal **990**, 2 (2025).

2. Rebecca Efrat Hadad, Argha Jyoti Roy, Eran Rabani, Ronald Redmer and Roi Baer
Stochastic density functional theory combined with Langevin dynamics for warm dense matter.
Physical Review E **109**, 065304 (2024).

3. Argha Jyoti Roy, Armin Bergermann, Mandy Bethkenhagen and Ronald Redmer
Mixture of hydrogen and methane under planetary interior conditions.
Physical Chemistry Chemical Physics, **26**, 14374 (2024).

4. Argha Jyoti Roy, Vineet Kumar Sharma and Venkatakrishanan Kanchana
High thermopower and optical properties of A_2MoS_4 (A=K, Rb, Cs) and Cs_2MoSe_4.
Physica Status Solidi B, 258: 2000587 (2021).

5. Anuroopa Behatha, Argha Jyoti Roy, C V Anusree, L Ponvijayakanthan, Vineet Kumar Sharma and Venkatakrishanan Kanchana
Correlation driven topological nodal ring ferromagnetic spin gapless semimetal: $CsMnF_4$.
Journal of Physics: Condensed Matter **33** 165803 (2021).

Conferences and Poster

1. 12^{th} **Joint Workshop on High Pressure, Planetary and Plasma Physics (HP4)**, Hamburg, Germany (2025)

2. 1^{st} **International Conference on Light-Matter-Interactions at Interfaces**, Rostock, Germany (2024)

3. 11^{th} **Joint Workshop on High Pressure, Planetary and Plasma Physics (HP4)**, Rostock, Germany (2023)

4. **Matter in extreme conditions**, Israel, Jerusalem (2023)

5. **Matter in Extreme Conditions from MATerial science to PLAnetary physics (MECMATPLA)**, Montgenèvre, France (2022)

6. **DFT Methods for Matter under Extreme Conditions**, Görlitz, Germany (2022)

7. **Strongly Coupled Coulomb Systems**, Görlitz, Germany (2022)

8. 10^{th} **Joint Workshop on High Pressure, Planetary and Plasma Physics (HP4)**, Brussels, Belgium (2022)

C. Acknowledgement

At the conclusion of my dissertation, I would like to express my gratitude. This achievement would not have been possible without the support of my supervisor, Prof. Dr. Ronald Redmer. His assistance, his lecture notes on WDM, and his open-door policy for professional and personal matters. I would also like to thank Roi Baer, who made it possible for me to visit his group and use the new development in the technique of DFT. I would also like to express my gratitude to Armin Bergermann for picking me up from the Hauptbahnhof, being my translator everywhere in Rostock, and having countless discussions and comments, helping me through my doctoral studies. Next, the tallest person that I have known to date, i.e., Martin Preising, thanks for the countless bike trips, bouldering, cooking escapades with Julian, "Yo Mama Jokes," and helping me to settle in Rostock. I would especially like to thank Anna Julia, Jan Maik, and Clemens, who accompanied me throughout my doctoral studies and on whom I could always rely for a little distraction. Max also deserves a nod for his playful punches, believing he's the next Floyd Mayweather—always a source of entertainment!. It has been a pleasure. I also thank Mandy and her database of methane; her expertise in the matter helped accelerate the work. A big thank you to the entire AG Statistical Physics Working Group and to Dominik Kraus' High Energy Density Physics Working Group for creating such a supportive work environment. Outside of academia, I want to acknowledge my friends Hari and Swaparjith for our lively discussions and debates. I also deeply appreciate Urvi and Mahrushi for standing by me, particularly during rough patches. Lastly, my most enormous gratitude goes to my family. My mother's constant support throughout my education has been my bedrock, and I am truly grateful for their unwavering belief in my choices.

D. Danksagung

Zum Abschluss meiner Dissertation möchte ich meine Dankbarkeit zum Ausdruck bringen. Dieses Ergebnis wäre jedoch ohne die Unterstützung meines Betreuers, Prof. Dr. Ronald Redmer, nicht möglich gewesen. Sein ständiger Zuspruch, seine Hilfe, seine Vorlesungsunterlagen zur warmen dichten Materie (WDM) sowie seine offene Tür für berufliche und persönliche Anliegen haben maßgeblich zu meinem Erfolg beigetragen. Mein besonderer Dank gilt Prof. Roi Baer, der mir den Aufenthalt in seiner Arbeitsgruppe ermöglicht und mir Zugang zu den neuesten Entwicklungen in der DFT-Methodik gewährt hat. Ebenso möchte ich Armin Bergermann danken – dafür, dass er mich vom Hauptbahnhof abgeholt hat, mir als Übersetzer in Rostock zur Seite stand, unzählige Diskussionen mit mir geführt und mich mit wertvollen Kommentaren durch die Promotionszeit begleitet hat. Dem größten Menschen, den ich bislang kennengelernt habe – Martin Preising – danke ich herzlich für die zahlreichen Radtouren, Boulder-Abende, Kochabenteuer mit Julian, die „Yo Mama"-Witze und die Hilfe beim Einleben in Rostock. Ein besonderer Dank gilt Anna Julia, Jan Maik und Clemens, die mich während meiner gesamten Promotionszeit begleitet haben und auf die ich mich stets verlassen konnte, wenn ich eine kleine Ablenkung brauchte. Auch Max verdient eine Erwähnung – für seine spielerischen Boxhiebe, seinen Glauben, der nächste Floyd Mayweather zu sein, und den ständigen Unterhaltungswert, den er damit geliefert hat. Es war mir eine Freude. Mein Dank gilt außerdem Mandy und ihrer Methan-Datenbank – ihre Fachkenntnisse auf diesem Gebiet haben die Arbeit erheblich beschleunigt. Ein großes Dankeschön geht an die gesamte Arbeitsgruppe Statistische Physik sowie an die Arbeitsgruppe Hochenergiedichtephysik von Dominik Kraus für die Schaffung eines unterstützenden und motivierenden Arbeitsumfelds. Außerhalb der Wissenschaft möchte ich meinen Freunden Hari und Swaparjith für unsere lebhaften Diskussionen und Debatten danken. Mein besonderer Dank gilt auch Urvi und Mahrushi, die in schwierigen Zeiten zu mir gehalten haben. Abschließend gilt mein tiefster Dank meiner Familie. Die unermüdliche Unterstützung meiner Mutter während meiner gesamten Ausbildung war mein größter Rückhalt, und ich bin ihr zutiefst dankbar für ihr unerschütterliches Vertrauen in meine Entscheidungen.

E. Declaration

The opportunity to undertake this doctoral project was not arranged for me commercially. In particular, I did not engage any organization that seeks supervisors for the preparation of dissertations in return for payment or that performs all or part of my obligations with regard to examination requirements on my behalf. I hereby declare on my honor that I have prepared this work independently and without outside assistance. I have used no resources or sources other than those specified by me. I hereby declare in lieu of oath that I have written this thesis independently and without outside help. I have not used any resources or sources other than those specified by me, and I have identified any passages taken verbatim or in substance from the works used as such.

Rostock, October 15, 2025
Argha Jyoti Roy